DEVELOPMENT OF A PHOTOELECTROCHEMICAL CELL USING III-V NITRIDES

ROBERT DUBREUIL

Presented to the faculty of Electrical and Computer Engineering in partial fulfillment for a PhD degree

Electrical Engineering
Lakehead University

ABSTRACT

Hydrogen production though Photoelectrochemical (PEC) water splitting is a source of clean and sustainable energy. Current energy production though the use of fossil fuels is rapidly depleting reserves and had been a direct cause of climate change. III-V nitrides offer a unique solution due to the variable band gap seen in Indium Gallium Nitride, which allows the semiconductor to capture the full spectrum of light by varying the quantities of Indium in the layer.

In this work, different type of III-V Nitrides were used as both photoanodes and photocathodes for the development of a III-V Nitride based PEC cell. In addition, NaCl was added to the electrolyte to act as simulated ocean water to reduce the cost of production for the cells, as current processes requires the use of distilled water for electrolyte preparation. Samples were grown in a custom built Metal Organic Chemical Vapor Deposition (MOCVD) reactor using a Flow Modulated Epitaxy (FME) method. Samples were first characterized using XRD, SEM, AFM and, UV-Vis before being used as photoelectrodes. A custom coded and commercial potentiostat were used in a three electrode set-up to determine the photoelectrochemical response of the samples. Samples were tested in a acidic, neutral and alkaline solutions to determine the best solution for III-V nitride based PEC cells. In addition to III-V nitride photoelectrodes, Zinc Oxide layers created though dip coating were also tested.

Finally, investigations into the band gap of Indium Nitride were performed. Films grown by Remote Plasma MOCVD on sapphire substrates while varying the indium pulse length and substrate temperature. The structural, morphological, electronic, and optical properties of the thin films are studied using X-ray diffraction and X-ray photoelectron spectroscopy and the effects of incorporating oxygen atoms in the structure is described. The N K-edge X-ray absorption spectroscopy (XAS) and X-ray emission spectroscopy (XES) measurements are used to determine the band gap and it is found to be 1.80 ± 0.25 eV. A complementary measurement, X-ray excited optical luminescence measurement is performed to confirm the band gap value obtained from XAS and XES measurements. O K-edge XAS measurements are performed to determine the presence of oxygen impurities in the samples.

PUBLICATIONS

[1] D. Alexandrov, J. Tot, R. Dubreuil, *et al.*, "Low temperature epitaxial deposition of GaN on LTCC substrates," in *2017 IEEE 5th Workshop on Wide Bandgap Power Devices and Applications (WiPDA)*, Oct. 2017, pp. 48–54. DOI: 10.1109/WiPDA.2017.8170501.

[2] R. Dubreuil, M. R. Amin, J. Tot, M. Nagorski, B. Kadikoff, A. Moewes, and D. Alexandrov, "Structure and bandgap determination of InN grown by RP-MOCVD," *Journal of Materials Science: Materials in Electronics*, vol. 33, no. 22, pp. 17 668–17 677, Aug. 2022, ISSN: 1573-482X. DOI: 10.1007/s10854-022-08630-x.

[3] B. Kadikoff, R. Dubreuil, J. Tot, and D. Alexandrov, "Investigation into the Characteristics of DC Nitrogen Plasma Used for Group III-N Semiconductor Thin-Film Growths," in *2018 41st International Spring Seminar on Electronics Technology (ISSE)*, May 2018, pp. 1–5. DOI: 10.1109/ISSE.2018.8443696.

[4] J. M. Mánuel, R. Dubreuil, J. Tot, *et al.*, "Engineering of III-Nitride Semiconductors on Low Temperature Co-fired Ceramics," *Scientific Reports*, vol. 8, no. 1, p. 6879, Dec. 2018, ISSN: 2045-2322. DOI: 10.1038/s41598-018-25416-6.

[5] J. Tot, R. Dubreuil, and D. Alexandrov, "Low temperature growth of InAlN on epitaxially grown SiC/Si (111) wafers," in *2017 40th International Spring Seminar on Electronics Technology (ISSE)*, May 2017, pp. 1–5. DOI: 10.1109/ISSE.2017.8000892.

ACKNOWLEDGEMENTS

I'd like to thank Dr Alexandrov for his unwavering support in allowing me to continue with my education and willingness to support all my ideas within the laboratory. I'd like to thank Michael Sorokopud and Dr. Guosheng Wu for the assistance with the instruments and patience with all my questions in the Instrumentation Lab. I'd like to thank Dr. Boriana Tzaneva for her invaluable help with the electrochemistry side of my thesis, I would not have been able to understand some of the concepts without her help. I'd also like to thank Dr. Valentin Videkov for his help with my initial experimentation. I'd also like to thank my research colleagues for providing me with support, ideas and memories throughout my research. To my parents, thank you for encouraging me to leave southern Ontario to pursue higher education. Finally I'd like to thank my partner Rachael for being there to keep me focused and on task whenever I got distracted throughout my studies.

CONTENTS

LIST OF FIGURES

LIST OF TABLES

LISTINGS

ACRONYMS

PEC Photoelectrochemical
STH Solar to Hydrogen Converison Efficiency
WE Working Electrode
CE Counter Electrode
RE Reference Electrode
HER Hydrogen Evolution Reaction
OER Oxygen Evolution Reaction
MBE Molecular Beam Epitaxy
MOCVD Metal Organic Chemical Vapor Deposition
HVPE Hydride Vapour Phase Epitaxy

ALD Atomic Layer Deposition
PVD Physical Vapour Deposition
CVD Chemical Vapour Deposition
RHE Reversible hydrogen electrode
SHE Standard hydrogen electrode
OCP Illuminated Open Circuit Potential
IPCE Incident photon-current conversion efficiency
SMU Source measuring unit
UHV Ultra High Vacuum
RHEED Reflection High Energy Electron Diffraction
MEE Migration Enhanced Epitaxy
FME Flow Modulated Epitaxy
VW Volmer-Weber
SK Stranski-Kranstanov
ALE Atomic Layer Epitaxy
XRD X-Ray Diffraction
WZ Wurtzite
FWHM Full Width at Half Maximum
UV-Vis Ultraviolet-visible
SEM Scanning Electron Microscope
EDX Energy Dispersive X-Ray
BSE Back Scatter Electron
AFM Atomic Force Microscope
DFT Density Functional Theory

1

INTRODUCTION

Fossil fuels have dominated the energy market since the industrial revolution. As such, they have been instrumental in humanities technological advancement. However, the burning of fossil fuels for energy comes with a severe negative impact. Increased pollution has led to many noticeable effects, the major of which is climate change. Global reserves of fossil fuels are also being depleted, with oil, natural gas, and coal having 50.7, 52.8and 114years left respectively. [1]

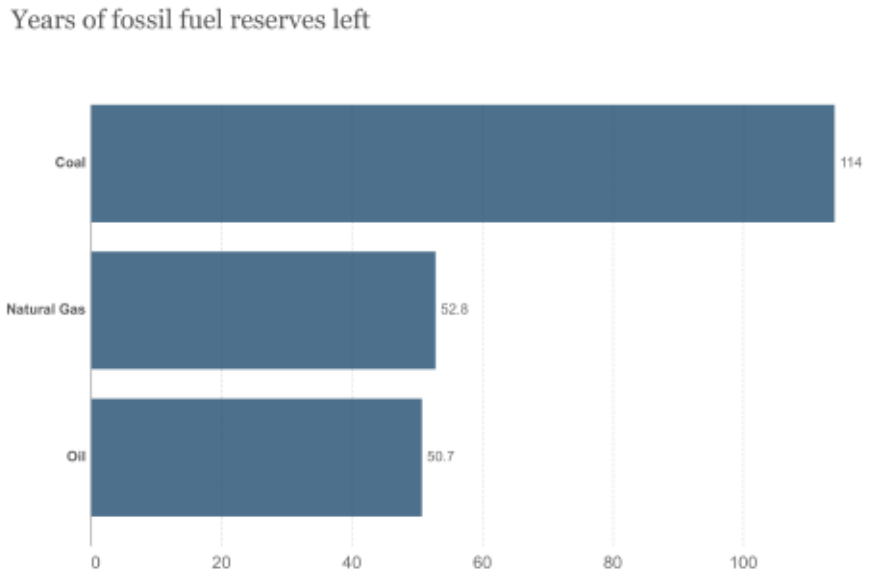

Figure 1.1: Years of global fossil fuels left, reported as reserve to product, which measures annual production to known reserves as a function of years remaining.[1]

Renewable energy sources provide an attractive alternative to the continuing burning of fossil fuels. Established sources such as nuclear, hydroelectric, solar, wind, geothermal, wave and tidal, and bioenergy

continue to provide an increased percentage of generation globally. (11.7%)[2]

1.1 HYDROGEN PRODUCTION AND STORAGE

Hydrogen is a natural next step for renewable energy sources. Hydrogen is almost unique as an energy storage system as it produces zero CO_2 and greenhouse gases. While hydrogen itself can be considered a green energy system, this is only true if the production of hydrogen is green itself (not generated using fossil fuels). Water electrolysis for hydrogen production has several advantages: purity, no pollution, a very simple process, and plenty of sources. Water electrolysis has been in commercial production for a century.[3] However, due to the energy demands, unless purity is the only desired outcome, hydrocarbon sources of hydrogen are still the primary source of hydrogen production. The use of 'grey' hydrogen is only justified in the short term. Moving to a truly green hydrogen is the only way to reduce the overall greenhouse gas amount in the atmosphere.

Hydrogen storage is key in a hydrogen based system, especially in large scale operations. These storage methods are divided depending on their applications (mobile or stationary). Storage can be split into two main methods physical based and material based seen in Fig. 1.2.

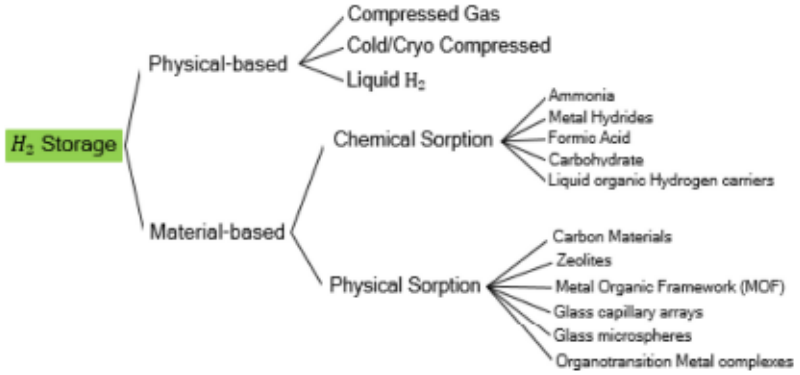

Figure 1.2: Methods of hydrogen storage.[4]

1.2 HISTORY OF III-V NITRIDES

The group III-V class of semiconductors have been used in many optoelectronic and high frequency device applications as an alternative to silicon. Often, this is because III-V semiconductors have a direct band gap, which means they can absorb and emit radiation at or above their band gap energy efficiently, or compared to silicon, have improved electron mobility and breakdown characteristics.

Table 1.1: Comparison of III-V electrical properties. [5]–[7]

MATERIAL	BAND GAP(eV)	TYPE	MOBILITY (cm^2/Vs)	CRITICAL FIELD (V/cm)
Silicon	1.12	indirect	1400	3×10^5
GaAs	1.42	direct	8500	5×10^5
GaP	2.26	indirect	250	1×10^5
GaSb	0.73	direct	3000	5×10^4
GaN	3.42	direct	1400	$3\text{-}5 \times 10^6$
InAs	0.35	direct	44000	4×10^4
InP	1.3	direct	5400	5×10^5
InSb	0.17	direct	77000	1000
InN	0.7-1.8	direct	4400	3×10^4

The III (aluminum, gallium, and indium) - V (nitrogen, phosphorus, arsenic, and antimony) group semiconductors consist of binary (GaAs, InAs, etc.), ternary ($Al_xGa_{1-x}As$, $In_xGa_{1-x}N$) and even quaternary ($In_xAl_yGa_{1-x-y}N$) solid solutions. Except for the nitrides, all have been studied for several decades due to the liquid phase growth such as the Czochralski process allowing for production of high quality bulk wafers.

The III-Nitrides are hindered because they cannot be grown in liquid phase. Nitrogen has a high vapour pressure and the high melting point of the nitrides themselves cause the nitrogen to dissociate out of the material before melting. With the inability to create wafers via liquid techniques, native substrates using, the comparatively slow and costly, vapour techniques caused wafers greater than 2 inches to be unavailable at the commercial scale. Heteroepitaxy, on sapphire, SiC

and recently Si, has seen commercial success since the development of the blue LED in the 90's. Heteroepitaxy leads to growth defects ($10^9 cm^{-1}$) extending from the interface due to the mismatch between the two materials. Techniques such as low temperature nucleation layers [8], selective area growth [9], and AlN buffer layers [10] have reduced defects in layers to $< 10^7 cm^{-1}$. [11]

There have been a variety of growth techniques for III-Nitrides, specifically for GaN as most devices are GaN based and use low content of AlGaN and InGaN for junction/quantum wells. Most of these techniques rely on ammonia (NH_3) as the nitrogen source. However thermal decomposition of ammonia starts at 600 °C for efficient production of atomic nitrogen and high V/III ratio for accommodate for nitrogen desorption.[6]

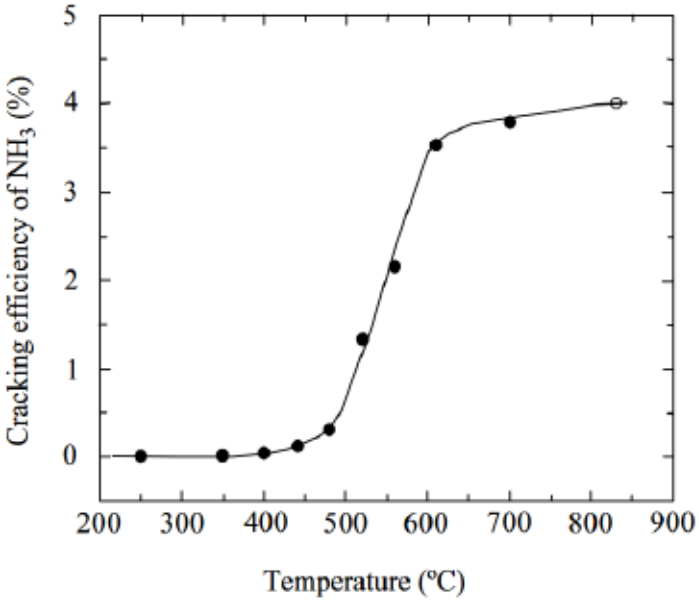

Figure 1.3: Thermal decomposition efficiency of ammonia versus substrate temperature.[6]

Ammonthermal growth of III-Nitrides begins at 900 °C with the best electrical and optical qualities requiring 1050 °C or higher using chemical vapour deposition (CVD) [12]. Without additional energy (plasma, laser excitation), thermal energy largely determines the layer

morphology by limiting the growth rate of different crystal planes and the migration of the precursors to the substrate surface as seen in Fig. 1.4.

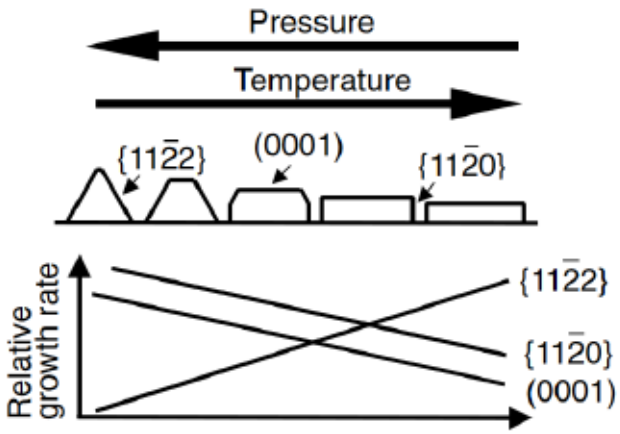

Figure 1.4: Morphological changes due to temperature and pressure.[9]

Alternative growth techniques have been proposed to lower the thermal budget. Plasma assisted techniques can lower III-Nitride deposition temperatures to between 400 °C and 500 °C. This allows for more substrates to be considered including transparent substrates such as glass [13]. However, due to the thermal and lattice mismatch with heteroepitaxy, defects and dislocations are not dealt with.

Recently, III-Nitrides have been used for photocells. The ternary alloy InGaN has a tunable band gap that spans almost the full range of the solar spectrum (0.5 to 3 eV). By varying the amount of indium in the alloy, multiple layers can be formed that capture different wavelengths of light. [14]

1.3 MOTIVATION

With the increased need for clean energy, and with hydrogen being a excellent alternative to fossil fuels, the generation of green hydrogen is proving to be a necessary and vital technology. The III-Nitrides

offer a unique ability to capture solar energy and generate hydrogen. Unlike metal-oxide based photoelectrodes, which corrodes in acidic or alkaline solutions, III-nitrides are very corrosion resistant in both acidic and alkaline solutions and photoelectrodes containing $In_xGa_{1-x}N$ materials have band-edge potentials which can satisfy water splitting conditions. [15]

Additionally, research into PEC cells uses distilled or deionized water as the basis for the electrolyte. This is a very energy intensive process to distill water for use in research. A cheaper alternative would be to use ocean water as it is abundant and would only need filtering to remove particulates.

In this work Plasma Enhanced MOCVD is used to create III-Nitride based photoelectrodes for use in PEC cells. The electrolytes used are simulated ocean water (3.5%) with a 1M NaOH solution added, H_2SO_4 and, NaCl for alkaline, acidic, and neutral solutions, respectively. The films are analyzed using x-ray diffraction (XRD), scanning electron microscopy (SEM), UV-Vis, and Raman spectroscopy. Electrical characteristics are analyzed using a Van Der Pauw Hall effect device and a source multimeter acting as a potentiostat, along with a commercial potentiostat for electrochemical measurements.

2

MATERIALS

2.1 III-V NITRIDES

Due to the heteroepitaxy nature of the III-nitrides, some fundamental challenges exist, primarily from their crystal structure. All group IV (Silicon and Germanium) and non-nitride group III-V (GaAs and InP) semiconductors have a cubic or zincblende structure. For the III-Nitrides the thermodynamically stable structure is hexagonal wurtzite.

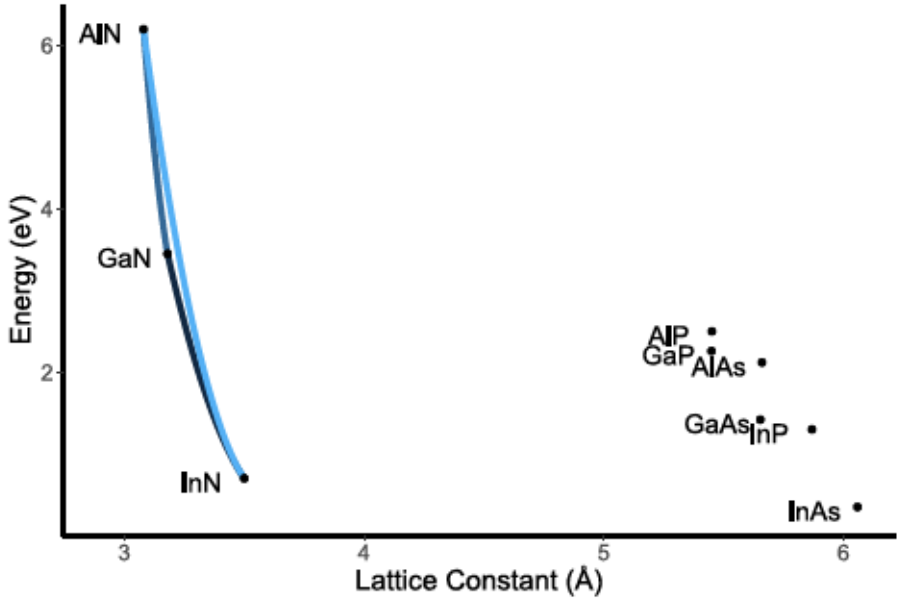

Figure 2.1: III-V semiconductors lattice constants compared to their band gaps.

Fig. 2.1 shows the relationship of the III-V semiconductor lattice constants to their respective band gaps. On the high end of the graph ($Å > 5$) are the cubic zincblende materials and left ($Å < 4$) are the III-Nitrides having the wurtzite structure. One point to note is that

the band gap of InN is still debated (between 0.7 eV and 1.8 eV) and investigations into the band gap of InN will be discussed in Section 5.1.

Both zincblende and wurtzite structures shares a tetrahedral nearest-neighbour atomic coordination due to the sp^3 hybrid bond. They differ in how the unit cell stacks,Fig. 2.2 shows the zincblende will have a stacking sequence of AaBbCcAaBbCc... while wurtzite has a AaBbAaBbAaBb... sequence, where A(a), B(b) and C(c) denote three kinds of cation (anion) position on the triangular lattice of the (001) and (111) planes.

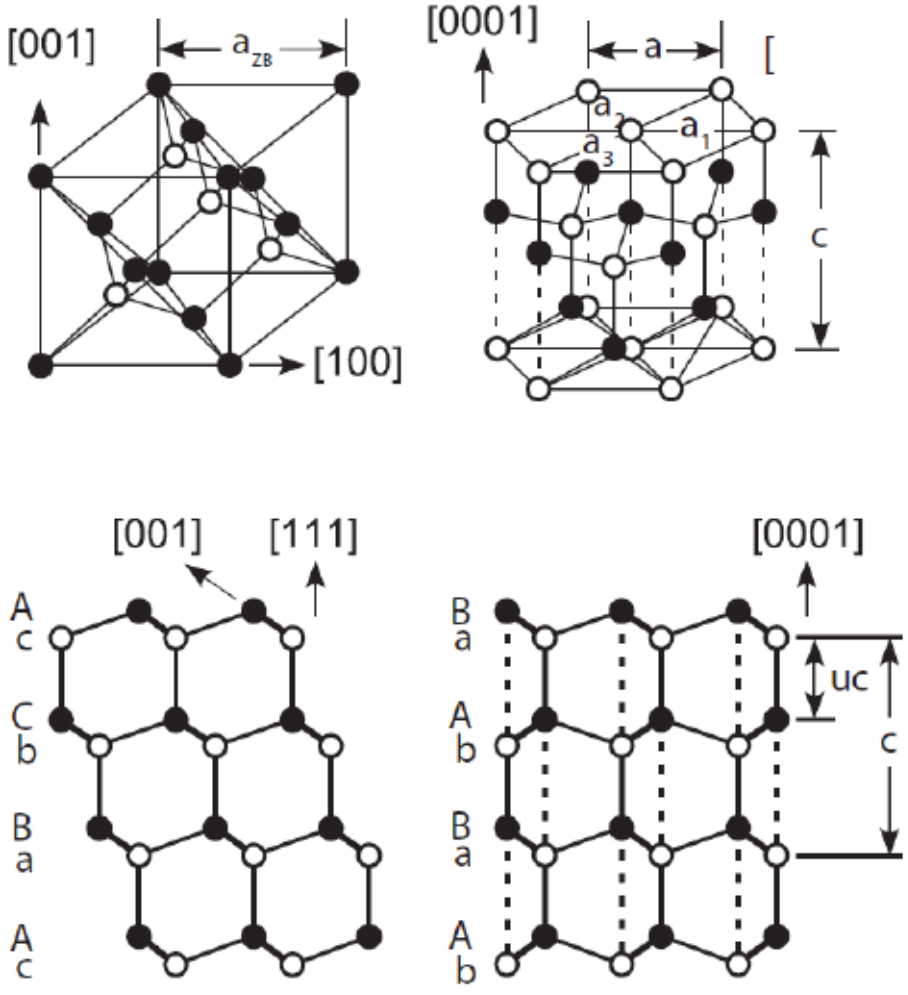

Figure 2.2: Atomic structure of zincblende (left) and wurtzite (right). [16]

In the wurtzite structure, however, there are pairs of cation-anion atoms connected by dashed line in the [0001] direction which are

attracted to each other by electrostatic force. This electrostatic interactions make the wurtzite III-Nitrides more stable than their zincblende counterparts because of the ionicity. The length of the dashed line tends to be shorter than the ideal one (with the ideal being $c/a = \sqrt{8/3} = 1.633$ and a internal parameter $u = 3/8 = 0.375$ where uc corresponds to the length of the bonds parallel to [0001] which can be seen in Table 2.1. These structural deformations induce spontaneous and piezoelectric (P_{sp} and P_z respectively) polarization.

Table 2.1: Lattice constants a, c(Å) and internal parameter u of the wurtzite III-N crystal, lattice constant a_{ZB}(Å)

	a	c	u	c/a	a_{ZB}
AlN	3.112 [17]	4.982 [17]	0.380 [18]	1.601	4.38 [17]
GaN	3.189 [17]	5.185 [17]	0.376 [18]	1.626	4.50 [17]
InN	3.545 [17]	5.703 [17]	0.377 [18]	1.609	4.98 [17]

Piezoelectric polarization induces a voltage on the c-axis as a restoring force in response to strain in the crystal in a direction (aligned either into or away from the (0001) surface), while P_{sp} comes from the charge difference between the group III atom and nitrogen atom in the crystal.

The band gap of InN has been debated for the past 20 years. With the band gap ranging from 0.7 to 2 eV. This is because InN has been very difficult to form. The difference in size, electronegativity and high vapour pressure of nitrogen over indium causes difficulty in formation. Early reports of InN growth (Through DC discharge, RF sputtering, and RF deposition) suggested a gap of $1.8 - 2.0$ eV at room temperature. The stoichiometry of InN is the source of the controversy. Reports that the actual band gap of InN is $0.7 - 0.8$ eV has been accepted. However, lower values such as 0.65 eV [19] and 0.67 eV [20] have also been reported. The larger band gap was explained by Oxygen contamination and Moss-Burstein Shift. While, those who

support the larger band gap explain the small gap as Mie resonance owing to the absorption or scattering of light from metallic In clusters. [21] This presence of In clusters would also make the mobility and doping level published suspect. Recently, an investigation into the band gap of InN was performed by the Lakehead Semiconductor Research Lab, in conjunction with the Canadian Light Source (CLS) at the University of Saskatchewan, which demonstrated a band gap of 1.8 eV though x-ray absorption/emission spectra to directly probe the band structure of InN with varying morphologies.[22] The results from [22] are expanded on in Section 5.1.

2.2 PHOTOELECTROCHEMISTRY

Presently, there are three ways light can be converted to useful energy (2.3). *Photosynthesis* is nature's method and is ultimately responsible for the chemical fuel that sustains life on earth. The basic process involves the conversion of carbon dioxide and water to sugar and molecular oxygen. The incident solar radiation provides the energy source, and some of this energy is stored as chemical fuel.

Although natural photosynthetic systems can form a variety of products (alcohol, sugars, methane, etc.), all operate similarly in that they convert incident photons into stored fuel. Typically, the photosynthetic system only converts $3 - 5\%$ of the total incident power as Gibbs free energy during an optimal growing season, yet this is sufficient to support life.

The second method, *Photovoltaic cells* (PV), are solid state devices that convert solar radiation into electrical energy. Initially constructed as early as 1954 [24] (with only efficiencies of $1 - 4\%$). A basic cell consists of two solids that are connected with an abrupt defined junction. [24] This type of junction provides the cell the ability to

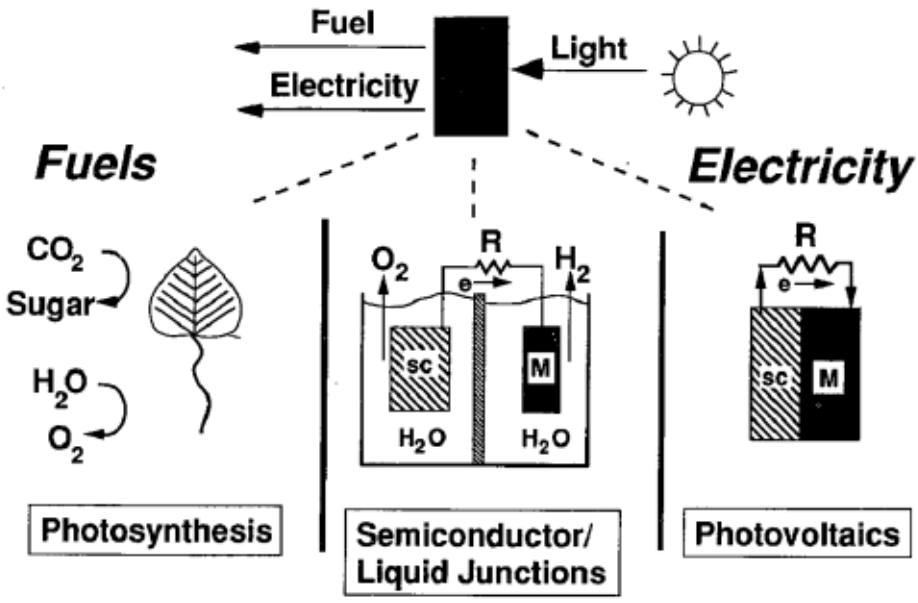

Figure 2.3: Solar energy conversion methods. [23]

direct current flow in one direction though the circuit to produce power. Unlike photosynthesis, photovoltaics do not convert photons into chemical fuels but directly into electric power. Modern PV cells are very efficient and are capable of converting up-to 47.1%. [25]

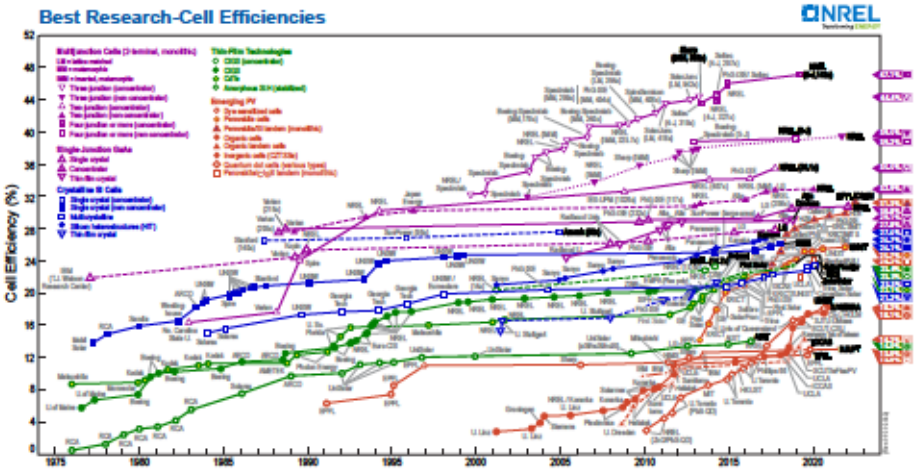

Figure 2.4: Highest confirmed conversion efficiencies plotted from 1976 to present. [26]

This final type of light-energy conversion is a photoelectrochemical cell which will be discussed further in Chapter 3

2.2.1 *Electrolytes*

Essential to the performance and overall stability of the device, the composition of the electrolyte must be considered. Water itself is a poor conductor, so it is necessary to dissolve charged ions to help in the charge transfer between the electrodes. Many considerations must be accounted for in choosing the electrolyte, including stability of both the solution and of the interaction of the electrodes with the solution, and the ionic conductivity. The electrolyte's role as a ionic liquid solution is to transfer the charge from the working electrode to the counter electrode. A positive charge is passed though protons (H^+), while the negative charge is passed though the hydroxide ions (OH^-). The standard ionic species, H^+ and OH^- have the highest limiting conductivity of 349.8 and 197 ($10^{-4}\Omega^{-1}mol^{-1}m^2$) respectively. Common cations such as K^+ and Na^+ have a conductivity of 73.5 and 50.1 ($10^{-4}\Omega^{-1}mol^{-1}m^2$) respectively, and common anions like Cl^- and SO_4^- have conductivities of 76.4 and 162 ($10^{-4}\Omega^{-1}mol^{-1}m^2$) respectively.Table 2.2 shows the conductivity, κ, resistance and potential loss of some common electrolytes.

Table 2.2: Common electrolyte compositions and pH with the associated conductivity, resistances, and, potential losses at $5mA/cm^2$. [27]

PH	COMPOSITION	$\kappa(\Omega^{-1}m^{-1})$	R_E (Ω)	V_{loss} (mV)	T (°C)
Neutral	Distilled Water	$10^{-3} \sim 10^{-4}$	$10^5 \sim 10^6$	∞	20
Neutral	Purified Water	$\sim 5.5 \times 10^{-6}$	$\sim 18 \times 10^{-6}$	∞	25
Acid	0.5 M K_2SO_4	6.2	16	81	20
	1.0 M H_2SO_4	36.6	2.7	14	20
	3.5 M H_2SO_4	73.9	1.4	7	18
Neutral	0.1 M NaCl	1.07	93	467	18
	0.5 M NaCl	3.8	26	132	18
	1.0 M NaCl	7.44	13	67	18
Base	0.1 M KOH	2.26	44	221	18
	0.5M KOH	10.7	9.3	47	18
	1.0 M KOH	20.1	5.0	25	20

2.2.2 *Electrodes*

A PEC device needs to be able to manage electronic, catalytic and optical functions at the same time. A true PEC device has the light-absorbing material fully immersed in the liquid. This increases the complexity of the cell. For example, incident light must travel though the liquid in order to illuminate the material, this results in a decrease in available photons received at the surface of the semiconductor. This in in turn decreases the potential Solar to Hydrogen Converison Efficiency (STH) on the PEC cell. [28]

2.2.2.1 *Counter Electrode*

Choosing the correct CE is based on the type of Working Electrode (WE). The size of the active surface of the CE is important, especially in a two-electrode configuration, and must be much larger than the WE. Over sizing the CE will ensure that the reaction at the WE is not limited by the reactions at on the CE. For all n-type semiconductors, H^+ is reduced

into H_2 via Hydrogen Evolution Reaction (HER) at the CE, for this Platinum foils or meshes make good CEs. For p-type semiconductors H_2O is oxidized onto H^+ and O_2 via Oxygen Evolution Reaction (OER) of the CE. Platinum is not suitable since it is a poor OER catalyst, instead oxides such as RuO_2 is a better electrode and can reduce over potential compared to the noble metals. The CEs are not interchangeable, as the catalyst may slowly deposit onto the WE. [28]

2.2.2.2 *Working Electrode*

For the WE, the semiconductor needs to be able to efficiently absorb light, have good charge transport and be able to generate sufficient power to drive the circuit. There are many deposition techniques for fabricating the WE including: Molecular Beam Epitaxy (MBE), MOCVD, electrodeposition, sol-gel, Atomic Layer Deposition (ALD), and a host of others. Each method has advantages and disadvantages such as precise control over layer thickness at the cost of low deposition rate for ALD, or monocrystalline layer at the cost of expensive fabrication for MBE and MOCVD.

Regardless of the fabrication, crystallinity plays an important role in the electronic properties such as the band gap, Fermi level position and mobility. The choice of fabrication technique determines the crystallinity (from amorphous to monocrystal). The thickness of the device is also important to maximize the charge carrier generation and collection. The thickness should be on the order of the optical penetration depth (α^{-1} where α is the absorption coefficient). Typically a thickness of 1 µm is sufficient for a direct band gap material ($\alpha \sim 10^6 \text{cm}^{-1}$), while for indirect ($\alpha \sim 10^4 \text{cm}^{-1}$) a thickness of a few hundred micrometers may be required.

2.2.2.3 *InGaN as Working Electrode*

The current photocatalytic technology is either too inefficient due to large band gaps [29]–[32] or unstable in aqueous solutions. [33], [34] The III-V nitrides offer a unique solution, $In_xGa_{(1-x)}N$ has a tunable direct band gap over the entire visible spectrum of light [35], and has generated a lot of interest for PEC cells as both photoanodes and photocathodes. [36]–[40] InGaN has the potential to straddle the redox potentials of water, allowing for splitting over the entire spectrum of light [41], [42] and has high corrosion resistance in an aqueous solution. [43]–[45] Fig. 2.5 shows some common working electrodes, including metal oxides, III-V, Si and III-Nitride semiconductors assuming an acidic environment. Both InGaN (up to $x = 0.5$ $In_xGa_{1-x}N$) and GaN encapsulate the redox potentials while InN only straddles the oxidation reaction.

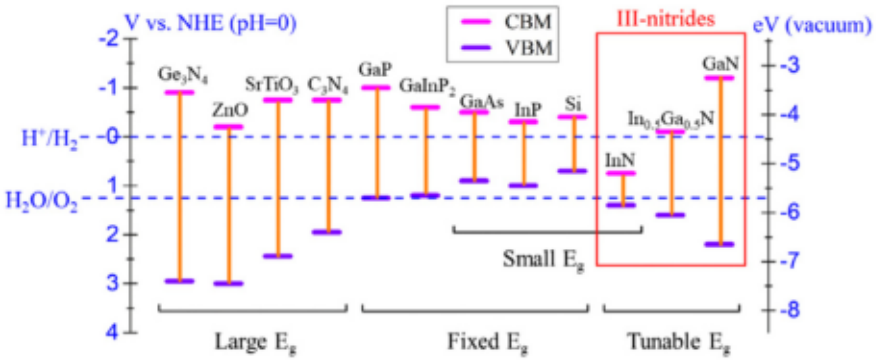

Figure 2.5: Energy band diagram of common working electrodes, assuming a pH=0 CBM and VBM represent conduction band minimums and valence band maximums respectively.[36]

2.2.2.4 *Reference Electrodes*

As the applied potential is a key parameter when studying the properties of a WE, the potential should be measured with respect to a known fixed reference potential, so that any changes in the applied potential reflects a change in the working electrode. The counter elec-

trode cannot be used as any over potential at the CE or any unknown interactions at the CE will interfere with measurements. To avoid this, a third electrode with a fixed known potential can be added. This is the RE. Table 2.3 shows an overview of the common references electrodes used in PEC research.

Table 2.3: Commonly used reference electrodes [46]

REFERENCE ELECTRODE	SOLUTION	POTENTIAL
Reversible Hydrogen	Actual Electrolyte solution purged with H_2 gas	0.059 x pH
Standard Hydrogen	$[H^+] = 1.18 \text{mol L}^{-1}$, $p(H_2) = 10 \times 10^5 \text{Pa}$	0
$Ag/AgCl$	0.1 M KCl	0.289
	1 M KCl	0.237
	3 M KCl	0.210
	3.5 M KCl	0.205
	3 M CaCl	0.209
Hg/Hg_2Cl_2	0.1 M KCl	0.334
	1 M KCl	0.281
	3.5 M KCl	0.250

Applied potentials are usually reported against the Reversible hydrogen electrode (RHE). Zero volts on the RHE scale is the H^+/H^2 redox potential of the solution, irrespective of pH. This differs from the Standard hydrogen electrode (SHE) which is only 0V at unity between the H^2 gas bubbled though and the production of H^+ in an ideal solution. $Ag/AgCl$ electrodes have replaced the traditional and environmentally damaging calomel electrodes (based on Hg/Hg_2Cl_2). The potential measures with a $Ag/AgCl$ can be converted to RHE using the below formula

$$\phi_{RHE} = \phi_{Ag/AgCl} + \phi^0_{Ag/AgCl\ vs\ SHE} + (0.059 \times pH) \tag{2.1}$$

Where $\phi^0_{Ag/AgclvsSHE}$ is the potential of the $Ag/AgCl$reference electrode with respect to the SHE, ϕ_{RHE} is the potential of the RHE and

$\phi_{Ag/AgCl}$ is the potential measured with respect to the $Ag/AgCl$ electrode.

3

PHOTOELELECTROCHEMICAL CELL

As mentioned in Chapter 2, there are three methods of converting light into energy: Photosynthesis, Photovoltaics and a photoelectrochemical cell. PEC cells can be considered as a hybrid between photosynthesis and photovoltaics, in that they can both produce electricity or produce chemical fuel. [23]

The principle of PEC water decomposition can be described in simple terms. Water is decomposed based on the conversion of light into electricity within a cell having two electrodes that are immersed in an aqueous electrolyte, with at least one electrode being a semiconductor. Theoretically there are three arrangement options for a PEC cell.

- A photo-anode made of an n-type semiconductor and a cathode made of metal.
- A photo-cathode made of a p-type semiconductor and an anode made of metal.
- A photo anode made of a n-type semiconductor and a photo-cathode made of a p-type semiconductor.

The following will focus on the first type of cell option, however the measurements and performance metrics apply to all three and there is no one option better than another.

3.1 METHOD OF OPERATION

When a semiconductor is brought into contact with another semiconductor or a metal contact [47], [48] the difference in Fermi levels cause a transfer of charges until equilibrium. For example, when a n-type semiconductor is brought into contact with a metal having a higher work function, electrons will move from the semiconductor into the metal. This removal of electrons leaves a positive space charge near the semiconductor surface of ionized donors. Assuming that the charge due to electrons can be neglected, the electric field and potential distribution can be obtained by integrating Poisson's equation in one dimension

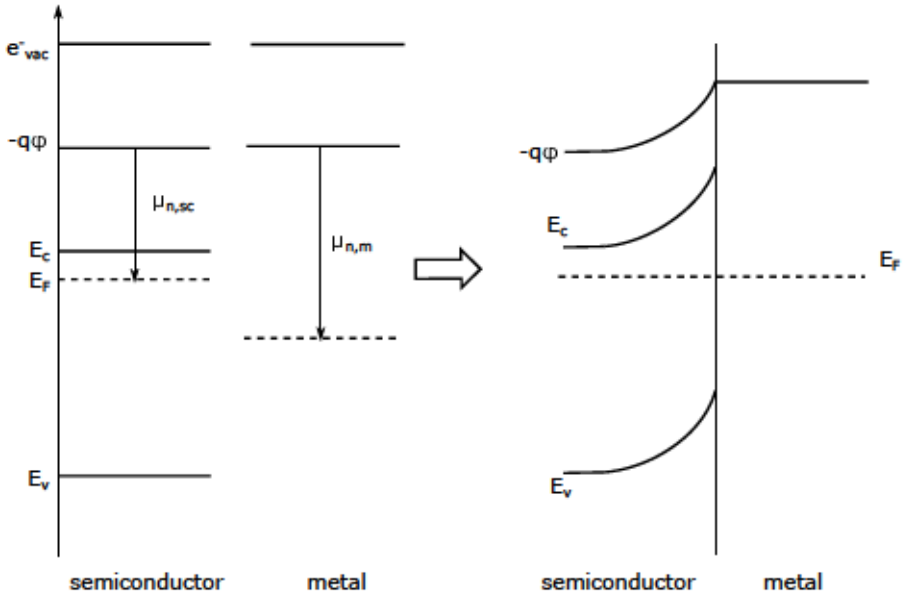

Figure 3.1: Formation of a Schottky barrier between a n-type semiconductor and a higher work function metal. [27]

$$\frac{\delta^2 \varphi}{\delta x^2} = \frac{\rho(x)}{\epsilon \epsilon_0} = -\frac{N_d}{\epsilon \epsilon_0} \tag{3.1}$$

With a boundary condition that the electric field and potential are zero at $x = W_{SC}$ (W_{SC} being the width of the space charge region), integration shows that the field varied linearly and the potential varies

with the square of the distance. This corresponds to the band bending seen in 3.1. This means that with no illumination there is no driving force to separate thermally generated electrons and holes.

The electrochemical potential of a charged species i is a partial molar quantity. It is the measure of the way the Gibbs energy G changes when i is added to a phase with a inner potential φ.

$$\bar{\mu}_i = \left(\frac{\delta \bar{G}}{\delta n_i}\right)_{T,p,n_j,\varphi} \tag{3.2}$$

This potential can be split into the associated chemical species and charge.

$$\bar{\mu}_i = \mu_i + z_i F \varphi \tag{3.3}$$

μ_i represents the chemical potential while $z_i F$ is the electrical work required to transfer one mole of charge. The absolute value of the chemical potential is the work function Φ. The chemical potential of electrons and holes is dependant on their concentration. The chemical potential per electron or hole would be

$$\mu_n = \mu_n^0 + k_B T \ln \frac{n}{N_C} \qquad \mu_p = \mu_p^0 + k_B T \ln \frac{p}{N_v} \tag{3.4}$$

Where μ_n^0 and μ_p^0 are the standard potential of elections and holes. while N_C and N_v are the standard states for electrons and holes.

When a semiconductor is immersed in an electrolyte containing a redox couple, electronic equilibrium is achieved by electron transfer across the semiconductor/electrolyte interface. A one-electron reaction would be

$$O + e^- \rightarrow R \tag{3.5}$$

where O is an oxidation (loss of electron/increase in the oxidation state) and R is a reduction (gain of an electron/decrease in the oxidation state). Which can be expressed in terms of electrochemical potential.

$$\mu_O + \mu_n = \mu_R \text{ or } \mu_n = \mu_R - \mu_O \tag{3.6}$$

From Eq. (3.6) at equilibrium the electrochemical potential is equal to the difference between the electrochemical potentials of R and O. By substituting Eq. (3.3) into Eq. (3.6) and expanding the chemical and electrical components.

$$\mu_n + \mu_n - q\varphi = \mu_O - \mu_R + q(z_R - Z_O)\varphi_{sol} \tag{3.7}$$

With $(z_R - z_O)$ being the number of electrons transferred. The contact potential difference between the semiconductor and solution is

$$\Delta\varphi = \varphi_{sc} - \varphi_{sol} = \frac{1}{q}(\mu_n + \mu_R - \mu_O) \tag{3.8}$$

Eq. (3.8) allows a comparison with a metal-semiconductor junction and by adapting Eq. (3.2), this allows for the definition of the redox Fermi energy.

$$E_{F,redox} = \mu_R - \mu_O = (\mu_R^0 - \mu_O^0) + k_B T \ln \frac{N_R}{N_O} \tag{3.9}$$

$E_{F,redox}$ plays the same role as any other Fermi level in a junction which allows for a band diagram similar to Fig. 3.1 as seen in Fig. 3.2.

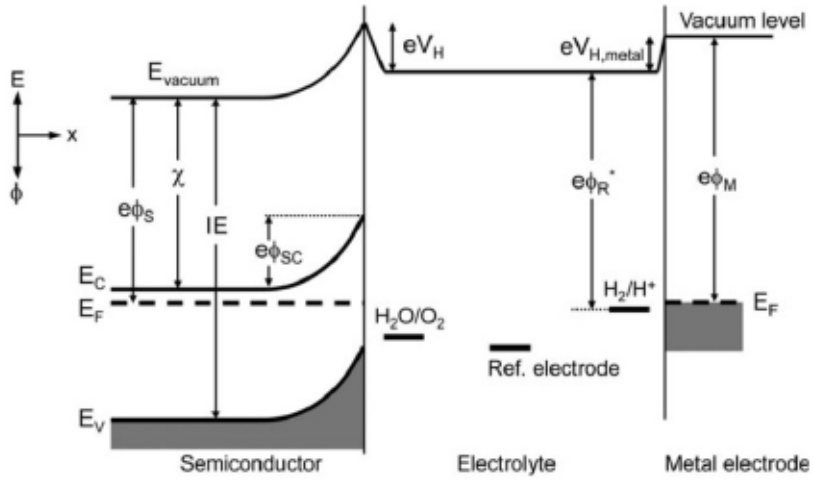

Figure 3.2: Energy band diagram for a PEC cell, using an n-type semiconductor. The electron affinity(κ) and ionization energy (IE) are constant while the work function ($e\phi_{SC}$) depends on the distance to the surface.[46]

3.1.1 *Reaction Mechanism Under Illumination*

When the immersed semiconductor is illuminated several processes occur:

- Light-induced ionization of the semiconductor, resulting in charge carrier formation.
- Oxidation of the water at the photo-anode.
- Transport of H^+ ions from the photo anode to the cathode.
- Reduction of hydrogen at the cathode.

The light induced ionization leads to the formation of electrons and holes in the conduction band and valence band, respectively.

$$2h\upsilon \rightarrow 2e' + 2h^{\bullet} \tag{3.10}$$

where h is Planck's constant, v the frequency, e' the electron, and $h^{\bullet}$ the hole. This reaction takes place when $hv \geq E_{g,sc}$ These induced electron-holes result in splitting water into gaseous oxygen and hydrogen

$$2h^{\bullet} + H_2O_{liquid} \rightarrow \frac{1}{2}O_2 + 2H^+ \tag{3.11}$$

This reaction takes place at the semiconductor/electrolyte interface. Oxygen is generated at the anode while the hydrogen ions migrate to the cathode though the electrolyte. At the same time though the electrical connection between the anode and cathode (external to the electrolyte) electrons generated from Eq. (3.10) are transferred to the cathode which cause a reductions of the hydrogen ions to gaseous hydrogen.

$$2H^+ + 2e' \rightarrow H_2 \tag{3.12}$$

Therefore, the overall reaction can expressed as

$$2hv + H_2O \rightarrow \frac{1}{2}O_2 + H_2 \tag{3.13}$$

Eq. (3.13) takes place when E_{photon} absorbed are equal to or greater than the threshold energy E_t:

$$E_i = \frac{\Delta G^0_{H_2O}}{2N_A} \tag{3.14}$$

Were $\Delta G^0_{H_2O}$ is the standard free enthalpy per mole of Eq. (3.13) $= 237.14\,\mathrm{kJ\,mol^{-1}}$, N_A is Avogadro's number $= 6.022 \times 10^{23}\,\mathrm{mol^{-1}}$. Eq. (3.14) yields:

$$E_i = hv = 1.23\,\mathrm{eV} \tag{3.15}$$

This means, that electrochemical decomposition of water is only possible when the electromotive force of the cell is equal to or larger that

1.23 eV. For practical purposes, an overpotential is generally considered for the WE to account for losses, as such $E_i = 1.6 - 2.0\,\text{eV}$.

3.2 CELL DESIGN

A general cell design consists of either a two-electrode or three-electrode cell with one or two compartments leading to one of four different configurations:

1. Two electrodes in one compartment
2. Three electrodes in one compartment
3. Two electrodes in two compartments
4. Three electrodes two compartments

Single compartment vessels can range from simple open vessels to complex circular vessels. The open vessel is the most basic, being a square quartz chamber with a flat surface to shine the light though. Quartz is used as it allows most of the light though including UV light, although a simple borosilicate glass beaker could be used. A second consideration is the use of ports for the electrodes. Ports allow for precise location of the electrodes. A final consideration would be the use of an optical window. Transparent quartz vessels can be expensive to produce and are therefore made in small sizes and thicknesses, which leads to fragility, an alternative would be to make the vessel out of borosilicate glass or Teflon. This allows for more complex shapes without the costly manufacturing time needed. A small quartz window is added to allow light into the chamber which is held in place by a o-ring or gasket to form a tight seal. Fig. 3.3 shows a variety of different configurations for a single compartment PEC cell.

Two compartment vessels are used for separating the WE and the CE so that any gas generated can be captured. In small scale testing, it

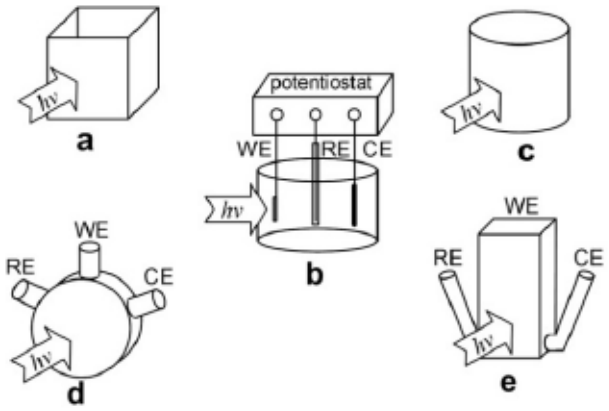

Figure 3.3: Different types of single compartment vessels. a)square transparent vessel, b) Schematic of a PEC set-up, c)simple open beaker, d) single compartment circular vessel, e)single compartment rectangular vessel. [49]

is not a requirement to separate the gases as the concern for potential explosion is small. With large scale production however, it is necessary to separate the gases. Traditionally, for a electrochemical reaction study with different electrolytes, a salt bridge was used. For a PEC cell, a two compartment cell can be made form two separate vessels held together with a ion membrane acting as the bridge. The ion membrane allows for H^+ to move though but no evolved gases. The membrane also allows for different electrolytes to be used. If one electrolyte is acidic and the other alkaline, a chemical bias can be established. [50]–[52] An alternative to using a salt bridge or membrane, is to use a *H-type* vessel. A H-type allows for gas separation with the membrane as two or more glass tubes are connected a small horizontal tubes close to the base of the tubes. This allows for ion flow and since the electrodes are placed higher than the horizontal tubes, any gas produced will bubble upwards which naturally separates the gases.[53], [54]

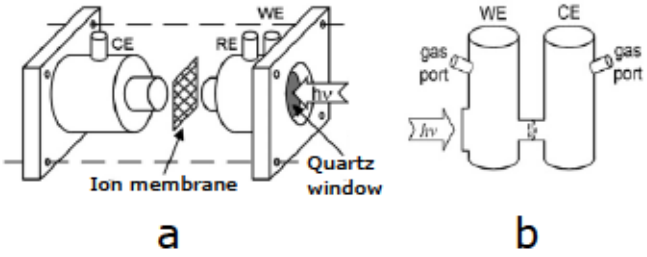

Figure 3.4: Two compartment cells a) Separate chambers[55], b) H-Type [53]

3.3 ELECTRODE PREPARATION

Proper preparation of the semiconductor electrode is essential to ensure only the material of interest is measured. Proper sealing, for example, is critical to keep the electrolyte from contact anything other than the semiconductor. Much of the requirements for the semiconductor layer have already been covered in Section 2.2.2.2, however construction of the electrode was not. In order to have optimal charge transfer an ohmic contact layer has to be used. An ohmic contact follows Ohm's law in that the current is a linear function of the potential. For n-type semiconductors a smaller work function is required, while for a p-type, a larger work function is required. Typical contacts are Aluminum ($\phi_m = 4.28\,\text{eV}$)[56] and Indium-Tin Oxide ($\phi_m = 4.4\,\text{eV}$) [57] for n-type and Gold $\phi_m = 5.3\,\text{eV}$) [58] for p-type.

To connect to the electrode, a number of methods can be used depending on the cell type. To connect using wires, depending of the size of the cell, it may be necessary to use two wires.The wires are stripped and connected to the cell using indium solder as indium has a high conductivity and adhesion. Silver paint could also be used. The indium and any uninsulated portions of the wires then must be protected using epoxy of sufficient thickness to avoid any pinholes.

A second method, which is used for samples in a library array, or if the semiconductor layer is very brittle and would crack with the epoxy curing, is to use copper tape and an o-ring. Copper tape is added to

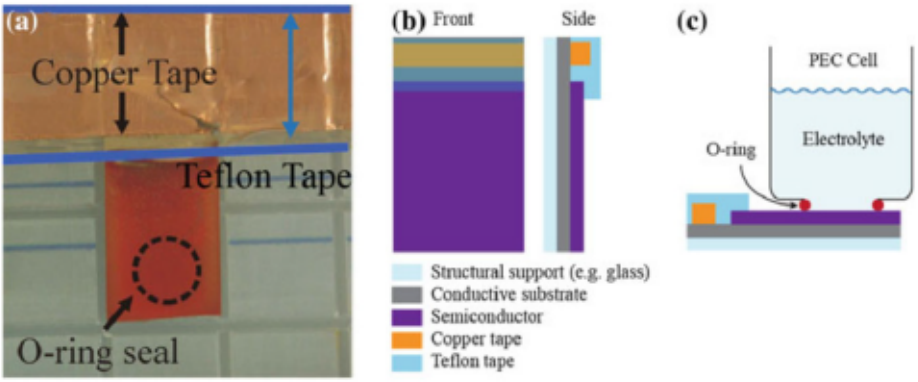

Figure 3.5: Copper tape electrode a) final assembly, the o-ring is represented by the dashed circle, b) schematic of the cell and c) a side view of the PEC cell with the electrolyte.[28]

the conductive layer and is protected by Teflon tape. The electrolyte is placed in a vessel on top and is confined using an o-ring made of a suitable material (such as Viton). This method also allows for post exposure characterizations in high vacuum (as epoxy is known to outgas when placed into a vacuum chamber) to be carried out without destroying the electrode. [28]

3.4 PERFORMANCE METRICS

To determine if a material is suitable for being a PEC electrode, several characterization techniques can be used to determine the crystallographic and electrochemical properties of the semiconductor. Table 3.1 covers the main techniques, although other characterization techniques can be used in conjunction for verification and supplemental information.

Table 3.1: List of PEC characterization techniques, with the information gained and limitation of each

Technique	Information Gained	Limitations
UV-Vis Spectroscopy	• Optical band gap. • Direct, indirect, allowed or forbidden transitions	• Data is prone to subjective errors and is not conclusive. • Derived band gap is not necessarily valid doe the surface
Illuminated Open Circuit Potential	• Flat Band Potential. • Conductivity type.	• Possible photocorrosion. • Samples with high recombination can prevent band flattening.
Three Electrode Voltammograms	• Saturated photocurent density. • Voltage range of photocurrent generation. • Conductivity type.	• Catalysts may be needed to minimize overpotential errors. • Possible photocorrosion.
Hall Effect	• Conductivity type. • Doping density. • Charge carrier density.	• Samples should be deposited on non-conductive substrates.
Incident Photon to current efficiency	• Wavelength dependant incident photon to current efficiency. • Absorbed photon to current efficiency.	• Errors in data if the lamp source is not accurately measured. • Possible photocorrosion or side reactions .
Two electrode photocurrent	• Solar to hydrogen efficiency .	• Possible photocorrosion or side reactions .
Solar to Hydrogen	• Efficiency for water splitting.	• Detection requires perfect sealing of the cell.
Stability Tests	• Lifetime of material.	• Instability of light source over time.

3.4.1 *Illuminated Open Circuit Potential*

The OCP can be used to estimate the flat band potential (F_{fb}) if the material does not have very fast recombination rates. A multimeter or potentostat is connected to the WE and the RE with all stray light excluded. The dark OCP is then recorded. The WE is then illuminated and the OCP is recorded. The OCP is plotted versus time. If there is a negative shift in the OCP, then the sample would possess a n-type conductivity. Fig. 3.6 shows the OCP of a n-type $GaInP_2$ electrode in a pH 2 buffer

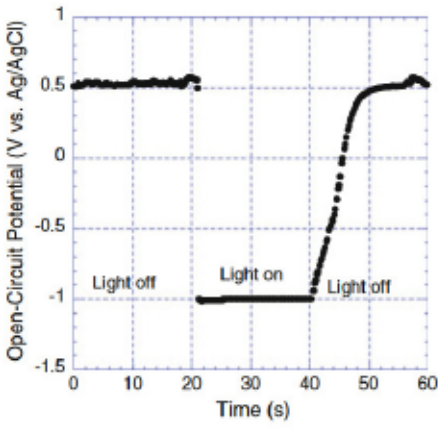

Figure 3.6: OCP of a $GaInP_2$ electrode in a pH=2 buffer. [28]

3.4.2 *Three Electrode Voltammograms*

While the eventual goal of a PEC device is the dissociation of water with two electrodes, in order to study the material properties of the photoelectode, a $j - V$ analysis in a three electrode configuration can be used. In addition, the flat-band potential can be determined.

First the conductivity of the device under test must be measured in order to determine if the electrode will act as a photoanode or photocathode. It is also necessary for the test to be carried out with

a small forward bias ($E < E_{fb}$) to avoid degradation though anodic (p-type) or cathodic (n-type) stripping. The potential at which HER or OER occurs is called E_{onset} and is the offset relative to E_{fb} and the required overpotential or drive the reaction. In reverse bias, a dark-current appears due to the lowering of the Schottky barrier, shunting of majority carriers or, reverse bias breakdown. [48]. Thus the voltage must be kept between $E_{dark-onset}$ and E_{onset}.

3.4.3 *Incident Photo to Current Efficiency*

The Incident photon-current conversion efficiency (IPCE) is the ratio of the photocurrent to the rate of incident photons. IPCE gives combined information on the efficiencies for photon absorption (η_{e^-}), charge transport from the solid to the solid-liquid interface ($\eta_{transport}$), and charge transfer across the solid-liquid interface ($\eta_{interface}$).

To perform a IPCE measurement in addition to the standard cell setup, a monochromatic and related optics (filters and a shutter) are required. The sample is measures at different wavelengths over time, with the illumination source having sufficient power to achieve an acceptable signal to noise ratio.

The general equation for calculating IPCE is:

$$IPCE(\lambda) = EQE(\lambda) = \frac{electrons/cm^2/s}{photons/cm^2/s} = \frac{|j_{pH}(mA/cm^2)| \times 1239.8(V \times nm)}{P_{mono}(mW/cm^2) \times \lambda(nm)}$$

3.4.4 *Solar to Hydrogen Efficiency*

The ultimate goal of a PEC device is the dissociation of water or the STH conversion efficiency. The short-circuited photocurrent density in a two electrode measurement is critical to determining the STH conversion efficiency. As well, any applied bias in a two electrode

configuration can provide important information on the material for the PEC material. If the applied bias is small ($0 - 0.1\,V$) modification to material itself such as tuning the band gap, using a surface catalyst or, change the electrolyte conductivity may be investigated. If the applied bias is moderate ($0.1\,V - 0.5\,V$) then integration into tandem structure might be an option. If the bias is large ($> 1.5\,V$) the photoelectode might require major changed to it's morphology.

Similar to a three electrode set-up the WE and CE are attached to a potentiostat and a voltage sweep is performed. A typical scan rate would be 10 to 100mV/s. Analysis of the data can be found from the steady state j_{SC} and the STH can be calculated by:

$$STH = \frac{j_{SC}(\mathrm{mA/cm^2}) \times 1.23\,V}{P_{total}\,\mathrm{mW/cm^2}} \tag{3.16}$$

For AM1.5G at one sun P_{total} is $100\,\mathrm{mW/cm^2}$ which most accurately estimates real world STH. This means that unlike solar cell, the only variable in the STH is the current produced.

3.4.5 *Stability Test*

The final test for a PEC device is stability. Photocorrosion is one of the most significant obstacles to overcome. During solar production, instead of driving OER and HER, the holes and electrons oxidize and reduce the semiconductor, causing physical and chemical changes. The test for stability is straight forward with only a few issues that could arise. The light source can overheat and the bulb may need to be changed if the test lasts of very long ($> 100\,h$) time. This can be mitigated by checking the test every 24 hours and having active cooling. Another problem is that with long term testing, the evolved

gas could cross over and over saturate the electrolyte, this can be mitigated by using a two compartment cell.

Testing itself involves a two electrode setup measuring the current density over time, with an applied bias if necessary. Starting at 1h to verifying if the electrode is stable, stability tests can be continues (24 hours or longer).

4

INSTRUMENTATION

4.1 PHOTOELECTROCHEMICAL CELL

The majority of the background theory of the PEC device is covered in Chapter 3, this section will cover the specific PEC device used. The cell is a three neck round bottom flask made from glass, the CE is a platinum sheet the RE is a $Ag/AgCl$ filled with a 3 mol KCl solution, and the WE consist of 9 different samples made of GaN, InN, InGaN, and ZnO. The light source is a 500 W halogen lamp with the output limited by a shadow box to allow light to strike the cell only. Fig. 4.1 shows the PEC cell without any of the electrodes, while Fig. 4.2 shows the spectral analysis of the light source compared to the $AM1.5$ spectrum. The spectrum of the light source peaks more into the visible spectrum of light, but is still appropriate for testing.

Figure 4.1: Photo of the PEC cell.

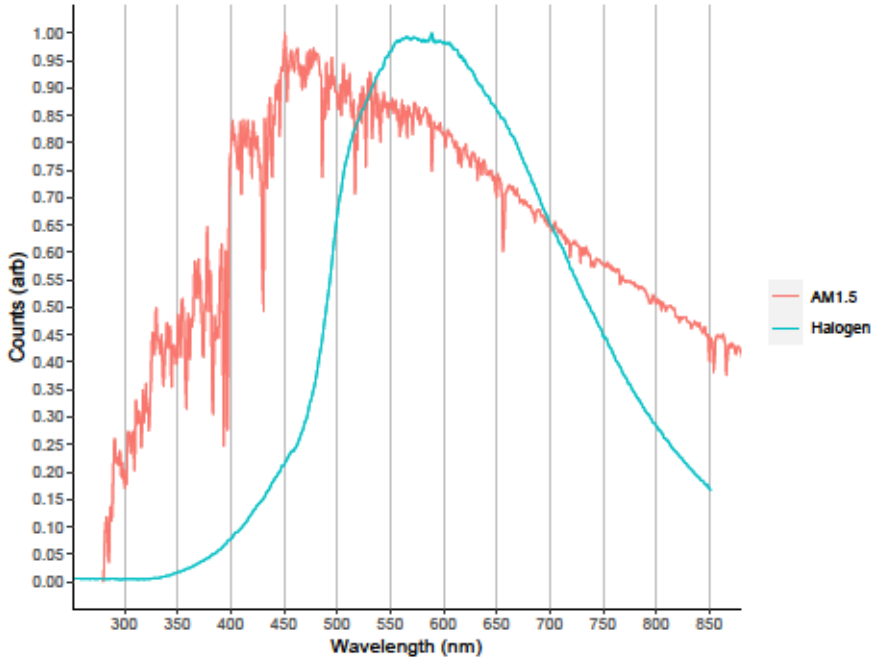

Figure 4.2: Spectral analysis of the halogen lamp as compared to AM 1.5.

The PEC cell used in TU Sofia was a vertical style cell. The sample was mounted at to bottom of the cell using a o-ring and to further reduce the diameter of the sample, a piece of silicon rubber with a $d = 1\,\mathrm{mm}^2$ hole was used. The sample was mounted to a copper sheet which served as the electrical connection to the potentiostat. The connection between the copper and the sample was accomplished though the use of a gold wire. The CE was a platinum sheet bonded to a platinum wire, while the RE was a Ag/AgCl electrode placed in a separate beaker but connected though a salt bridge.

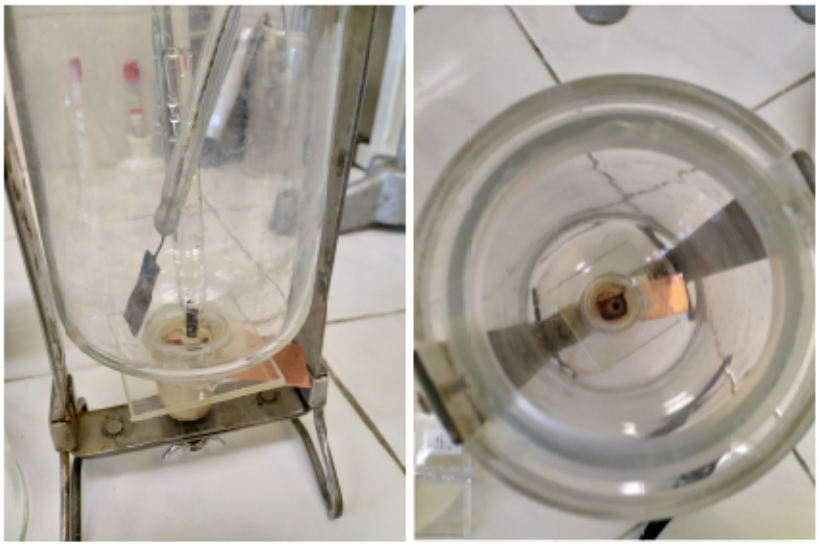

(a) (b)

Figure 4.3: a) Vertical cell used in TU Sofia with the sample at the bottom, and the CE and the salt bridge used by the RE, b) sample mounted in cell.

4.1.1 *Potentiostat*

The potentiostat used is a Keithly 2400 Source measuring unit (SMU) set-up in a four wire connection seen in Fig. 4.4 running a custom control software written in Python using the pymodule suite of commands. The code for the control of the SMU is recorded in Appendix A

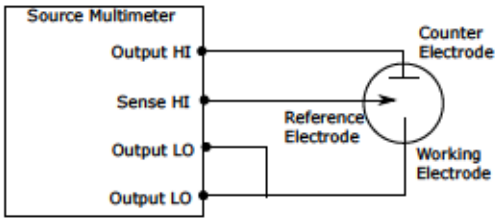

Figure 4.4: Wiring diagram for the source multimeter to act as a potentiostat.

The potentiostat used at TU Sofia was a commercial PalmSens4 potentiostat from PalmSens, with a $\pm 5\,V$ range and a maximum frequency frequency of 1 MHz. The software used by the PalmSens4 is supplied by the company, and is called PSTrace, operating in corrosion mode using a linear sweep voltammetry test.

4.2 LAKEHEAD SEMICONDUCTOR LAB REACTOR

Growth of the semiconductor layers can be done in a variety of different ways. The most common production methods for III-Nitrides are MOCVD, and Hydride Vapour Phase Epitaxy (HVPE). The vapour portion is a precursor to the one of the elements in the film. This precursor requires elevated temperatures to initiate the chemical reaction near the substrate surface to deposit the required materials. This thermal decomposition creates a concentration much higher than the vapour pressure of the material which causes the material to condensate onto the surface of the substrate. If the temperature of the substrate is high enough to completely decompose the precursors a diffusion current is created to grow the crystal. If the temperature is too low, the reaction will be limited by the thermodynamics of the precursor, this results in a decreased growth rate and increased surface roughness. The temperature can also be too high, where the deposited material desorbs and the observed growth rate is reduced. For both MOCVD and HVPE there is a stable temperature window where optimal growth exists. A

typical growth rate curve for GaN can be see in Fig. 4.5, where three distinct deposition zones can be seen. At low temperature the growth is limited by the precursors and a high temperatures decomposition and evaporation occurs. In the middle the gas transport is limited and the growth rate is stable and high.

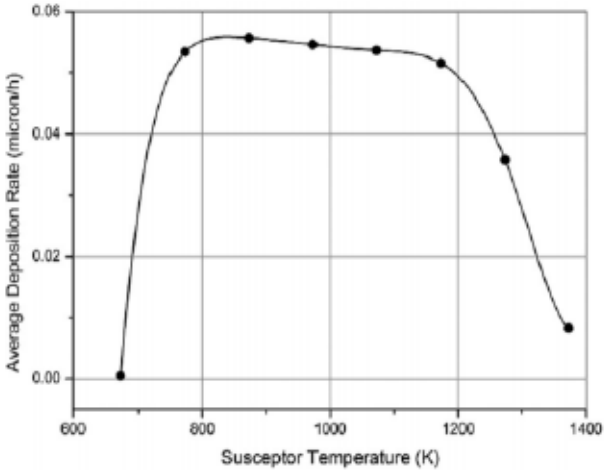

Figure 4.5: Growth rate curve for GaN. [59]

For commercial scale, HVPE and MOCVD are preferred due to the low vacuum conditions as compared to Physical Vapour Deposition (PVD), like MBE and sputtering, due to the long mean free path for the atoms to deposit on the substrates. These techniques rely on vaporizing elemental sources which require Ultra High Vacuum (UHV) ($< 10 \times 10^{-8}$ Torr), making it more difficult to scale reactor volume and more time to fully reestablish the vacuum after routine maintenance. PVD is also non conformal. The beam path coats in line of sight, Chemical Vapour Deposition (CVD) does not require a long free path as the reaction is driven by temperature gradients near the substrate surface. This allows for complex geometries to be coated including non-line of sight features. PVD is useful for research as it allows for lower impurities and a lack of process by-products, and the deep vacuums allow for electron diffraction tools such as Reflection High Energy Electron Diffraction (RHEED) for in-situ growth monitoring.

MOCVD is the most common technique for growth of III-Nitride layers. This technique allows for abrupt control of the layers for thin quantum well structures at the cost of lower deposition rates. In a MOCVD system, group III precursors,typically triethyl- or trymethyl-(aluminum, gallium or indium) gas, is mixed with a nitrogen precursor, typically ammonia(NH_3), to from the III-Nitride layer. Ammonia is used because N_2 is very stable ($N-H = 3.25\,\text{eV}$vs.$N = N = 9.80\,\text{eV}$[60]) so deposition with N_2 is not feasible. Other nitrogen precursors such as hydrazine ($NH_3 - NH_3$), methylamines ($NH_2 - CH_3$) and single precursors like dimethylgalium amide ($[(CH_3)_2GaNH_2]_3$) which can directly deposit GaN,[61]–[63] but ammonia continues to remain as the most common choice.

A typical growth for a III-Nitride begins with a thin (20-30nm) AlN layer on the substrate (typically sapphire but also (111) silicon) to produce a close lattice match layer between the substrate and the GaN layer. This is done by nitridating the sapphire at high temperatures[64] or a low temperature plasma exposure to form AlN (for sapphire) and SiN(for silicon) [65], [66]. Next a low temperature ($\sim 550\,^\circ\text{C}$) buffer layer is deposited which is then annealed at growth temperature ($\sim 1050\,^\circ\text{C}$). This low temperature growth induces Volmer-Weber (VW) island-like growth along the $11\bar{2}2$ facet. This growth allows for bending of dislocations towards the growth surface so that when they coalesce during growth they eliminate each other. Annealing above the growth temperature causes the surface bonds to break due to evaporation and local redeposition on the surface. [67] Finally a thick ($1-3\,\mu\text{m}$) GaN layer can be deposited to recuse substrate effects in the active layers.

Precursor flow rates are determined empirically by observing the characteristics of the grown layers, from surface roughness, crystallinity, carrier mobility and growth rate. Since decomposition of NH_3 is small and nitrogen has a high vapour pressure over the sub-

strate, III/V ratios are typically on the order of 4000 to lower nitrogen vacancies.[68]

The above however does not work for growth of InN. InN has a decomposition temperature of $\sim 450 - 500\,^{\circ}C$ where the In-N bond breaks and forms In_3O_2. This also poses a problem for NH_3 cracking, as temperatures must be $> 600\,^{\circ}C$ for efficient cracking. [69] A solution is to use a plasma system. This system could be an inductively coupled plasma (ICP), a microwave cavity or DC/RF capacitive plates. The increased reactivity of the nitrogen from plasma use is a benefit to film growth, however the excited nitrogen species mixed with the group III precursors can lead to gas phase reactions leading to powder formation of the substrate. This powder can be removed by a simple scotch tape adhesion text, ultrasonic cleaning or selective chemical etching, but may introduce impurities into the layer. Hydrogen introduction into the reaction chamber can help reduce the amount of carbon-nitrogen species formed. [70]

A second method to reduce powder formation is alternating the injection of precursors. This is referred to Migration Enhanced Epitaxy (MEE) for MBE and FME for CVD. [71]. The method is the same in both cases, group V precursors have high vapour pressures which leads to a need for rich group V conditions so that the surface is bombarded with N/P/As during growth. As such, it is possible for a migrating group III can combine with the group V atom before migrating to an appropriate edge or kink in the surface. Without high temperatures to increase migration distance, VW island-like growth occurs and rough surfaces filled with small grains appear on the layer. Separating the precursor injection stimulates island plus Stranski-Kranstanov (SK) layer growth, where crystalites grow on the $11\bar{2}2$ facet. This increased migration allows for the grains to expand two-dimensionally across the surface of the substrate before new layers are started.

Deposition in MEE and FME occurs by repeating a series of short growth loops which can be tailored to control composition. This alternating injections also allows for additional time for the group III precursors to migrate on the surface as the immobile nitride species cannot occur until the nitrogen injection. This has been shown to increase the crystal quality quality of the deposited layers. [72]–[75]

MEE and FME can also be adapted to Atomic Layer Epitaxy (ALE) where the growth surface is saturated during each cycle. This is achieved by isolating and purging the growth chamber for each precursor. The temperatures for this technique are intentionally low ($> 500\,^{\circ}C$) to avoids complete removal of the methyl groups of the group III precursors. This prevents additional precursors from coating the surface and self-limits the growth to one layer. This growth rate of one monolayer per cycle leads to very low growth rates which aren't suitable for device production, however growth of thin quantum well structures, gate oxides and passivization layers are easily done with this technique. [76]–[78]

The Lakehead Semiconductor Lab Reactor is a Plasma Assisted MOCVD which can be operated in MOCVD mode, FME mode and ALE mode. These growth modes can also be mixed by altering the structure of the growth recipe. Fig. 4.6 show the outline of the system used while Fig. 4.7 shows the gas delivery system connected to the Lakehead semiconductor reactor.

The plasma head is a modified hollow cathode capacitive plasma system. This means that the bottom plate which acts as the cathode has an array of holes patterned into it, with each hole acting as an aperture to the system. This enables generation of nitrogen radicals though the hollow cathode effect. [79] This system provide significantly higher electron densities compared to parallel plate systems. [80] This hollow cathode design can also be scaled by increasing the number of holes

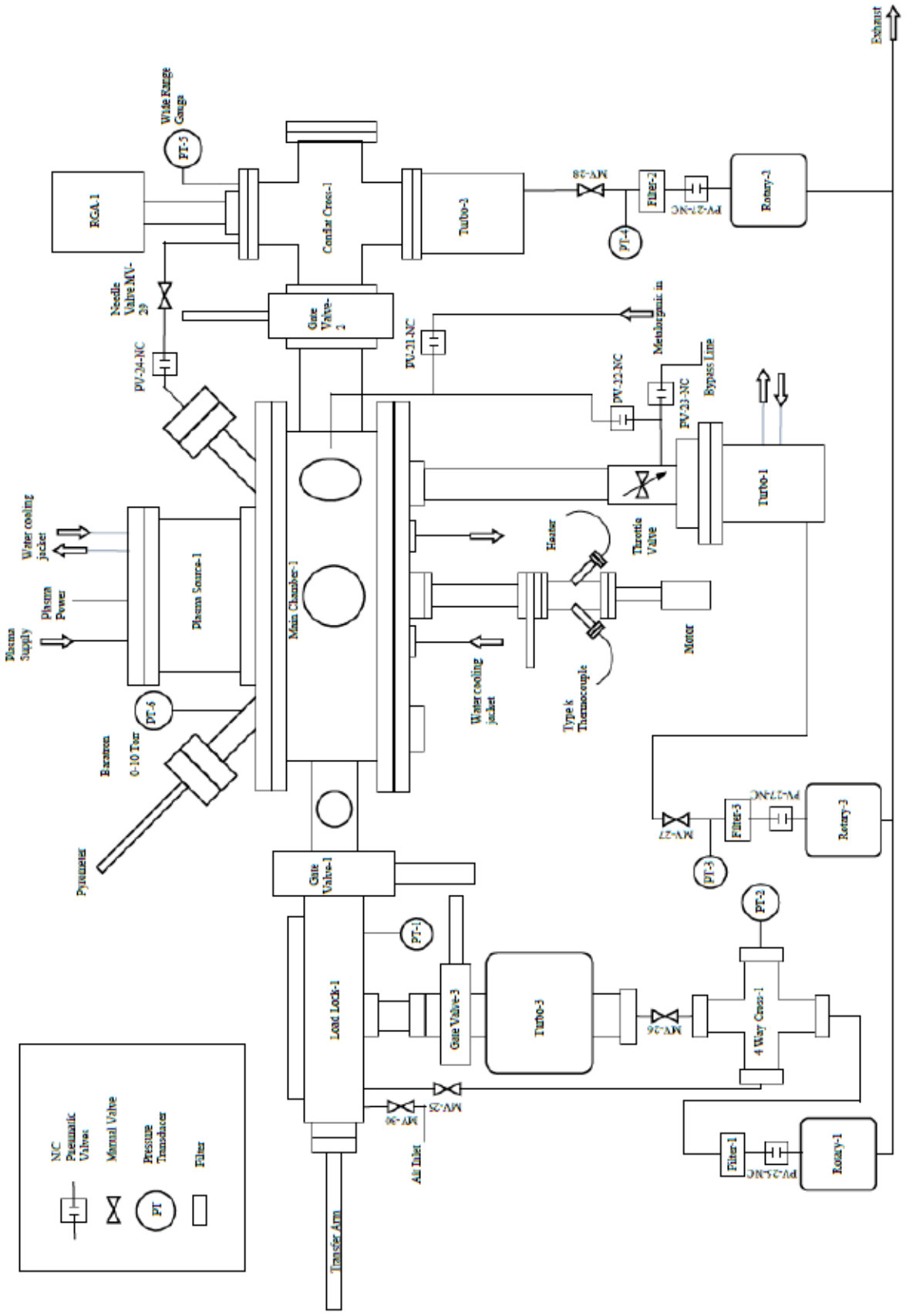

Figure 4.6: Block diagram of the Low pressure remote plasma MOCVD system at the Lakehead semiconductor lab.

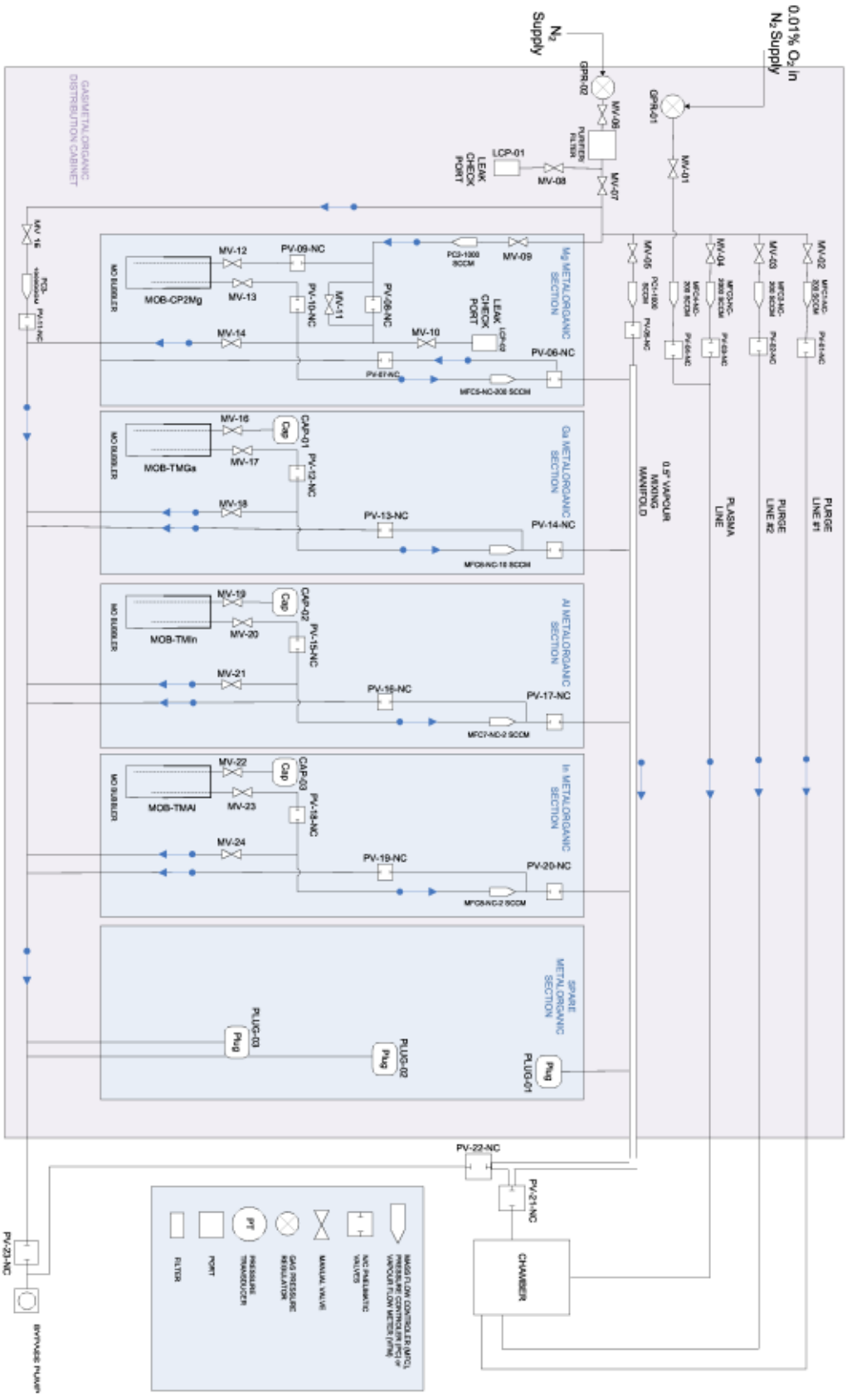

Figure 4.7: Block diagram of the Gas delivery system used in the Lakehead semiconductor lab.

in the array and avoids oxide contamination that come from the use of quartz windows. Fig. 4.8 shows the cathode and anode, the dimensions of which including the anode-cathode gap, along with the source-substrate distance are at fixed positions that determine the optimal operating pressure, which is determined empirically from experimental results.

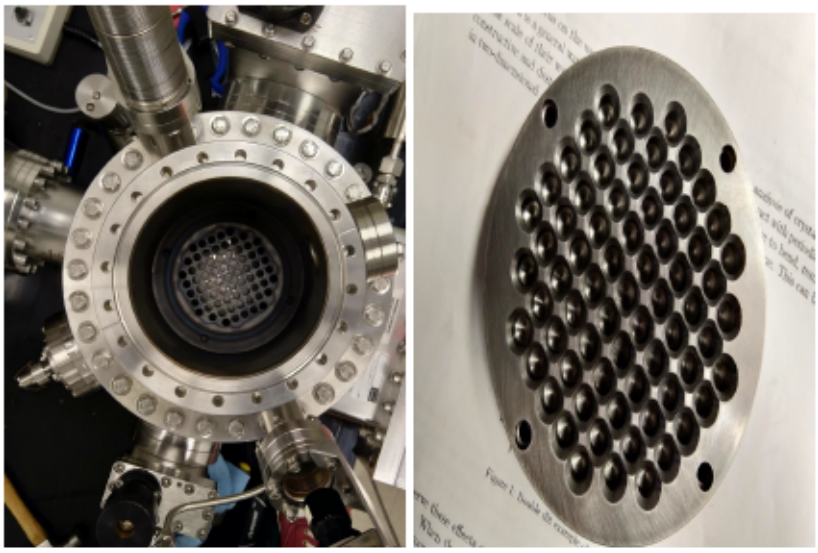

(a) (b)

Figure 4.8: (a) Cathode, (b) Anode

In this work, FME is combined with the hollow cathode plasma system. N_2 is used as the carrier gas for TMGa and TMI for gallium and indium respectively. N_2 also provides the backing pressure and source for the nitrogen plasma. The nitrogen is Praxair semiconductor grade 5N purity (99.99999%). The listed impurities are oxygen (1 ppm), water vapour (3 ppm), CO_2(1 ppm), CO(2 ppm), H_2(2 ppm) and various hydrocarbons (1 ppm). [81] The growth conditions have been optimized from previous work performed.

4.3 X-RAY DIFFRACTION

X-Ray Diffraction (XRD) is a non-destructive, non-contact method of determining crystallinity in solid samples. XRD relies on the constructive interference on scattered x-rays from the crystal lattice in the sample. The sample is placed in the path of a collimated beam of x-rays where the angle of incidence θ_i is swept over a range to determine which angles satisfy the Bragg condition.

Diffraction, in general, occurs when a wave encounters a series of regularly spaced scattering sites on the same order of the wavelength of the incident wave. The generated x-rays typically come from a copper tube ($\lambda = 1.5406\,\text{Å}$) held in a vacuum tube where high tension voltage is applied and the emission current is controlled. Silver ($\lambda = 0.56\,\text{Å}$) and Molybdenum ($\lambda = 0.71\,\text{Å}$) can also be used as the generating source for materials that fluoresce at the wavelength on the copper tube(such as iron). The high voltages are needed to drive L to K transitions for the wavelengths required for x-ray. Any additional x-rays can be filtered by lower atomic weight foils. Additional collimator slits and apertures are used to limit the beam divergence. For high resolutions application a fine bandpass filter can be used. Made of a single crystal (graphite or (220) Ge are the most common) input monochromator and an analyzer crystal on the output. Beam divergence can also be limited but including parabolic mirrors on the incident beam.

When the x-rays strike the surface of the sample, they scatter both elastically and inelastically. Inelastic scattering (Compton, Bremsstrahlung) leads to broad incoherent background noise in the detector while elastic scattering allows for observation of interference, dependant on the crystal structure and angle θ_i. The scan geometry used by the PANalytical X'Pert Pro used in this work can be seen in Fig. 4.9.

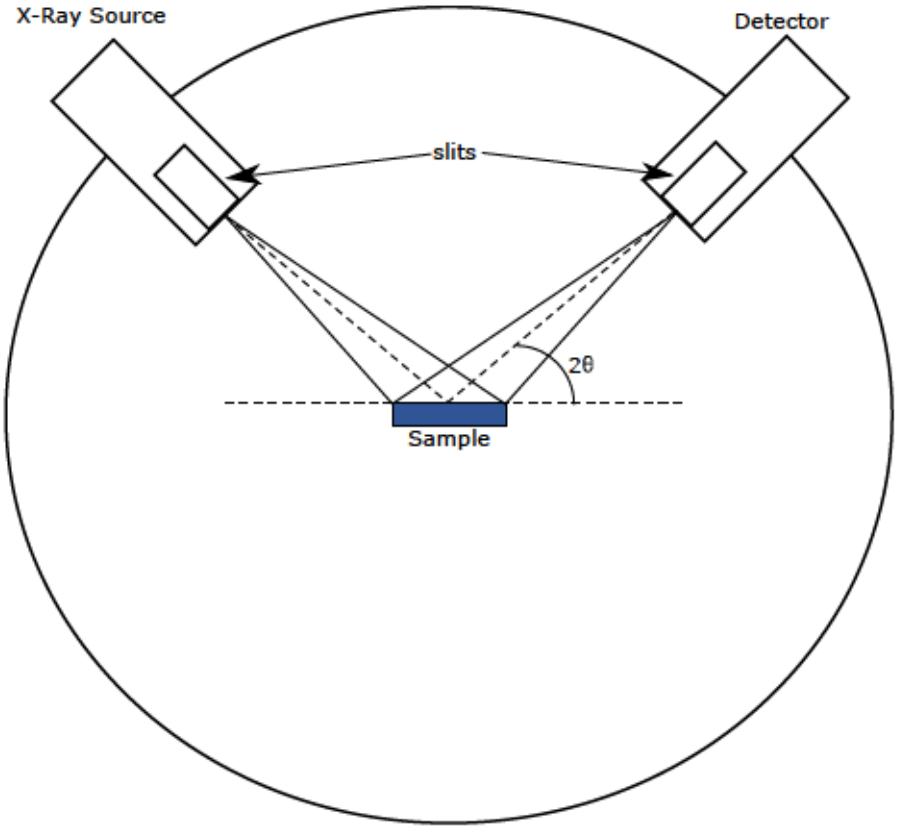

Figure 4.9: Bragg-Brentano goniometer used for XRD. Planes parallel to the surface are measured using a $\theta-2\theta$ can while the sample remains flat and the source and detector move at a constant rate.

The type of scan used in this work is a $\theta-2\theta$ scan where the sample remains flat while the source and detector move at a constant rate. While unable to produce a high resolution rocking curve or reciprocal space map, this type of scan provides information about the crystal unit cell and orientation. In order to determine information from this type of scan prior knowledge of the crystal cell is required and the application of the Bragg condition. All III-N and ZnO are Wurtzite (WZ) crystals and the miller indices can be found using Eq. (4.1).

$$\frac{1}{d_{hkl}^2} = \frac{4}{3}\left(\frac{h^2+hk+k^2}{a^2}\right) + \frac{l^2}{c_2} \tag{4.1}$$

Since WZ cell preferentially grow with the c-axis perpendicular to the surface the $000l$ peaks are compared between growths. The Bragg condition can be illustrated by Fig. 4.10.

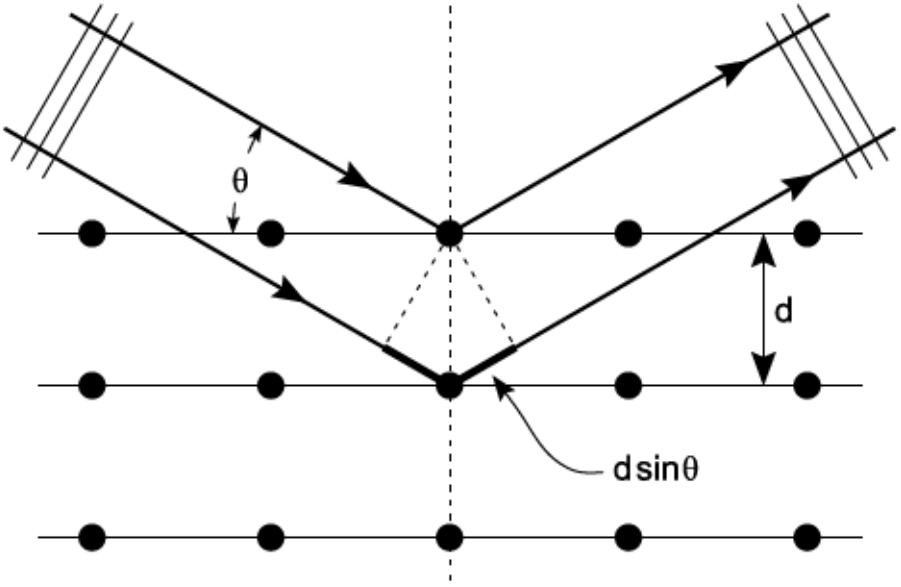

Figure 4.10: Bragg condition for x-ray diffraction. [82]

For constructive interference to occur, x-rays scattering off the sample must arrive in phase at the detector. Scattered x-rays from different planes within the crystal must therefore travel an additional $n\lambda$ so as to not disrupt their relative phase. As seen in Fig. 4.10 the length of the path which the x-rays must travel is $2d\sin\theta$. Therefore the Bragg condition is:

$$n\lambda = 2d\sin\theta \tag{4.2}$$

This observation is very easy to measure and control, whereas observing interplaner spacing on the order of 1 Å is difficult to observe.

4.3.1 *XRD Analysis*

Real crystals are not perfect and imperfections exist which disrupt the interference and thus broaden the distribution of the observed scattering centres. Given the volume probed by the x-rays, a statistically large numbers of d-planes are sampled and a Voigt profile is observed. A Voigt profile is the convolution between the Gaussian and

Lorentz distributions, which for most curve fitting analysis is a linear approximation between the two, referred to as Pseudo-Voigt. High quality crystals will have consistent spacing between the planes and a sharp peak will be observed. As the crystal become more disordered, the peak broadens until it is indistinguishable from the background noise. This broadening of the peaks is attributed to the shape or size related effects, with the shape effects contributing to a Gaussian like peak, whereas size effects contribute to a Lorentzian like peak.[83]

Analysis of the peaks is typically reported as the Full Width at Half Maximum (FWHM). The FWHM directly relate to the broadening of the crystal peak due to crystallite size, defects and impurities (both unintentional and intentional), alloy compositions and substrate induced strain. There is some additional broadening from the instrument as the beam diverges, but is largely ignored when comparing samples measured on the same instrument. For the $\theta-2\theta$ scans in this work, the broadening of the FWHM corresponds to strain gradients induced by the substrate and from impurity atoms, along with dislocations in the c-plane. As this scan does not directly measure tilt or twist of the grains, for which a high resolution rocking curve scan is needed, these types of defects cannot be reported. Therefore the lowering of the FWHM represents a reduction in the strain induced by the lattice mismatch and thermal mismatch between the substrate and the grown layer.

4.4 UV-VISIBLE SPECTROPHOTOMETRY

Ultraviolet-visible (UV-Vis) spectrophotometry is a quantitative analytical technique concerned with absorption of near UV ($180-390\,\text{nm}$) to visible ($390-780\,\text{nm}$) radiation. Light absorption as a function of the wavelength provides information about electronic transitions

occurring in the material. The amount of light transmitted is described by the Beer-Lambert law. The Beer-Lambert law relates to the optical attenuation as light travels though a sample. The transmittance or reflectance intensity (I) versus the incident intensity (I_0) is dependant on the path length (l) of the light through the sample, the absorption cross section (σ) of the transition, and the difference between the population of the initial state (N_1) and the final state (N_2) of the initial (E_1) and final (E_2) electronic energy levels.

$$\frac{I}{I_0} = e^{-\sigma(N_1 - N_2)l} \tag{4.3}$$

This is often simplified to the common form know as Beer's Law:

$$A = \epsilon c l = -\log_1 0 \left(\frac{I}{I_0}\right) \tag{4.4}$$

Where A is the absorbance, ϵ is the molar absorptivity, c is the concentration of the absorbing species and l is the path length of light through the sample. This can be further normalized to the path length of light though the thickness of the film to produce a absorption coefficient α. [47]

$$\alpha(\mathrm{cm}^{-1}) = \frac{\ln(10) \times A}{l(\mathrm{cm})} \tag{4.5}$$

UV-Vis spectrophotometers consist of a radiation source, a wavelength selection device, a sample compartment, a detector, and an output device. The radiation source can be a tungsten filament for visible light, a deuterium lamp for near-UV, or a Xenon flash lamp which covers the full spectrum from 185 nm to 2000 nm. The wavelength selection device is a grating monochromator, although for cheaper models a filter can be used. The sample compartment, for semiconductors is a holder with a narrow slit to allow all the incoming light to hit the semiconductor. Detectors can be photomultipliers, phototubes or in this case photodiodes. The most common optical configurations

for UV-Vis spectrophotometers are single beam and double beam arrangements as seen in Fig. 4.11. Single-beam instruments are cheaper, while double-beam is more convenient for spectral scans. A final configuration, which is used in diode array spectrophotometry, is having polychromatic light pass though a sample and is dispersed though a grating onto a linear diode array detector.

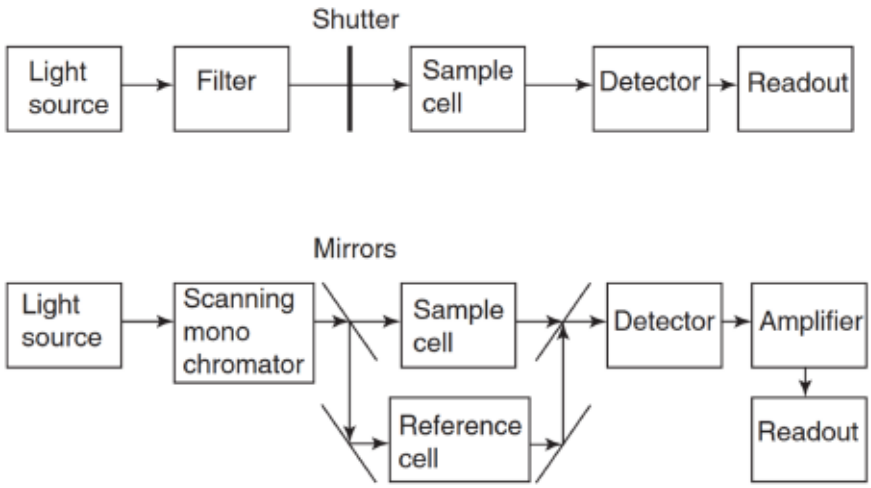

Figure 4.11: Block diagrams of single-beam (top) and double-beam (bottom) spectrophotometers. [84]

UV-Vis spectroscopy is a convenient method os estimating the optical band gap, since the electronic transitions between then valence band and the conduction band is probed. While the optical band gap is not necessarily equal to the electronic band gap, which is the difference between the valence band maximum and the conduction band minimum, it is often used as the there are not easy methods for measuring the electronic band gap. UV-Vis theoretically allows for the characterizations of electronic transition (direct of indirect) and also if the transitions are allowed or forbidden. The transitions can be observed by analysis of the absorption Tauc plots. Finally the **absorptance** ($A_{\%}$) is defined as the ratio of photons absorbed per photons impinging on the sample.

$$A_{\%} = 1 - \frac{I}{I_0} = 1 - 10^{-A} \tag{4.6}$$

For this work a Agilent Cary 50 UV-Vis spectrophotometer was used. The Cary 50, has a xenon flash bulb as it's light source, a Czerny-Turner monochromator, a holographic $27.5 \times 35\,\text{mm}$, 1200 lines/mm, blaze angle $8.6°at240\,\text{nm}$ grating, in a dual beam set-up with two silicon diode detectors with a wavelength range of $190 - 1100\,\text{nm}$ set-up to read absorbance with samples in transmission mode.

4.4.1 *UV-Vis Analysis*

In an ideal semiconductor, the UV-Vis spectrum has no absorption of photons below the band gap and a sharp increase of absorption above the band gap. Spectra are typically reported in units of wavelengths of light rather than energy. The conversion between wavelength (nm) and band gap energy (eV) is given by:

$$h\nu(\text{eV}) = \frac{h(\text{eV}\cdot\text{Hz}) \times c(\text{m}\,\text{s}^{-1})}{\lambda(\text{nm})} = \frac{1239.8\,\text{eV} \times \text{nm}}{\lambda(\text{nm})} \tag{4.7}$$

Band gap analysis involves plotting and fitting the absorption data to expected trendlines for direct and indirect band gap semiconductors. First A is normalized to the path length l of the light though the material to produce the absorption coefficient α as per Eq. (4.5). These are then plotted according to the relation developed by Tauc and supported by Davis and Mott. [85], [86]

$$\alpha h\nu \propto (h\nu - E_g)^{1/n} \tag{4.8}$$

where $n = 1/2,\ 3/2,\ 2,\ 3$ for direct allowed, direct forbidden, indirect allowed and, indirect forbidden respectively. These Tauc plots of

$(\alpha h\nu)^n$ vs $h\nu$ gives the optical band gap when extrapolated to the baseline. First, the minimum value of the plot is set to zero to account for wavelength-independent scattering. The absorbance is then analyzed using Eq. (4.5) for the absorption coefficient and then a Tauc plot is drawn with n being the correct exponent for the material. A tangent is drawn from the baseline and a line tangent to the slope of the linear region of the absorption onset is also drawn. Where the two tangents meet is the best estimate of the optical band gap.

4.5 SCANNING ELECTRON MICROSCOPE

SEM is used to image the surface or cross section of samples with high resolution in real time. The SEM used in this work is a Hitachi SU-70 Schottky Field Emission SEM capable of resolving 1 nm at 15 kV acceleration and is equipped with an Oxford Aztec 80 mm/124 eV Energy Dispersive X-Ray (EDX) and a solid state Back Scatter Electron (BSE) detector for back scatter imaging. In this work, the main application of the SEM is to acquire thickness profiles along the cross section of the samples for further use in Hall Effect and UV-Vis measurements, and to identify surface morphologies and chemical compositions using the EDX

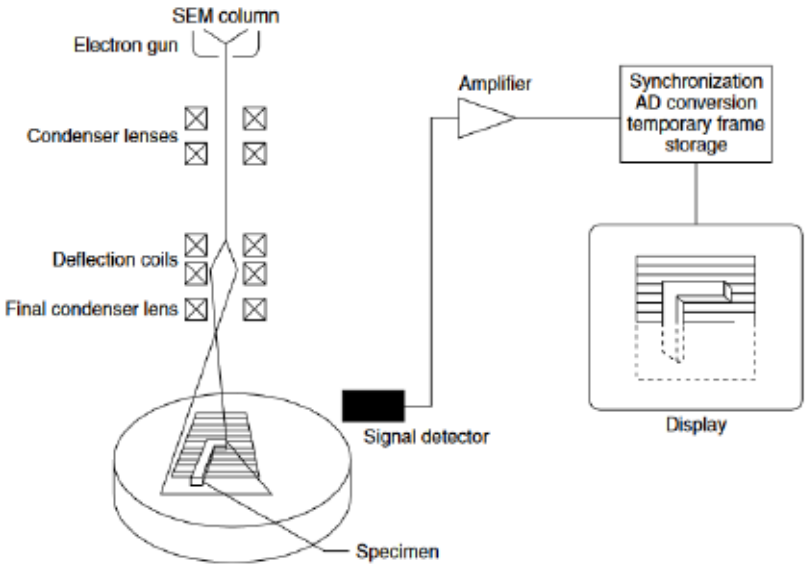

Figure 4.12: Schematic diagram of an SEM, showing the beam scanning and image formation. [87]

Fig. 4.12 shows a general schematic of an SEM. The electron beam is generated and focused and deflected onto the surface of the sample and scanned in a raster to generate an image. The electron beam also interacts with the sample surface in many different ways and produces many different secondary particles for analysis. The electron beam penetrates several µm into the material, as seen in Fig. 4.13

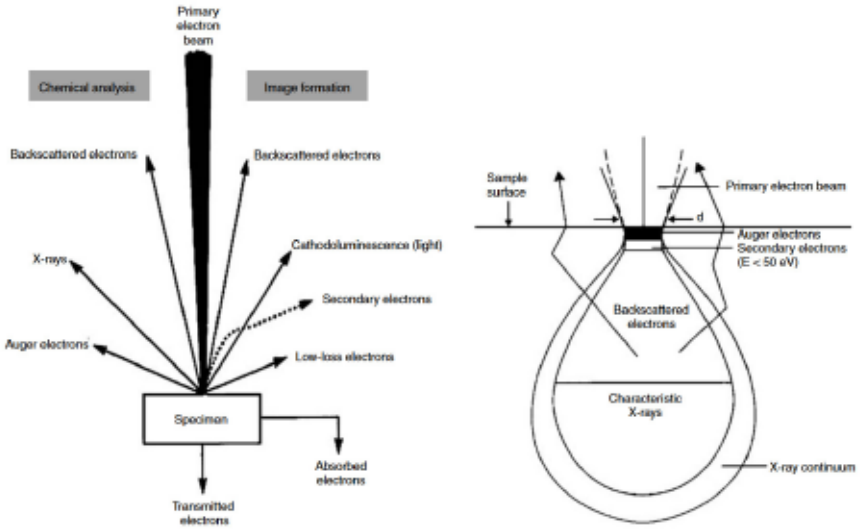

Figure 4.13: Signals generated by the SEM (left) and the excited volume with the generate signals (right) [87]

Secondary electrons are defined arbitrarily as electrons $\leq 50\,\text{eV}$ in energy. The depth of the secondary electrons vary depending on the sample and the accelerating voltage. Typically, $2 - 10\,\text{nm}$ for metals and $5 - 50\,\text{nm}$ for semiconductors. These are the most common due to their relative ease in collection, and because their signal is much stronger. Due to the low energy of secondary electrons, however, they cannot escape from very deep in the sample and their information is generally surface specific, allowing for high-resolution images of the samples.

Augur electrons are released within the first 5 nm of the surface and are characteristic of the surface chemistry. They are generated when core holes are filled from higher layers, the kinetic energy is equal to the hole filling transition energy minus the ionization energy of the atom, and require ultra high vacuum SEM to detect.

When the electron beam interacts with the sample, the beam can eject an electron from the samples inner electron shell. Rearrangements of the electrons in the ionized atom results in x-rays characteristic of the element they originated from. Since the x-rays penetrate significantly deeper into the material than electrons, the x-rays cannot be used to map the elements of the cross section, but can be used to sample the bulk composition of the layers.

Back scattered electrons are electrons that have undergone elastic of inelastic collisions with the sample and are reemitted with an energy less than the incident beam energy($\sim 50\%to80\%$ of the incident beam energy). The image generated by the back scattered electrons can be used to distinguish elemental composition based on atomic mass as the electrons generate contrast since the cross section is dependant on the atomic weight.

4.6 HALL EFFECT

The underlying working principle for the Hall effect (an example of which can be seen in Fig. 4.14) is the Lorentz force, which is a combination of the electric force and the magnetic force. When a charge q moves with a certain velocity $\vec{v}$ perpendicular to a magnetic field $\vec{B}$, it will experience a force proportional to its charge. In general this force is expressed as:

$$\vec{F} = q(\vec{v} \times \vec{B}) \tag{4.9}$$

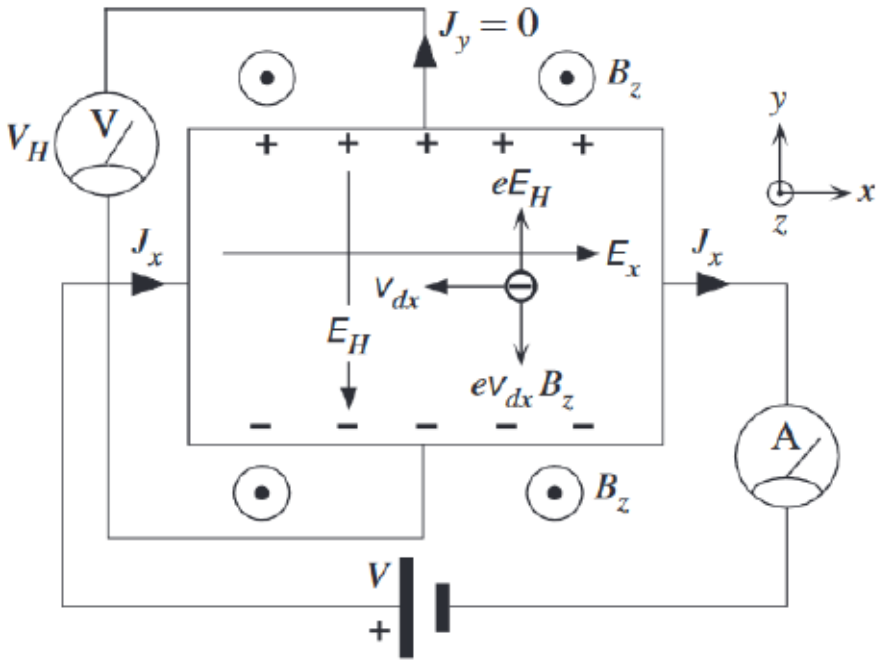

Figure 4.14: Schematic diagram of the Hall effect. the z-axis is out of the plane of the paper. The magnetic field is along the z-axis. [88]

In practice, the velocity of the electrons can be determined by measuring the current of a sample with known geometry. The current can be expressed as:

$$I = nWTqv_d \tag{4.10}$$

Where $W * T$ is the cross section area perpendicular to the current flow and n is the carrier density. While the electrons drift across the sample, the force of the magnetic field will deflect them. The magnetic field is always parallel or anti-parallel to the sample surface and thus the electrons will be deflected to the sample edges. This causes an accumulation of charge until the magnitude of the external magnetic force and the magnitude of the internal electrostatic force created by the charge accumulation are equal.

$$\vec{F} = q\vec{E} = q(\vec{v} \times \vec{B}) \tag{4.11}$$

With the magnetic field fixed perpendicular to the velocity, $\vec{B} = (0, 0, B_z)$ and current flow along the x-axis, $\vec{E} = (E_x, 0, 0)$

$$(\vec{v_d} \times \vec{B}) = v_d B_z \tag{4.12}$$

$$v_d B_z = E_x \tag{4.13}$$

A useful parameter call the Hall coefficient R_H is defined by

$$R_H = \frac{V_H}{IB_z} \tag{4.14}$$

R_H measures the resulting hall field per unit transverse applied current and magnetic field. The larger R_H, the greater V_H for a given I and B_z. Therefore R_H is a gauge of the magnitude of the Hall effect.

The Hall voltage can be further extended to find other properties of the semiconductor. By knowing V_H, I,B and $q = 1.602 \times 10^{-19}$ C (the elementary charge) the sheet density n_s can be found:

$$n_s = \frac{IB}{q|V_H|} \tag{4.15}$$

Finally, if the sheet resistance R_s is also known, then the mobility can be found as sheet resistance and sheet density are needed to calculate mobility:

$$\mu = \frac{|V_H|}{R_s I B} = \frac{1}{q n_s R_s} \tag{4.16}$$

The Van der Pauw technique for measuring the Hall voltage [89] is a easy and convenient way to measure both resistivity and Hall voltage. A simply connected (no holes or non-conducting islands) arbitrarily shaped sample connected by four very small ohmic contacts placed on the periphery (preferably in the corners) is used. A schematic of a rectangular Van der Pauw configuration is shown in Fig. 4.15.

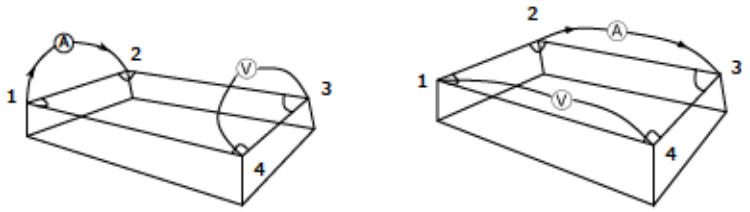

Figure 4.15: Schematic for resistivity measurements (a) $R_A = V_{34}/I_{12}$ (b) $R_B = V_{14}/I_{23}$

In a Van der Pauw configuration, there are two resistances R_A and R_B which are the vertical and horizontal resistances respectively. R_A and R_B are associated to the sheet resistance R_s though

$$e^{-\pi R_A/R_s} + e^{-\pi R_B/R_s} = 1 \tag{4.17}$$

For which, R_s can be solved numerically. A special case exists if $R_A = R_B = R$ where

$$R_s = \frac{\pi R}{\ln 2} \tag{4.18}$$

If the thickness d is known, then the bulk resistivity ρ can be calculated

$$\rho = R_s d \tag{4.19}$$

To calculate the Hall voltage using the Van der Pauw technique, the contact setup is shown in Fig. 4.16, current I is flowed though opposite pairs of contacts 1 and 3 and the Hall voltage is measured across contacts 2 and 4.

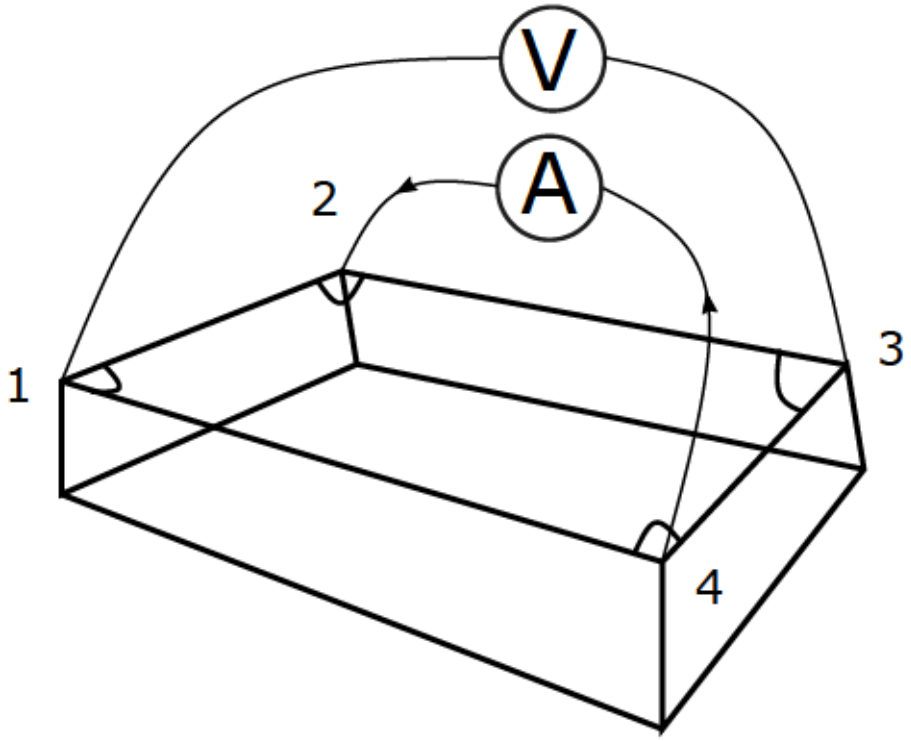

Figure 4.16: Schematic for measuring the Hall voltage using the Van der Pauw technique.

4.6.1 *Hall Effect Analysis*

In this work, a Ecopia HMS-3000 hall effect measurement system is used. The HMS-3000 allows for quick measurements of both resistivity (across all possible combinations for resistance) and eight different hall voltages (covering all possible combinations for current, voltage and magnetic field). There are eight possible combinations for resistance:

$$R_{21,34} = \frac{V_{34}}{I_{21}}, R_{12,43} = \frac{V_{43}}{I_{12}}$$

$$R_{32,41} = \frac{V_{41}}{I_{32}}, R_{23,14} = \frac{V_{14}}{I_{23}}$$

$$R_{43,12} = \frac{V_{12}}{I_{43}}, R_{34,21} = \frac{V_{21}}{I_{34}}$$
$$R_{14,23} = \frac{V_{23}}{I_{14}}, R_{41,32} = \frac{V_{32}}{I_{41}}$$

R_s can be calculated by averaging the resulting resistances into the two characteristic resistances and using Eq. (4.17) :

$$R_A = \frac{(R_{21,34} + R_{12,34} + R_{43,12} + R_{34,21})}{4} \text{ and } R_B = \frac{(R_{32,41} + R_{23,14} + R_{14,23} + R_{41,32})}{4} \tag{4.20}$$

The HSM-3000 used in this work uses a 1 T magnet for Hall voltage calculations. The Hall voltage is taken with the magnetic field in a positive and negative direction, the differences between the positive and negative magnetic field voltages give four Hall voltages:

$$V_{13} = V_{13,P} - V_{13,N}$$
$$V_{24} = V_{24,P} - V_{24,N}$$
$$V_{31} = V_{31,P} - V_{31,N}$$
$$V_{42} = V_{42,P} - V_{42,N}$$

Which are then averaged to give the overall Hall voltage

$$V_H = \frac{V_{13} + V_{24} + V_{31} + V_{42}}{8} \tag{4.21}$$

From there using Eq. (4.15) and Eq. (4.16) the sheet density and mobility can be calculated.

4.7 ATOMIC FORCE MICROSCOPE

AFM is a surface characterization tool, which measures the forces between the surface and scanning tip to image the samples topography. The AFM has three different regimes as seen in Fig. 4.17: a) If the tip is

far away from the surface the force between the tip and sample is negligible. b) For closer distances a negative (attractive) force between the tip and sample occurs. c) For very small distances, a strong repulsive force between the tip and sample occurs. A problem with case c) is that the tip-sample force, which is the measure signal, depends on the tip-sample distance (for one value of measure force, in regime b, there are two tip-sample distances, point 1 and 2 on Fig. 4.17) Care has to be taken to work only on one branch of the minimum force-distance curve.

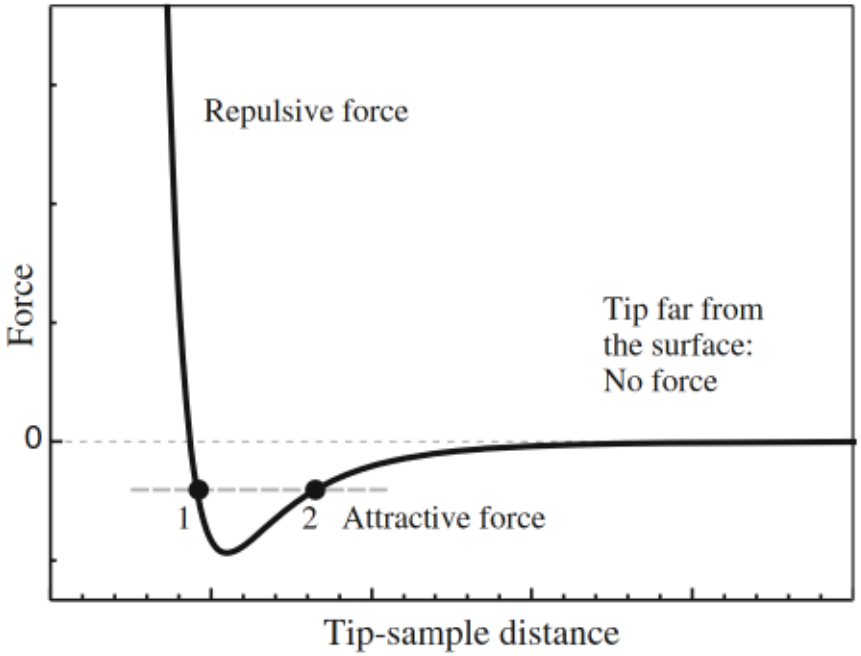

Figure 4.17: Force behaviour between the tip and sample as a function of tip-sample distance. [90]

AFMs consist of a cantilever, laser, photodiode and feedback electronics (as seen in Fig. 4.18). Cantilevers are made from silicon or silicon nitride. Silicon nitride cantilevers are silicon wafers with a thin silicon nitride film deposited by CVD. The cantilevers usually have a triangular point, which prevents torsional motion due to friction in contact mode. Coating the cantilevers in aluminum or gold provides

a high reflection coating to increase sensitivity of the optical beam detection.

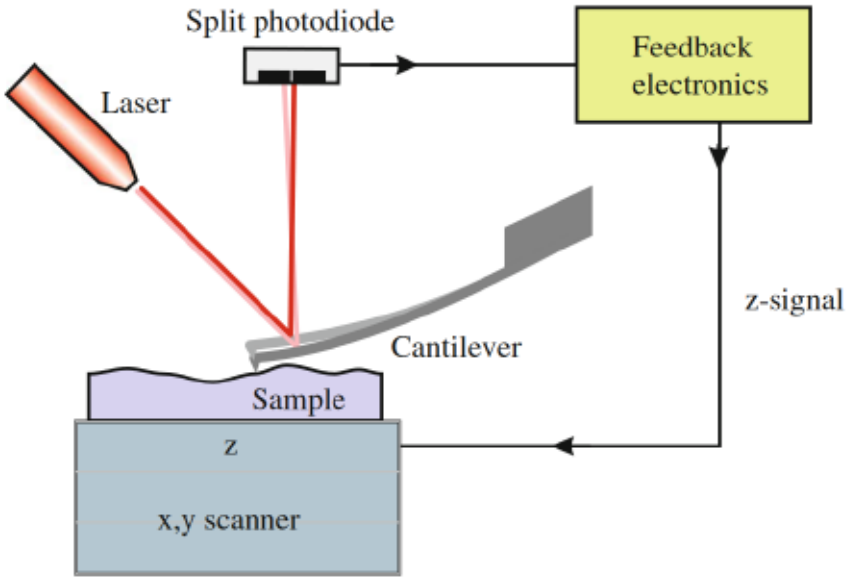

Figure 4.18: Schematic of the AFM with the minimum required components. [90]

Z movement is measured by a laser beam deflection. A laser is focused on the end of the back side of the cantilever where it is reflected into the photodiode. The bending is detected by a split photodiode (two diodes separated by a small slit). The difference in the optical signal is proportional to the angular deflection of the laser and therefore, proportional to the cantilever bending.

Movement in the x and y positioning is controlled by a piezoelectric flexure guide. A metal block with small trenches cut by wire EDM are shaped in a way to allow spring-like motion in one direction while being stiff in the other (with similar trenches to allow movement in the orthogonal direction). Piezo elements are employed to move the flexures.

There are two main types of measurements used for AFM. Contact (static) mode, where the static tip deflection is measure, and non-contact (dynamic) mode where the oscillation amplitude is measured. In both modes, a set point is given to the PID controller in the feed-

back system and a piezo element controls the tip-sample distance to maintain the set point as the cantilever is scanned across the sample. This set point is a force (for static mode measured in nN) or a % of the free vibration amplitude (for dynamic mode).

4.7.1 *AFM Analysis*

The Δz data is gathered from the difference in the split photodiode. As the the laser is deflected more into one photodiode, an error in the PID control loop is measured and recorded. The data is (typically) a square matrix of height values that the z-controller needs to adjust in order to maintain the set point. An RMS value (σ_{RMS}) for this is given as a statistical measure of the surface roughness. σ_{RMS} is calculated in the same way as a discrete time domain signal.

$$\sigma_{RMS} = \sqrt{\frac{1}{N}\sum_{n=1}^{N} |Z_N|^2} \tag{4.22}$$

Where N is the total number of points and Z_n is the height measured at point n. Since the RMS value only looks at the spread of the height and not the lateral dimensions the summation can be done in any order. This leaves a somewhat ambiguous description since the RMS value found can be represented by a sine wave which might not be representative of the surface. Therefore, the RMS value should not be blindly considered as the surface quality.

5

EXPERIMENTS

5.1 BAND GAP DETERMINATION OF INDIUM NITRIDE

As stated in Chapter 2, the band bap of InN has been widely debated. InN has generated a great deal of interest due to it's high electron mobility [91]–[93] and unique surface properties [94]–[96]. This high mobility makes InN suitable for high-frequency devices, but this has been limited by the low band gap.

Three different InN films (*S*1, *S*2 and, *S*3) were grown on sapphire substrates. The substrates were cleaned by sonication in acetone then methanol for 10 min, each at 50 °C. The substrates were then loaded into the chamber and heated to the growth temperature. The indium species was provided by trimethylindium (TMI) and the nitrogen species by a pulsed 400 W DC nitrogen plasma. The growth chamber pressure was held at 350 mTorr for all samples. The indium pulse length and the temperature are varied between each sample. Samples *S*1 and *S*3 were grown using an 8 s indium pulse followed by a 16 s plasma pulse at temperatures of 600 °C and 470 °C, respectively. Sample *S*2 was grown using a 16 s indium pulse followed by a 32 s plasma pulse at 600 °C. Pulse timings were determined though previous experimental results with a 1 : 2 ratio of indium to nitrogen being the best, while the temperature was chosen to be as high as possible while avoiding thermal decomposition in order to maximize adatom mobility. XRD, XPS, and SEM measurements were taken in the Lakehead University Instrument Lab (LUIL), while the XAS, XES,

and XEOL measurements were taken at the Canadian Light Source (CLS) in Saskatoon. Personal contributions to the investigations were development of the experimental recipes, measurement of the samples and as the leading author in the article.

5.1.1 *X-ray diffraction*

XRD measurements of each sample were taken to determine sample composition and crystallinity. The log-scale plot of the resulting sample measurements can be seen in Fig. 5.1. Several major peaks were observed on the XRD pattern of the InN layers. The peaks centred at 2θ 32°, 35°, 45°, and 56° are assigned to (100), (002), (004), and (103) planes of Wurtzite InN, respectively. These peak positions are in agreement with the existing literature [97], [98]. The diffraction peak for cubic InN (111) was not observed at around 31.2°, which shows that the layers have no cubic InN phase.

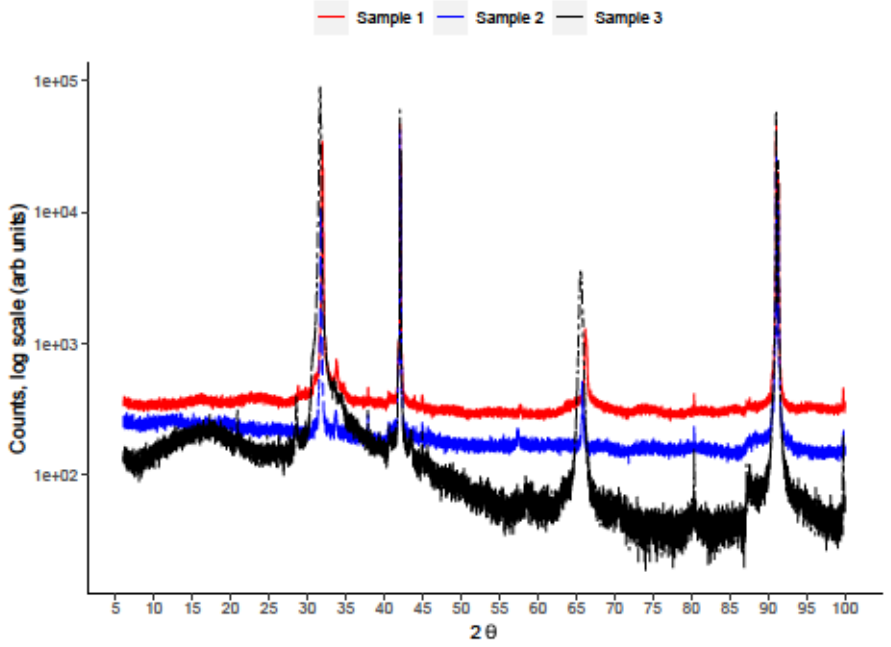

Figure 5.1: XRD patterns of InN samples (Log Scale) of samples S1 (red), S2 (blue), and S3 (black)

5.1.2 *X-ray photoelectron spectroscopy*

XPS spectra were collected for all elements present on the film surface and the $O1s$, $C1s$, $N1s$, and $In3d$ states were analyzed. All XPS measurements were collected using Al K_α 1486.6 eV. All spectra were charge corrected to the carbon peak at 284.8 eV and all spectral deconvolutions were done using the Kratos ESCApe XPS program using a Gauss Lorentz algorithm. Fig. 5.2 shows the $In3d5/2$, $O1s$, and $N1s$ spectra for sample $S3$. The $In3d$ shows the In–N peak (444.5 eV), the In–O (444.2 eV) and metallic indium (443.5 eV). The value of the In–N bond corresponds close to ion-beam deposited InN films [99]. The $N1s$ shows the In–N peak (396.5 eV) and a N–O peak (398.3 eV) coming from organic contaminants on the surface [100], which is also confirmed by the $N-O$ bond (535.0 eV) seen in the $O1s$ scan. $O1s$ scans indicate that the majority of the oxygen is due to adsorbed oxygen (531.8 eV) caused by surface contamination corresponding to a $O=C-N$ bond [101], with some amount of oxygen bonded to In.

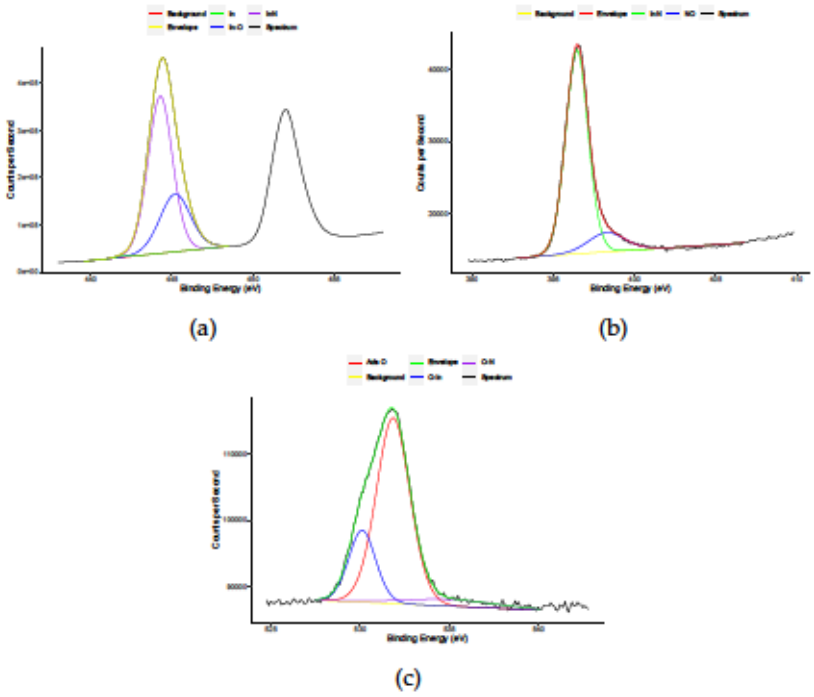

(a) (b)

(c)

Figure 5.2: XPS scans of sample S3 (a) In 3d 5/2, (b) N 1s, (c) O 1s.

5.1.3 *Scanning electron microscopy*

The morphology of the samples were investigated by scanning electron microscopy. Fig. 5.3a shows a needle-like morphology of sample *S*1. These needles are approximately 800 nm in height and 15 nm in diameter. Fig. 5.3b shows the rough film of *S*2 which consist of broken and stunted nanorods. Fig. 5.3c shows the thin film of sample *S*3. The thickness of this film is approximately 170 nm.

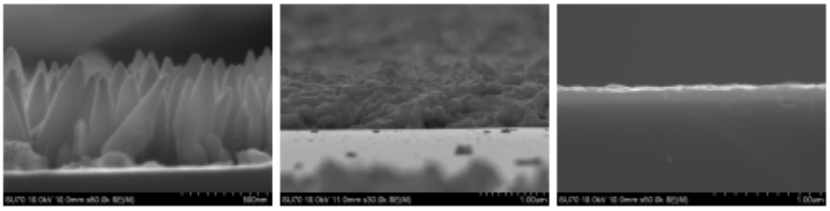

(a) (b) (c)

Figure 5.3: Cross-section SEM images of samples (a) S1 showing needle-like morphology, (b) S2 showing a rough film, and (c) S3 showing a thin film

5.1.4 *X-ray excited optical luminescence spectroscopy*

X-ray excited optical luminescence (XEOL) spectroscopy is employed to explore optical transitions, electronic structure, presence of defects, and luminescence properties of solids [102], [103]. The sample is excited with soft X-rays and the optical luminescence is registered by a spectrometer. Fig. 5.4 shows the XEOL spectra for InN thin films excited at 165 eV. The XEOL spectra are almost identical and exhibit two features at 689 nm and at 758 nm for all three samples. The electron energy transition interval is 1.56 eV which is due to the transition of electrons from the bottom of the conduction band of InN to the energy tail that is just above the top of the valence band of InN. This is caused by a oxygen atom substituting on a nitrogen site in the crystal lattice [104]. The broad luminescence feature at 758 nm corresponds to an

energy of 1.63 eV. The calculated electron transition energy of 1.56 eV in [103] is close to the measured 1.63 eV from the luminescence spectra for all samples. Based on the luminescence measurements and on the chemical content of the InN samples, there is oxygen in the samples, which substitutes on nitrogen sites and contributes to the tail. The luminescence feature at 689 nm, corresponds to an energy of 1.8 eV, is produced by the electron transitions from the conduction band to the valence band. Previous photoluminescence investigations also found band-to-band electron transition of InN at 1.8 eV [105], [106].

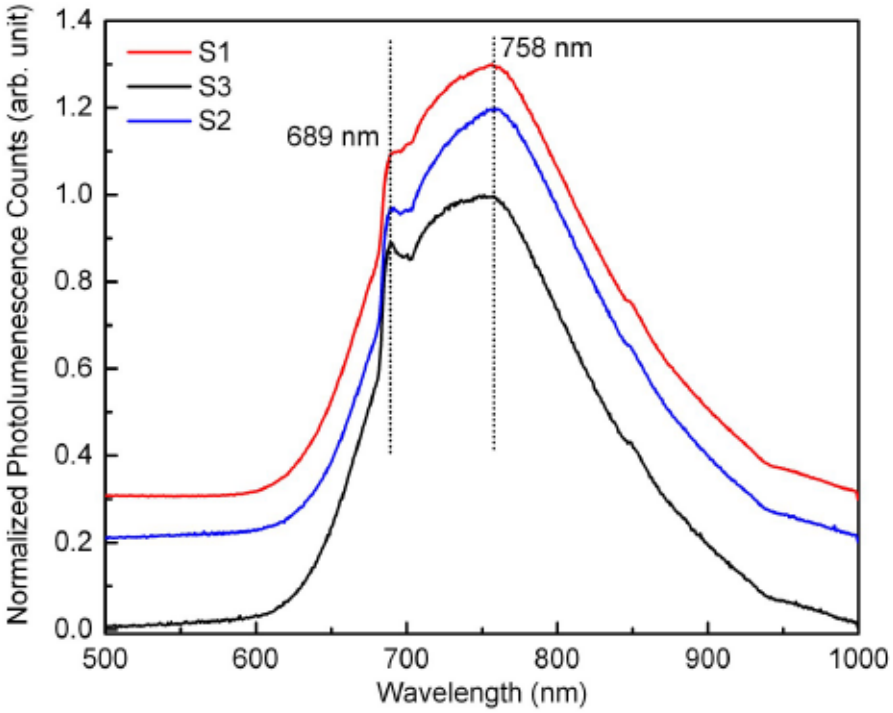

Figure 5.4: The XEOL spectra for *S*1 (red), *S*2 (blue), and *S*3 (black) InN thin films excited at 165 eV.

5.1.5 *N K-edge spectra and band gap measurements*

The XAS and the XES directly probe the conduction band (CB) and the valence band (VB) density of states, respectively. Fig. 5.5 shows the N K_α XES and 1*s* XAS spectra for the InN layers, along with a calculated Density Functional Theory (DFT) spectra. The DFT calcula-

tions were performed by partners at the university of Saskatoon using the WIEN2k software package [107]. The software package uses linearized augmented plane waves (LAPW) and augmented plane waves with local orbitals (APW + lo) to solve the Kohn–Sham equations. Fig. 5.5(b) shows that the XAS spectra for all samples are identical and have four distinct peaks located at 399.4 eV , 402.2 eV, 404.2 eV, and at 406.0 eV. Partial Density of States (pDOS) calculations have peaks at 399.4 eV , 404.2 eV, and at 406.0 eV which correspond to the N $p-$states, while the peak at 402.2 eV corresponds to In $s-$ and N $p-$states. The measured XAS spectra agree with the calculated core hole and ground state spectra. Fig. 5.5(a) shows two peaks at 390.3 eV and 394.0 eV. These peaks correspond to an admixture of N $p-$states and In $s-$states, and N $p-$states and In $p-$and $d-$states. The measured spectra are also compared to a calculated hypothetical Wurtzite $InO_{0.5}N_{0.5}$ and $InO_{0.0625}N_{0.9375}$. The measured spectra agree better with the $InO_{0.0625}N_{0.9375}$ meaning that there is only a small amount of oxygen within the layers. The calculated spectra are adapted from [108] and the method is described within the reference.

The second derivative of the XAS and XES can be used to determine the top of the valence band and the bottom of the conduction band respectively. The top of the valence band and bottom of the conduction band are measured at the first peak above the statistical noise from the upper edge of the XES and lower edge of the XAS as seen in Fig. 5.5(c) and (d) respectively. The band gap is found to be 1.80 ± 0.25 eV.

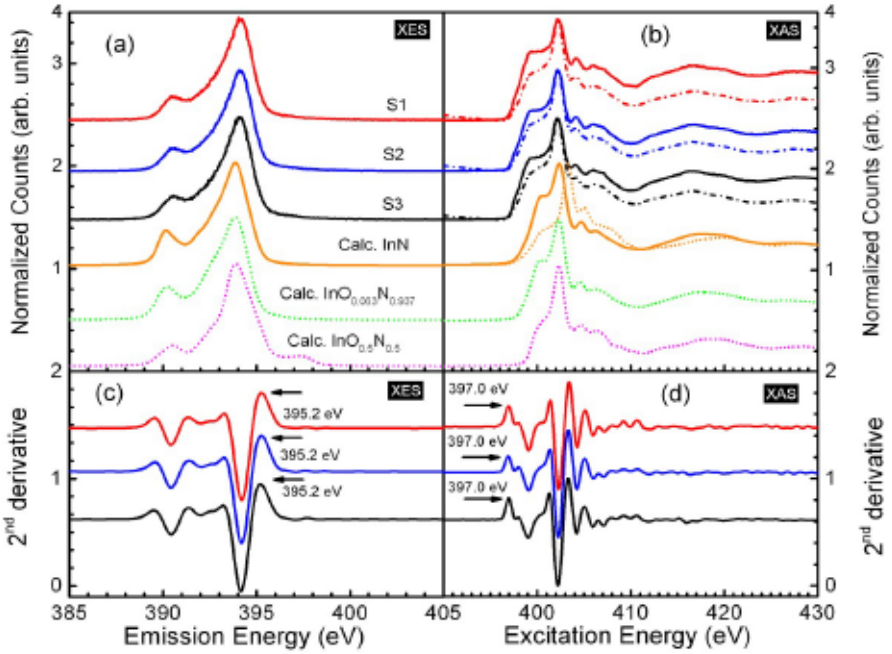

Figure 5.5: N K-edge XES and XAS spectra for *S*1, *S*2, and *S*3 InN thin films. (a) Experimental XES spectra of the InN layers are compared with ground state calculations for InN (orange), $InO_{0.0625}N_{0.9375}$ (dotted green), and $InO_{0.5}N_{0.5}$(dotted magenta). (b) Measured PFY (solid lines) and TEY (dash-dotted lines) for the InN layers are compared with core hole (solid orange) and ground state (dotted orange) calculations for InN and ground state calculations for $InO_{0.0625}N_{0.9375}$(dotted green), and $InO_{0.5}N_{0.5}$ (dotted magenta). Second derivatives of the XES and XAS spectra with peaks corresponding to valence band and conduction band onsets are indicated by horizontal black arrows in (c) and (d), respectively.

5.1.6 *O K-edge spectra and partial density of states*

To confirm the presence of oxygen impurities O K-edge XAS was performed. Fig. 5.6(a) shows the XAS spectra along with the calculated $InO_{0.5}N_{0.5}$ and $InO_{0.0625}N_{0.9375}$. The comparison between the measured and calculated spectra suggest that the $InO_{0.0625}N_{0.9375}$ spectra agrees more with the measured. The calculated spectra could be better matched if the calculations were for less than 6% but that would be too computationally expensive. There are three main peaks of the measured O K-edge XAS spectrum labelled I to III. These peaks are

assigned using the calculated conduction band pDOS of $InO_{0.5}N_{0.5}$ using GGA-PBE function seen in Fig. 5.6(b). Fig. 5.6(b) shows that mostly unoccupied O 2*p*-states contribute to peak I and peak II with weak admixture of N 2*p*-states and In 1*s*-states. The peak III is due to the admixture of In *p*−states, O p-states, and N *p*−states. Fig. 5.6(a) shows that the measured PFY spectra are not the same for the samples. This is because PFY is more sensitive to the bulk as it is governed by the attenuation length of the emitted photons which is larger (100 nm to μm) than that of the emitted electrons (<10 nm). TEY is more surface sensitive since the electrons are detected near the sample surface. Peaks I and II are almost absent in PFY mode for *S*1 as compared to *S*2 and *S*3, which would indicate that *S*1 has less oxygen impurities than the other two. Peaks I and II do show up in *S*1 in TEY mode, which mean unoccupied O 2*p*-states are present on the surface of the sample. This implies that oxygen atoms are substituting nitrogen atoms on the surface of the layers.

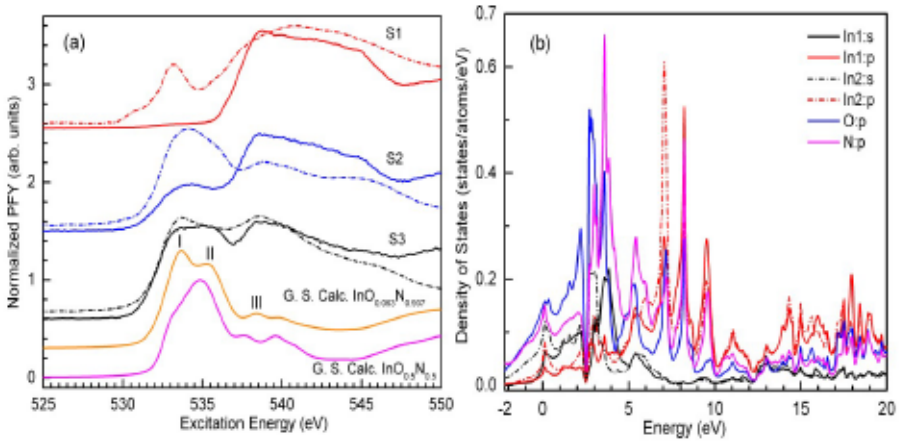

Figure 5.6: (a) O K-edge XAS spectra for the InN layers. The measured O K-edge XAS spectra of InN layers are compared with a calculated hypothetical Wurtzite-type $InO_{0.5}N_{0.5}$ (solid magenta) and $InO_{0.0625}N_{0.9375}$ (solid orange). The dotted lines are TEY mode and solid lines are PFY mode of InN. (b) The calculated partial density of states for $InO_{0.5}N_{0.5}$ using GGA-PBE functional. The energy zero is at the Fermi level.

5.2 PHOTOELELECTROCHEMICAL EXPERIMENTS

Ten samples were used for the experiments. They consist of different layers of GaN, InN, InGaN, and ZnO. Each sample was selected based on it's crystalline structure as found by XRD, and by it's mobility measured though the HMS-3000. All samples except for ZnO (dip coated on float glass) were grown on sapphire.

5.2.1 *Sample Analysis*

Samples 1 to 8 were grown in the Lakehead Semiconductor Research Lab Reactor, while sample 9 was grown though a dip coating process.

For the samples grown in the reactor a FME growth regime is used, first by introduction of the group III precursor followed by the group 5 precursor. The ratio between groups III and groups V are not completely the same as in a traditional system since both are not present in the chamber at the same time. The growth is instead divided into repeated cycles of group III rich conditions separated by group V plasma exposure. Thus the III/V ratio is controlled by the relative time of these two exposures in a growth loop. As it is desirable to have a large growth rate per hour, these cycles are kept as short as possible. Prior to all growths the substrates were cleaned in acetone in a ultrasonic bath for 10 min at 40 °C followed by the same in methanol followed by a rinse in distilled water then dried in clean compressed air before being loaded into the chamber.

5.2.1.1 *Sample 1*

Sample 1 is a layer of GaN on Sapphire. The sapphire was subjected to a 30 min DC plasma nitradation with a thin low temperature ($\sim$ 600 °C) GaN buffer layer before ramping up to the maximum

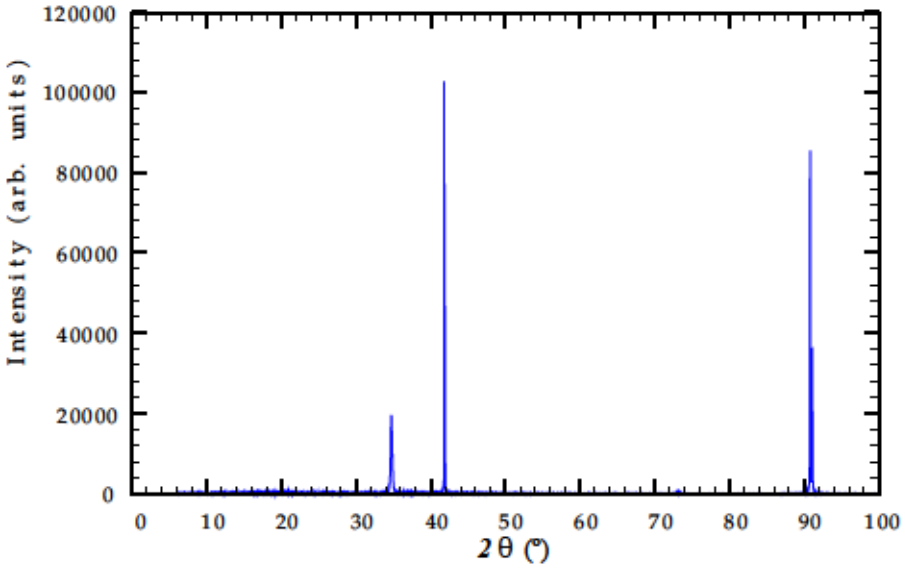

Figure 5.7: XRD of Sample 1.

temperature ($\sim 700\,^{\circ}C$), and the III/V ratio was 1 : 2 for both layers for a total of 1000 cycles. The mobility as measured by the Van der Pauw method is $5.262\,m^2/Vs$. Fig. 5.7 shows the XRD for sample 1. The peak 34.74° corresponds to the (002) peak of GaN, while the peaks at 41.82° and 90.81° are the (006) and (0012) respectively. The optical absorption edge measured from the Tauc plot (Fig. 5.8) is 3.23 eV with a thickness of 324 nm (Fig. 5.9).

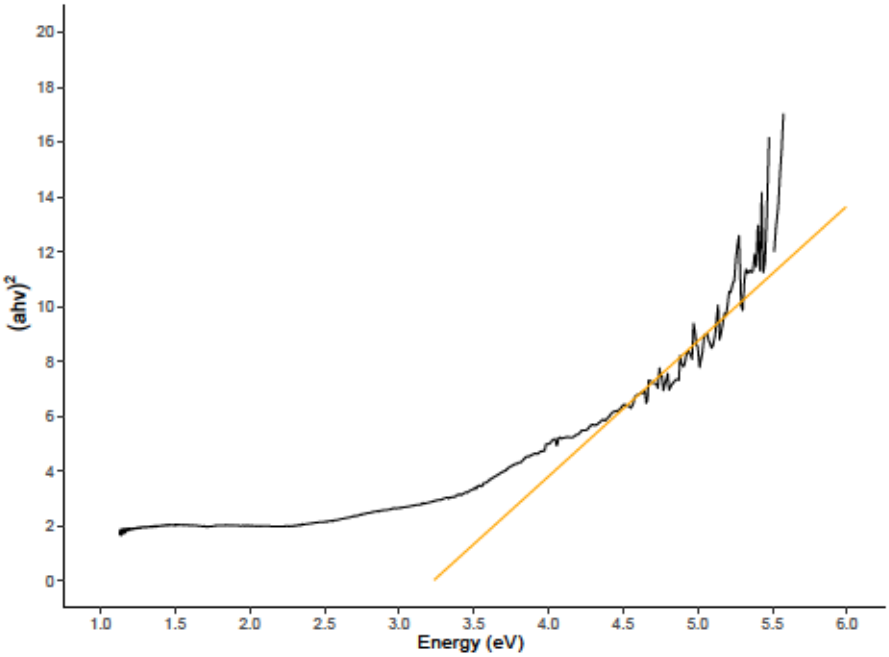

Figure 5.8: Tauc plot of Sample 1.

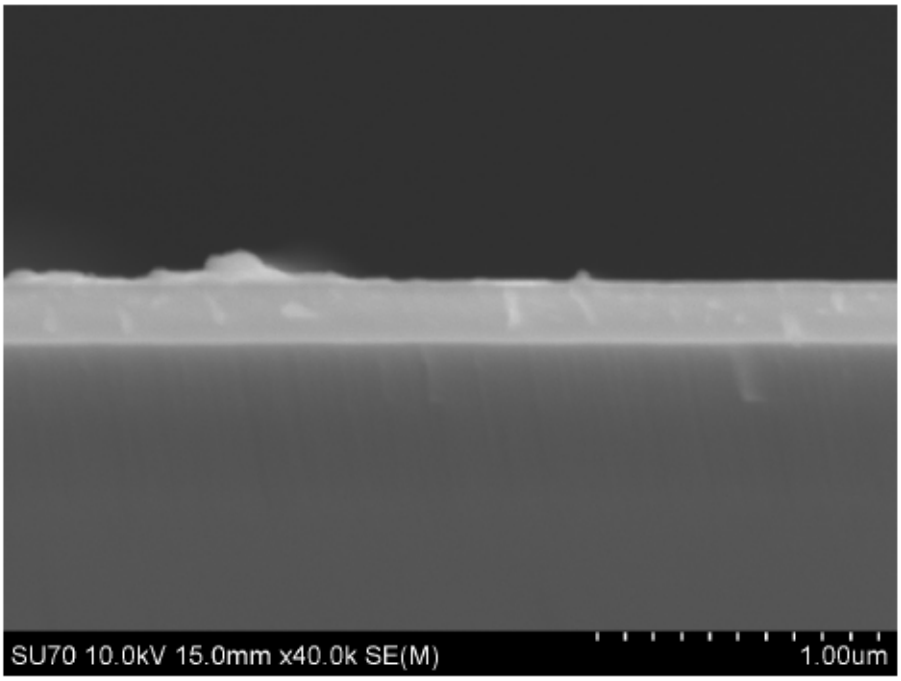

Figure 5.9: SEM of Sample 1.

5.2.1.2 *Sample 2*

Sample 2 was InN grown on commercially produced GaN on sapphire. The III/V ratio was 1 : 1 with a 60 s RF plasma nitradation. Every

20 cycles a 25 s nitradation was performed to convert any metallic indium on the surface to InN. For the first 800 cycles, growth was performed at 700 °C, and for the next 1600 cycles the temperature was dropped to 650 °C, finishing with a 15 min final nitradation. The measured mobility was 72.1 m^2/Vs and the XRD seen in Fig. 5.10 shows the peak at 31.61° corresponds to the (002) of InN while the peak at 34.84° corresponds to the (002) of GaN. The optical absorption edge measured from the Tauc plot (Fig. 5.11) is 1.11 eV with a thickness of 423 nm for the InN (the bright top layer in Fig. 5.12) and 2185 nm for the GaN (the middle layer).

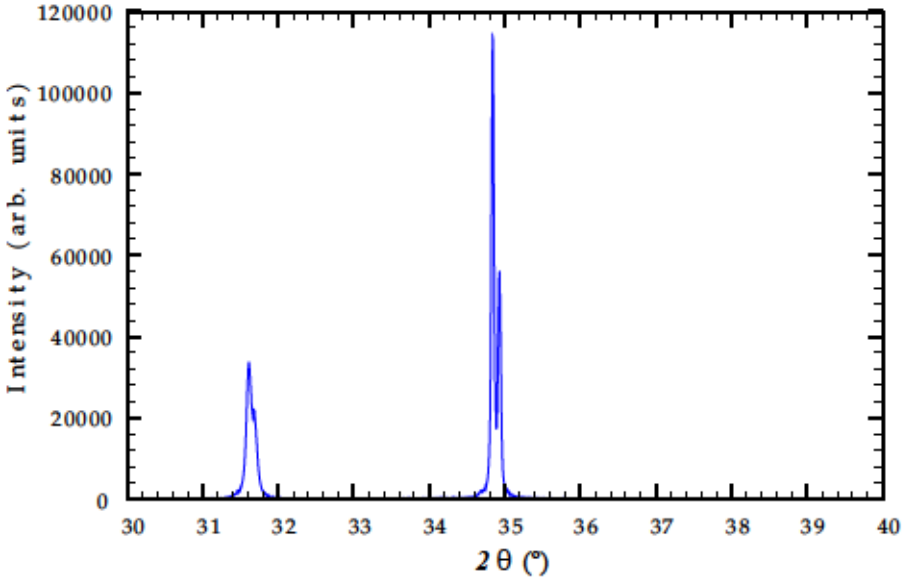

Figure 5.10: XRD of Sample 2.

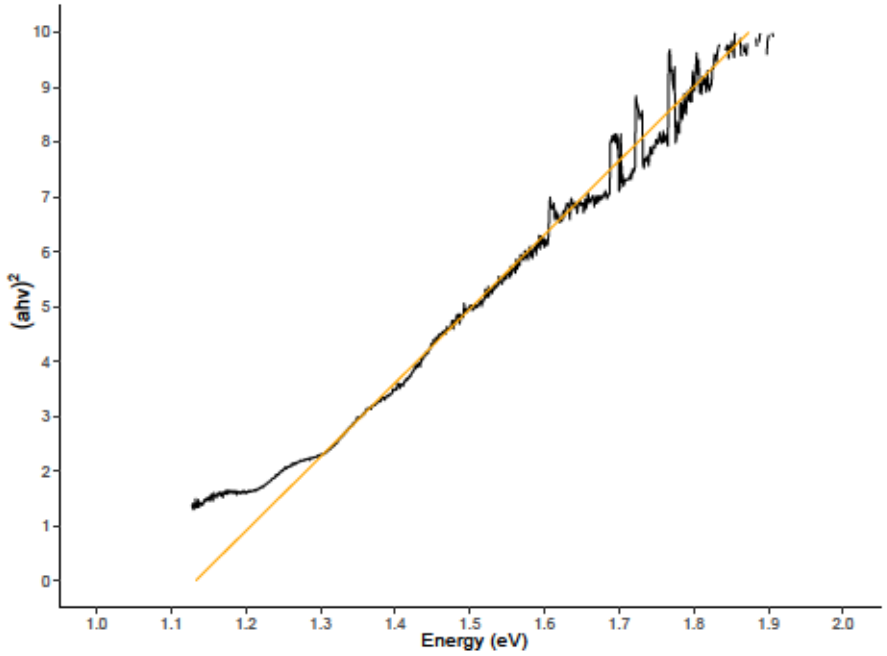

Figure 5.11: Tauc plot for Sample 2.

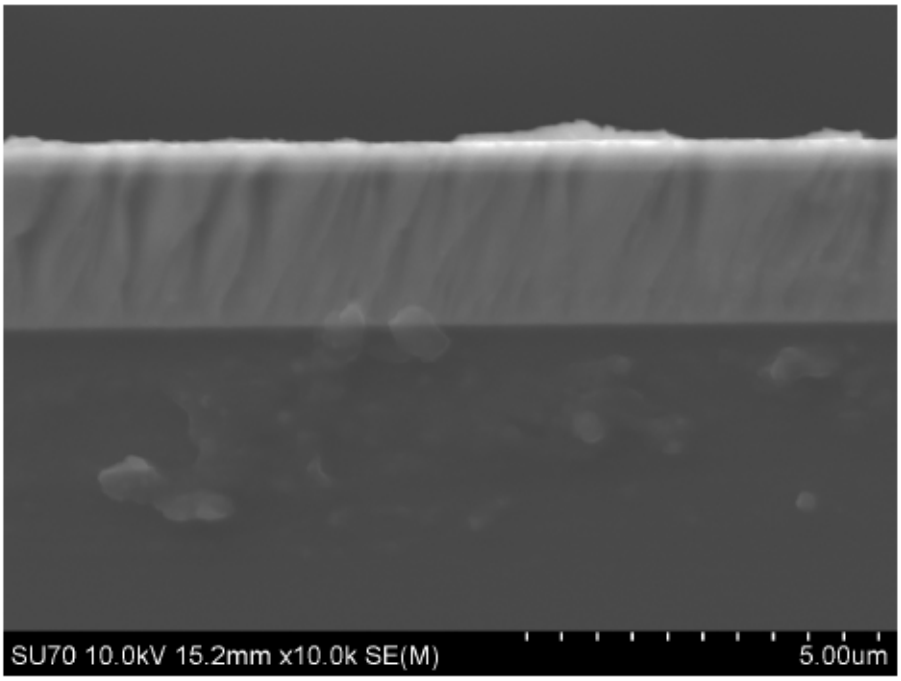

Figure 5.12: SEM of Sample 2.

5.2.1.3 *Sample 3*

Sample 3 was InGaN grown on sapphire. The III/V ratio was 1 : 2 for both the indium and the gallium. The theoretical percentage between

the indium and gallium is 50%. The growth temperature was 700 °C, and a 60 s nitradation was performed prior to growth. The InGaN growth cycle was set-up so that a monolayer of GaN was deposited before a monolayer of InN being deposited. The measured mobility was 40.7 m^2/Vs and the XRD seen in Fig. 5.13 shows peaks at 32.38° and 67.26° which correspond to the (002) and (004) of InGaN. The other two peaks are the sapphire substrate peaks as explained in Section 5.2.1.1. The optical absorption edge measured from the Tauc plot is 1.86 eV seen in Fig. 5.14, with a thickness of 822 nm which corresponds to a growth rate of 1.6 nm/cycle as seen in Fig. 5.15.

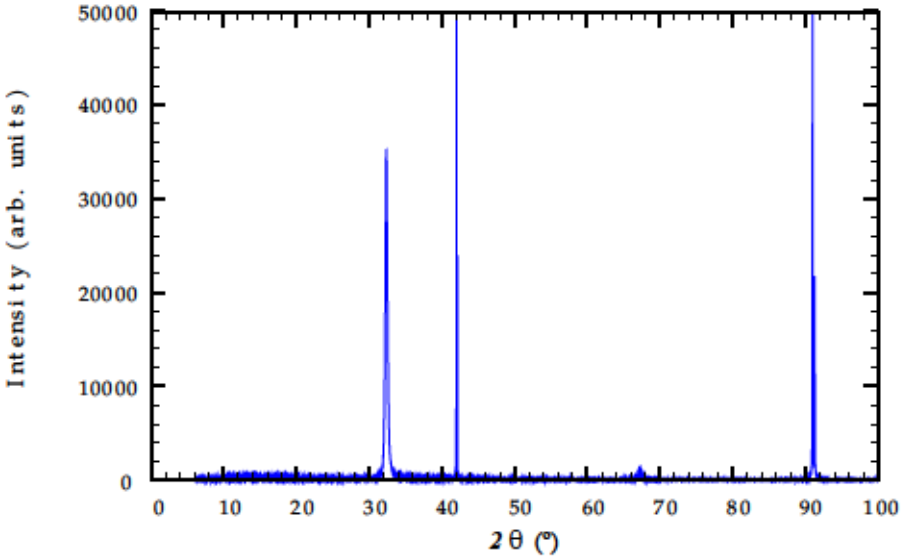

Figure 5.13: XRD of Sample 3.

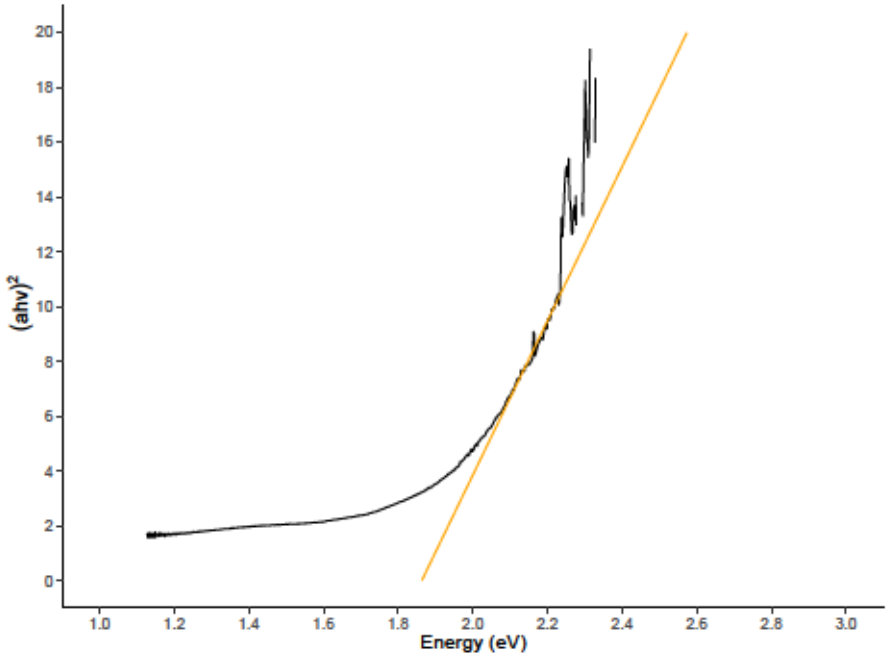

Figure 5.14: Tauc plot for Sample 3.

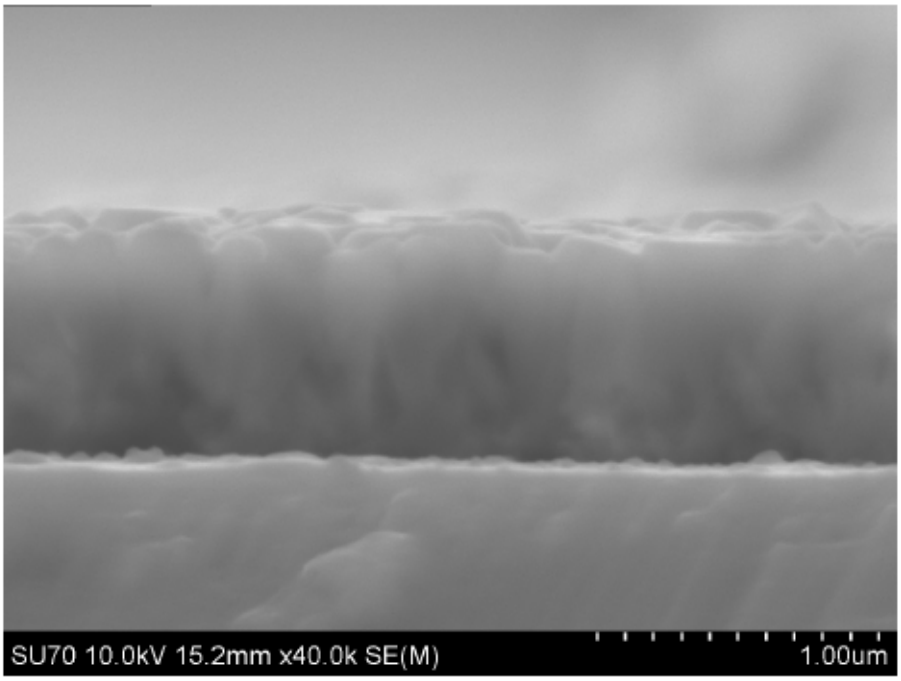

Figure 5.15: SEM of Sample 3.

5.2.1.4 *Sample 4*

Sample 4 was InN on GaN on sapphire. For the GaN growth, the III/V ratio was 1 : 2 while for the InN the III/V ratio was 1.1 : 1.4.

The sapphire was treated to a 30 min nitradation before a 30 min anneal at $\sim$ 700 °C. The GaN layer is only 100 cycles thick to act as a buffer layer for the InN. After the GaN growth, the sample was cooled to 650 °C for the InN growth. Every 20 cycles a mid-growth nitradation was preformed to convert any unreacted indium to InN. The measured mobility of the InN was 36.5 m^2/Vs, the XRD seen in Fig. 5.16 has peaks at 31.56° and 65.53° corresponding to the (002) and (004) of InN, while the peak at 34.68° corresponds to the (002) of GaN. Fig. 5.17 shows the Tauc plot for Sample 4, with the optical edge at 0.78 eV and Fig. 5.18 shows the BSE SEM of Sample 4. This was used to differentiate between the InN layer (the top layer at 334 nm) and the GaN (the bottom layer at 187 nm).

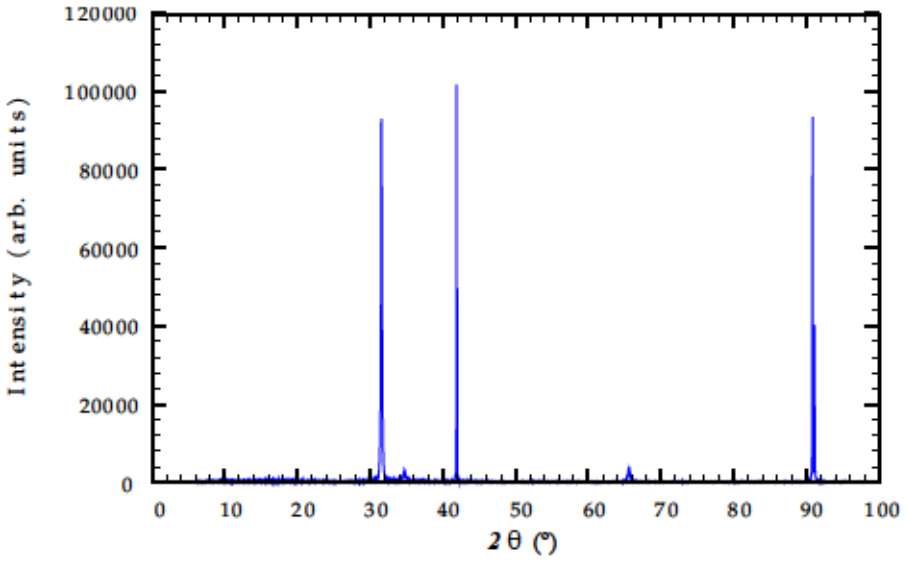

Figure 5.16: XRD of Sample 4.

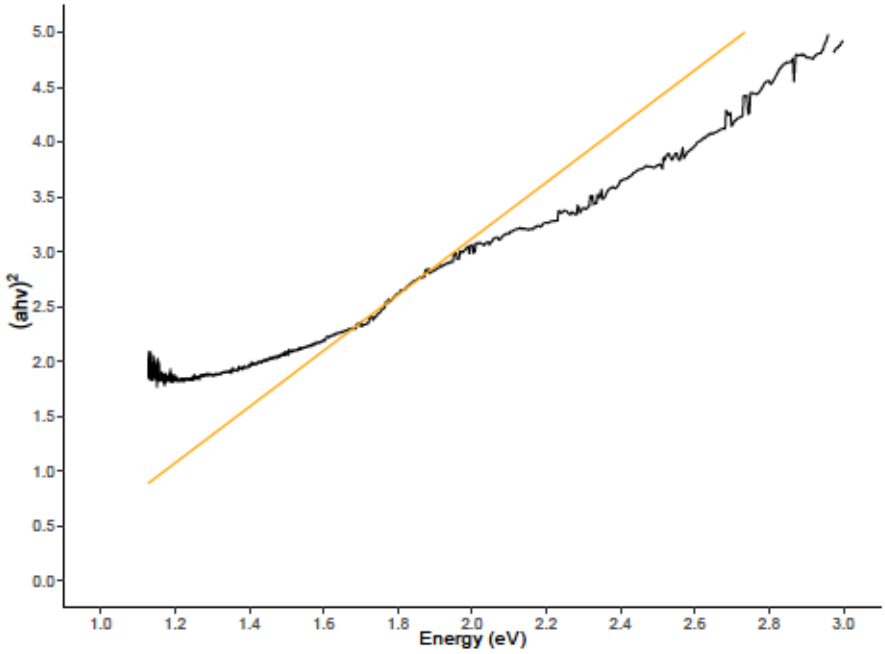

Figure 5.17: Tauc plot for Sample 4.

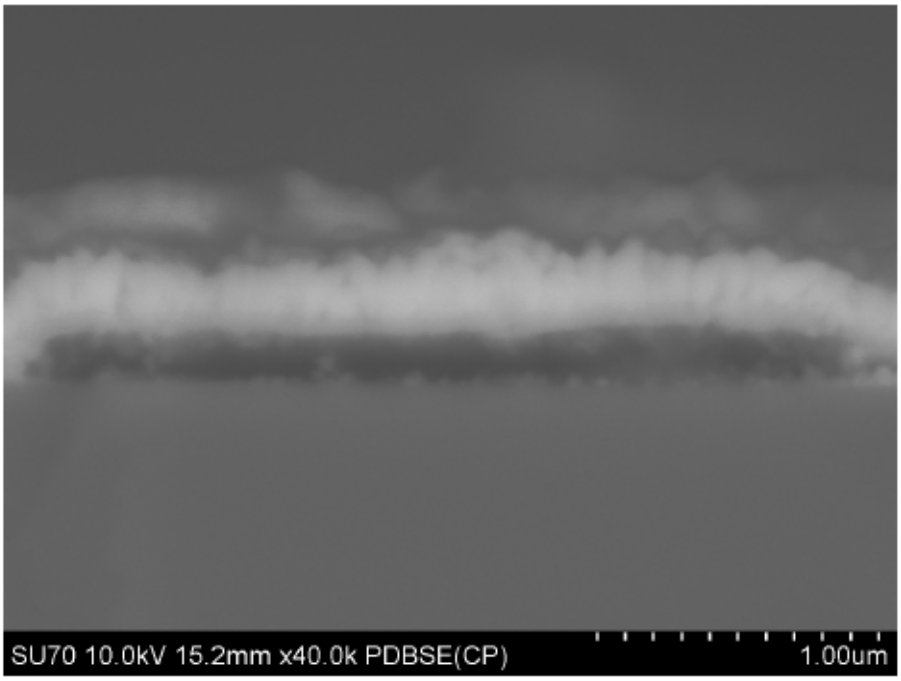

Figure 5.18: SEM of Sample 4. The BSE is used in order to differenate the layers.

5.2.1.5 *Sample 5*

Sample 5 was GaN on sapphire. The III/V ratio was 1 : 2 and growth was at $\sim 700\,^{\circ}\mathrm{C}$. A thin (100 cycle) low temperature buffer layer was deposited at 640 °C. The measured mobility was $106.8\,\mathrm{m}^2/\mathrm{Vs}$ and the optical absorption edge is 3.5 eV. The XRD seen in Fig. 5.19 shows a (002) peak at 34.73° and a (004) peak at 73.09°. The measured thickness is 494 nm(Fig. 5.21).

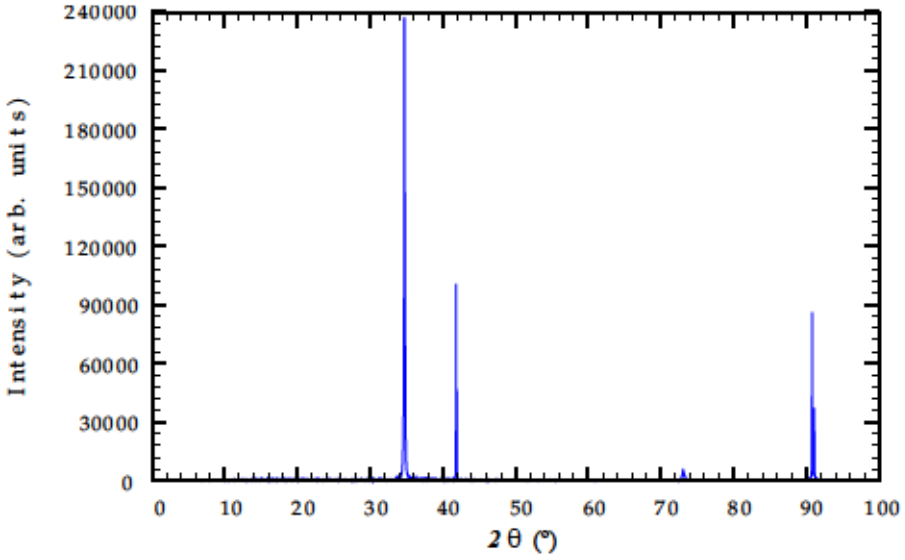

Figure 5.19: XRD of Sample 5.

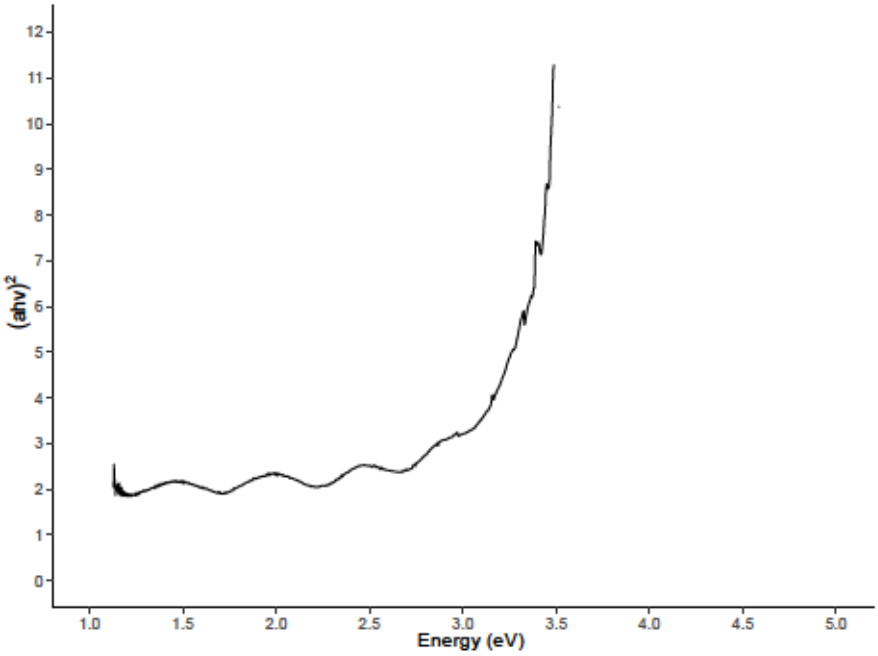

Figure 5.20: Tauc plot for Sample 5.

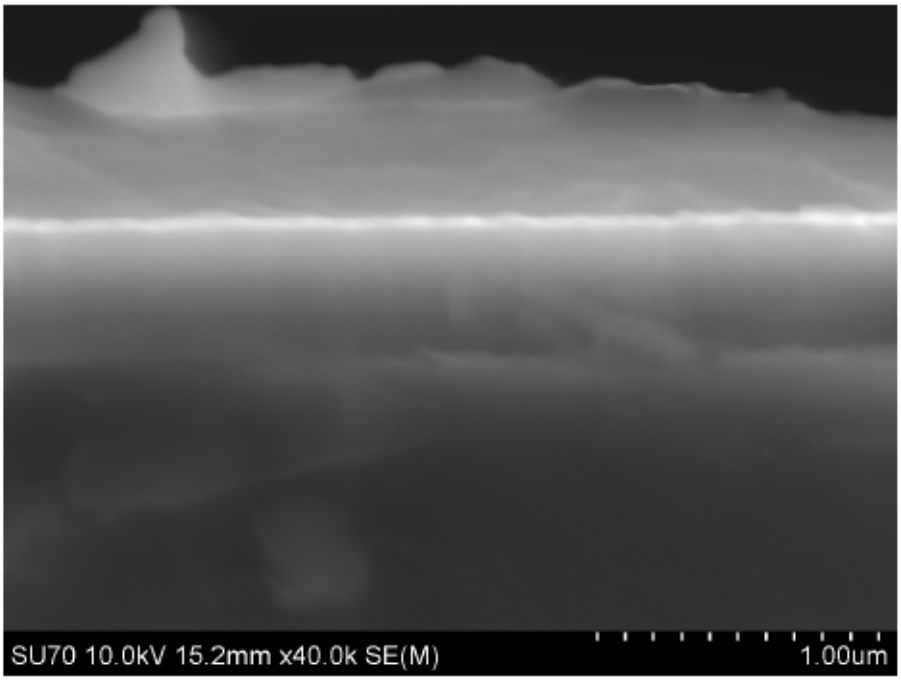

Figure 5.21: SEM of Sample 5.

5.2.1.6 *Sample 6*

Sample 6 was grown in the same manner as Sample 2, except for the underlying GaN was grown in the reactor and annealed in air at 566 °C.

The measure mobility was 61.89 m^2/Vs and the optical absorption edge was 1.17 eV. The XRD peaks seen in Fig. 5.22 correspond to the (002) on InN at 31.53° and the (002) of GaN at 33.33°. The measures thickness from Fig. 5.24 is 629 nm with 410 nm being the InN layer and 219 nm for the GaN layer.

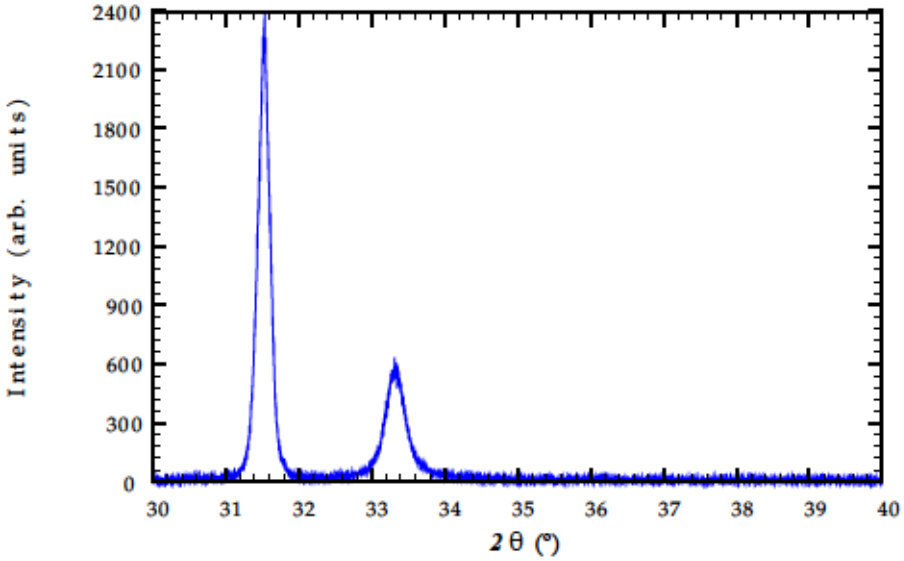

Figure 5.22: XRD of Sample 6.

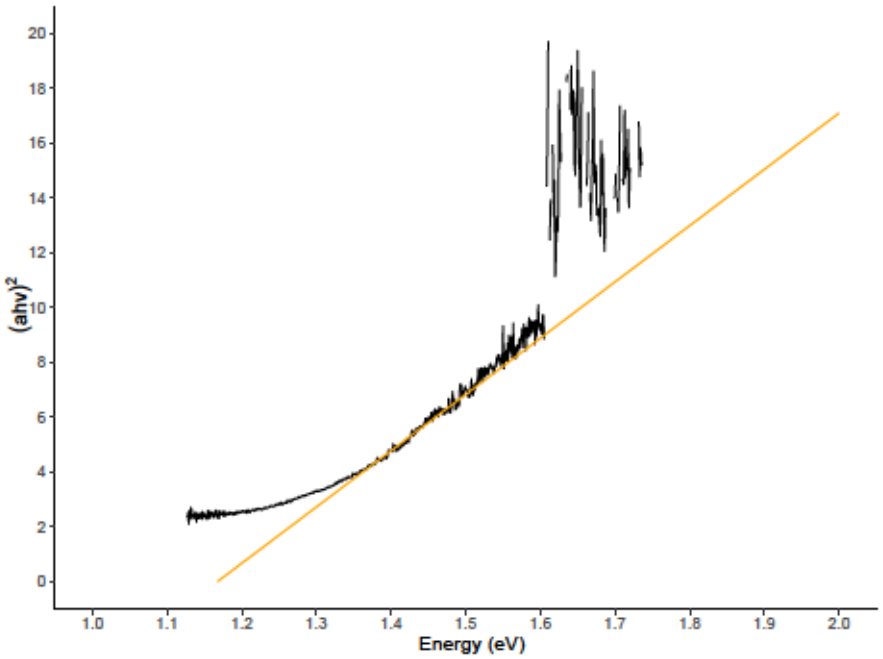

Figure 5.23: Tauc plot for Sample 6.

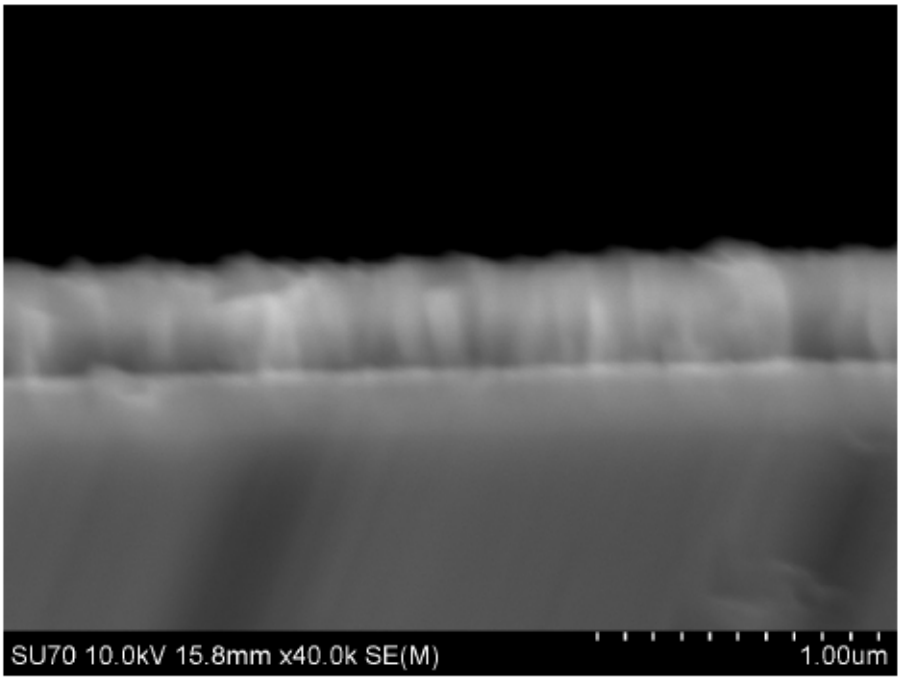

Figure 5.24: SEM of Sample 6.

5.2.1.7 *Sample 7*

Sample 7 was InGaN deposited on AlGaN. The III/V ratio for the InGaN was 0.03 : 2 and 2 : 3.5 for the AlGaN. The growth temperature was 540 °C. The measured mobility was 0.7 m^2/Vs and the optical absorption edge (Fig. 5.26) was 3.89 eV. The peaks seen in Fig. 5.25 at 33.76° and 34.91° are for the InGaN and AlGaN respectively. Each layer is hard to determine from Fig. 5.27 so the total thickness was instead measured at 266 nm

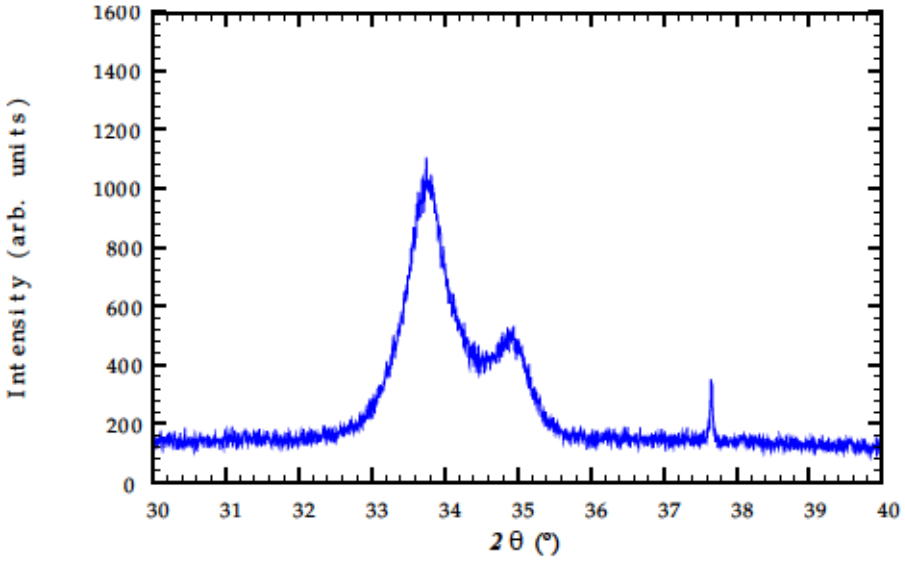

Figure 5.25: XRD of Sample 7.

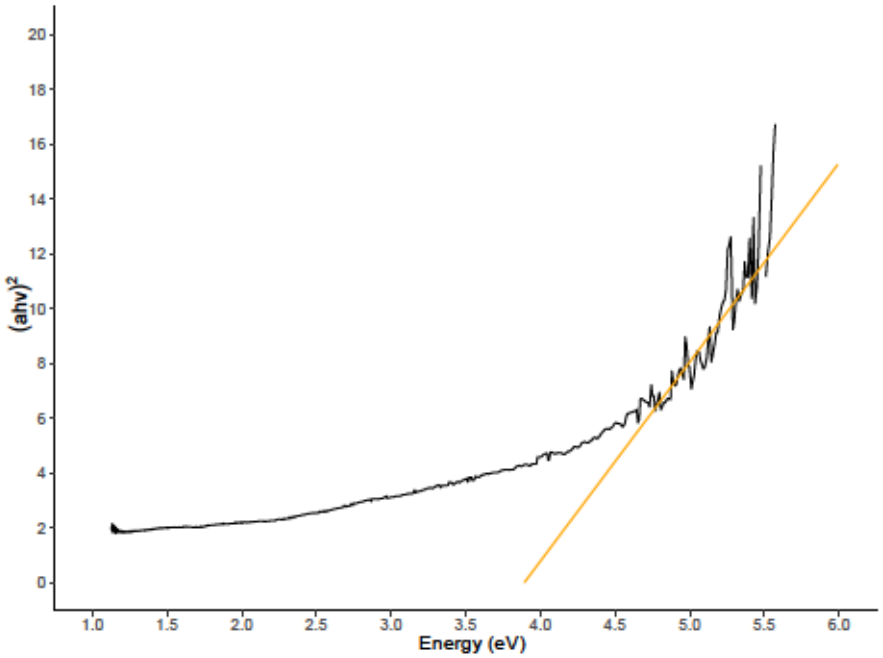

Figure 5.26: Tauc plot for Sample 7.

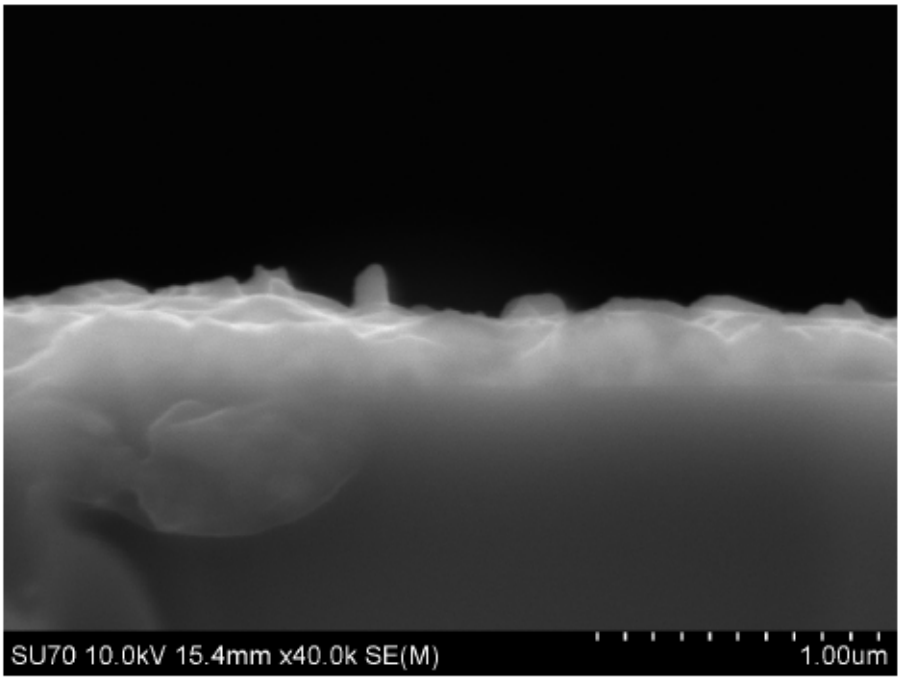

Figure 5.27: SEM of Sample 7.

5.2.1.8 *Sample 8*

Sample 8 was InGaN on Sapphire. The III/V ratio was 1 : 2 for both the GaN and InN loops. Much like Sample 2 a monolayer of GaN was deposited before a monolayer of InN, with the theoretical percentage of Indium being 50%. The measured mobility was 17.45 m^2/Vs with an optical absorption edge of 1.62 eV. The peak seen in Fig. 5.28 at 32.13 degree is the (002) of InGaN. An SEM was not taken.

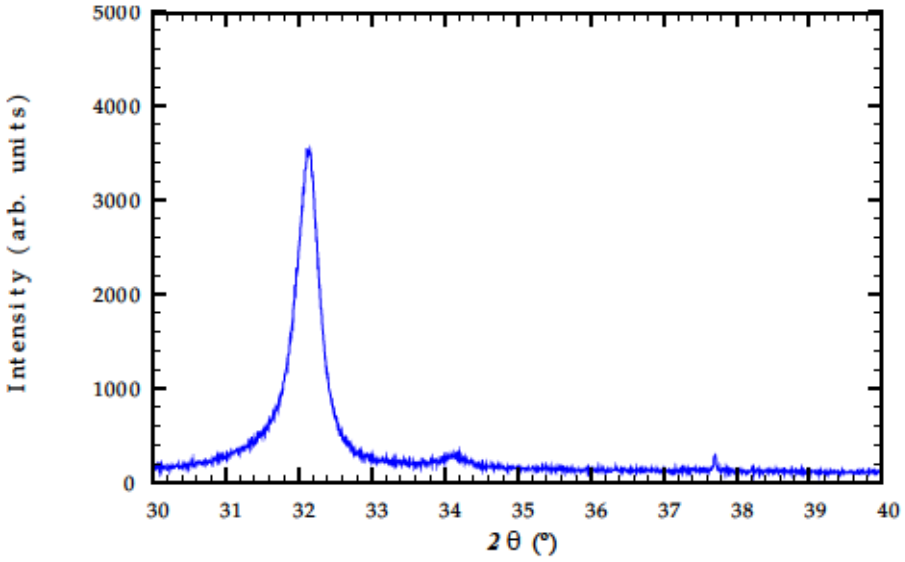

Figure 5.28: XRD of Sample 8.

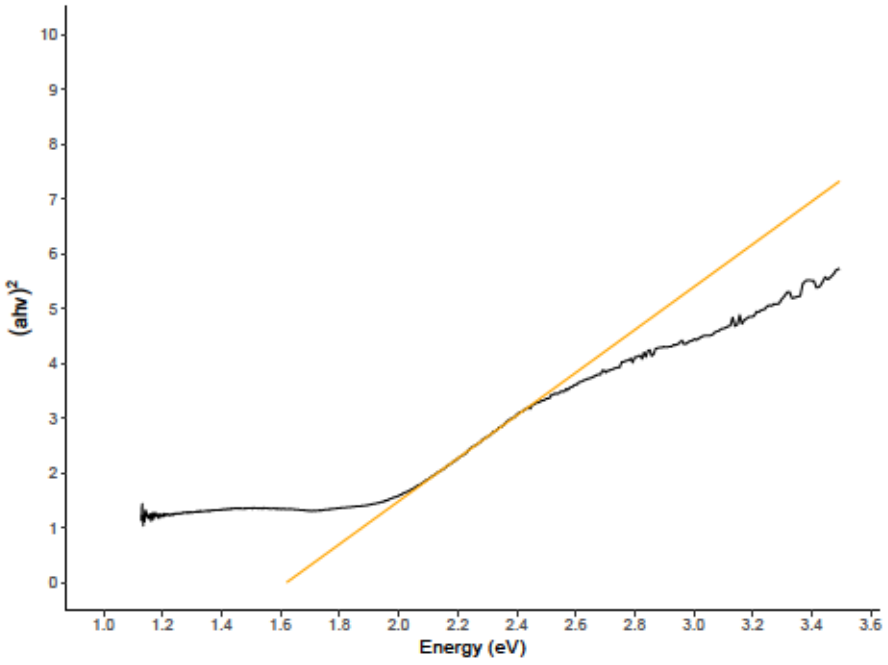

Figure 5.29: Tauc plot for Sample 8.

5.2.1.9 *Sample 9*

Sample 9 was grown though a custom-built dip coating process. Dip coating itself is a very simple process where a sample is dipped into a solution and withdrawn at at constant rate. This process can be divided into three distinct steps:

1. The initial immersion into the solution and a dwell time. This dwell time is to ensure a full wetting of the sample surface and to ensure the sample and solution are the same temperature.

2. The sample is withdrawn at a constant speed. This withdraw rate determines the thickness of the layer though the hydrodynamics of the solution. This included the solution evaporation, drainage of the solution off the sample and capillary pressure.

3. The final evaporation. Any remain solvent and undesirable organic compounds fully evaporate leaving behind the metal oxide gel network on the substrate surface. This is typically done at high temperatures to ensure complete evaporation between dips, however if the temperature is too high the rapid evaporation of the by-products will disturb the layer

Sample 9 was prepared on float glass with a Zinc acetate dyhidrate solution in Butanol, with a 0.5% Aluminum Chloride addition at a 2.5 cm min^{-1} withdraw rate and a 200 °C evaporation in an open air furnace, with a final anneal in a 500 °C closed oven for one hour. The sample was then treated to a one hour RF nitradation to improve conductivity. XRD scan of the sample show just the (002) and the (004) peaks at 34.86° and 72.95° respectively. The mobility as measured by the Van der Pauw method is 18.94 m^2/Vs. The optical absorption edge is 3.23 eV and the Tauc plot can be seen in Fig. 5.31 and the thickness of the layer was 746 nm which can be seen in Fig. 5.32

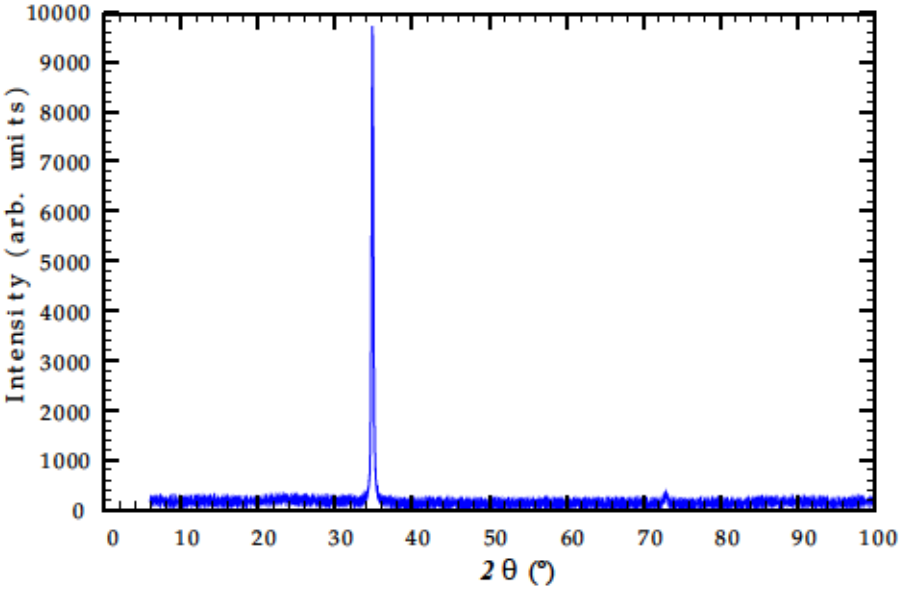

Figure 5.30: XRD of Sample 9.

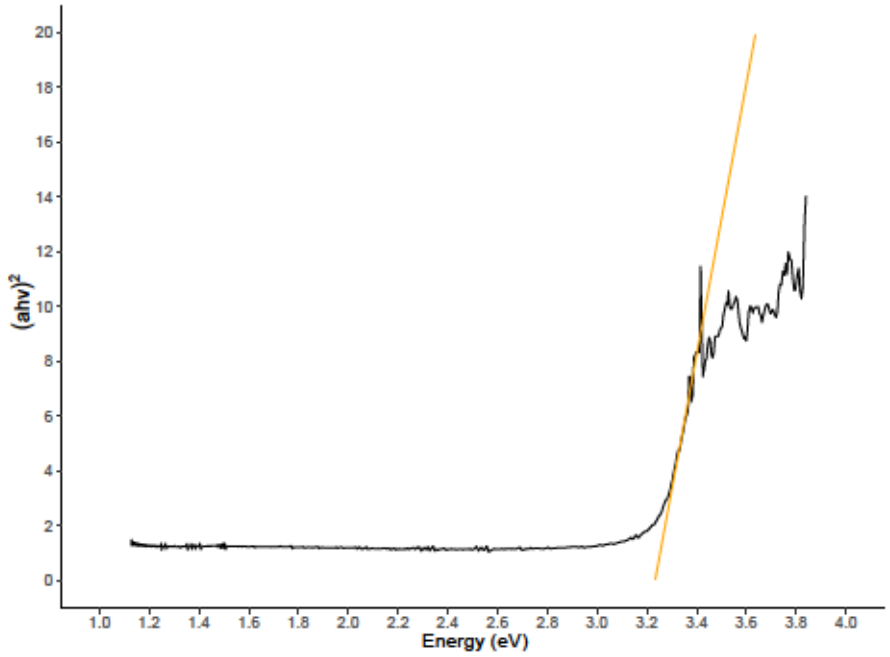

Figure 5.31: UV-Vis Tauc plot for Sample 9

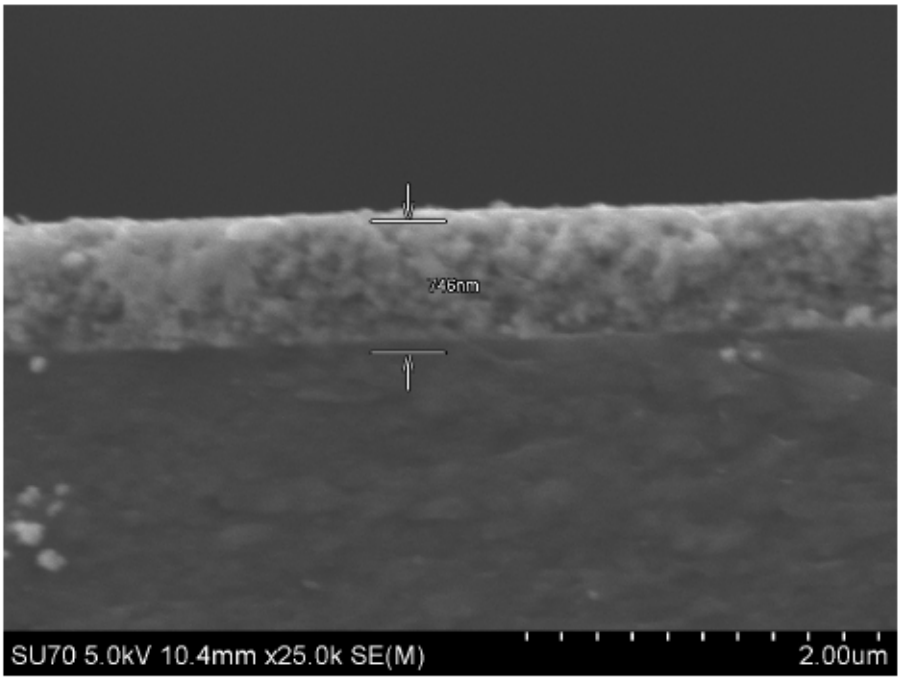

Figure 5.32: SEM image of Sample 9

5.2.1.10 *Summary*

Table 5.1 shows a summary of the samples along with the optical absorption edge, mobility, and sample thickness. These three pieces of data are the most important for a PEC cell, as the absorption edge determines what wavelengths of light can be effectively absorbed. The mobility determines the transfer of electrons or holes though the material and into solution. Finally, the sample thickness determines how much of the incoming light can be adsorbed. The band gaps of Samples 2, 4 and 6 differ from the standard value due to defects within the layer, either though incorporation of Oxygen atoms, or structural defects.

Table 5.1: Summary of all samples

Sample	Material	Mobility (m^2/Vs)	Optical Edge (eV)	Sample Thickness (nm)
1	GaN	5.26	3.23	324
2	InN	72.1	1.11	2539
3	InGaN	40.7	1.86	826
4	InN	36.5	0.78	486
5	GaN	106.8	3.5	494
6	InN	61.89	1.17	629
7	InGaN-AlGaN	0.71	3.89	266
8	InGaN	1.75	1.62	
9	ZnO	1.89	3.23	746

From the measured optical absorption edge samples 3 and 8 have the ideal optical absorption edge (from 1.6 eV to 2.2 eV) while samples 1, 5, 7, and 9 are larger than the ideal but wide enough to allow for both the HER and OER. Samples 2 and 6 should only work for the OER based on their absorption edge, however since sample 2 was grown on commercially purchased GaN, there could be a possibility for H_2 gas to be generated if there is tunnelling though the InN layer. The mobility of the samples determines the charge transfer in the semiconductor-liquid interface, thus the higher the mobility the more electrons (or holes depending on the potential) should be an indicator as to to which sample would be best. Finally, the thickness should be on the order of the optical penetration depth for maximum light absorption. From these requirements, Sample 3 should be the best for both HER and OER, with sample 1 and 5 following.

5.2.2 *Photoelelectrochemical Analysis*

5.2.2.1 *Sample Preparation*

Sample preparation for all samples are the same regardless of composition. Each sample was sectioned and a piece was chosen. A drop of In/Sn solder was placed on the layer with a thin silver wire attached. The wire then had a molex pin crimped onto the end and the solder joint was coated in JB Weld Marine epoxy before being covered by heat shrink. The surface area of each sample was measured using a photograph of the sample against a ruler and the ImageJ software is used used to measure the surface area, an example of which can be seen in Fig. 5.33.

The final measured surface area for each sample is summarized in Table 5.2.

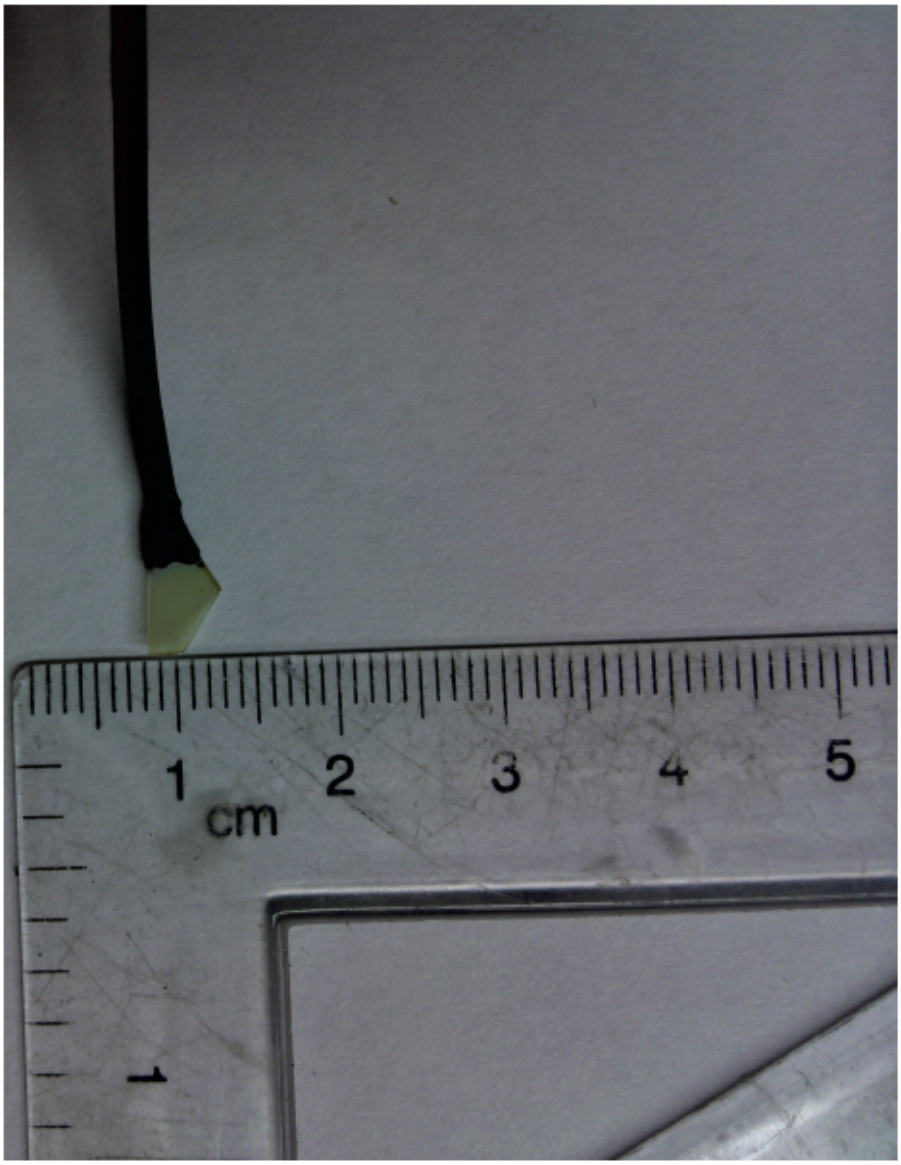

Figure 5.33: An example of the sample preparation along with the ruler used for surface area calculations

Table 5.2: Surface area for all samples

Sample	Surface Area (cm^2)
1	0.189
2	0.151
3	0.709
4	0.264
5	0.268
6	0.417
7	0.221
8	0.573
9	0.409
10	0.449

Sample preparation at TU Sofia consisted of cleaning the samples in Acetone and ethanol before a rinse in DI water. The sample was then mounted to a piece of copper with a gold wire stuck to the copper with double sided tape. The gold wire was then placed over the layer of the sample before a silicone pad with a hole punched through was placed on top with the hole surrounded by the gold wire. Then a piece of acrylic with a matching hole was placed on top of the silicone and a gasket was used to seal the stack to the bottom of the cell.

5.2.2.2 *Voltammograms*

Voltammograms completed at Lakehead University were performed with a scan rate of $500\,mV\,s^{-1}$ which is an extremely fast scan rate. As such, some data would have been lost but the overall effect would still be present. Voltammograms completed at TU Sofia were performed at a scan rate of $50\,mV\,s^{-1}$ or $10\,mV\,s^{-1}$ in order to better see any effects from the electrochemical process. Each sample was tested in a alkaline ($NaOH$), neutral ($NaCl$ with and without Na_2SO_3) and acidic (H_2SO_4) conditions. A linear sweep voltammogram was preformed from $-5\,V$ to $+5\,V$ ($-2\,V$ to $2\,V$ at TU Sofia). Fig. 5.34 shows the results

for Sample 1, 3, and 4. For Sample 1, where the layer is GaN it seems that an alkaline solution would be the best, because the overpotential of the hydrogen and oxygen evolution reaction are the smallest (the sharp increase in current density in the cathodic and anodic direction occurs at the most positive and negative potentials respectively). While for Sample 3 and 4, InGaN and InN respectively, acidic conditions seem to provide the best results.

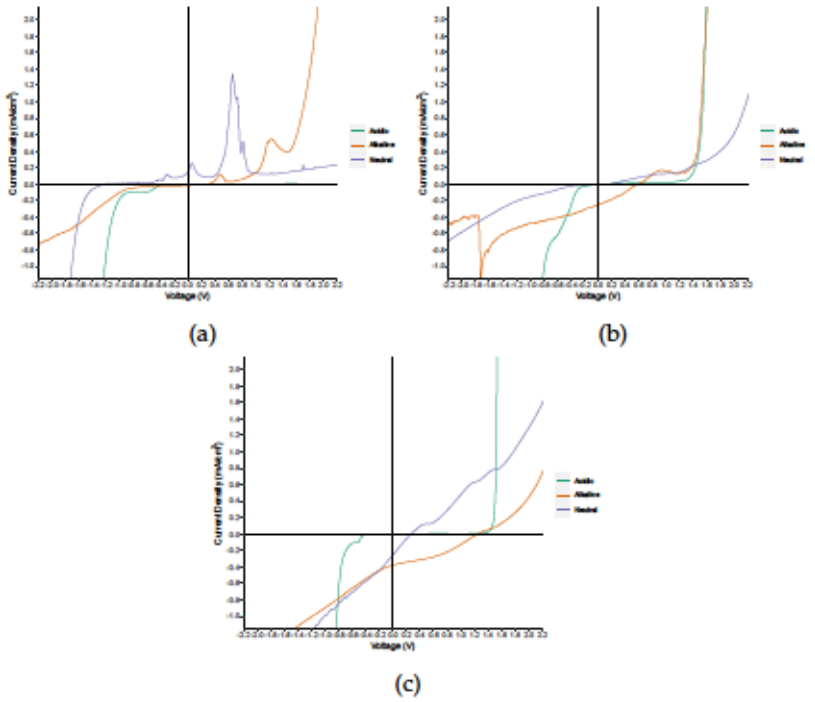

(a) (b) (c)

Figure 5.34: pH comparison for (a) Sample 1: GaN, (b) Sample 3: InGaN, and (c) Sample 4: InN

The weak current (not exceeding 0.1 mA/cm2) recorded at low cathodic polarizations is a result of dissolved oxygen in the electrolyte. It rapidly depletes (to potentials of about -0.5 V) and the horizontal line indicates diffusion limited oxygen reaction. At additional cathodic polarization, a sharp rise in the cathodic current is observed due to the hydrogen evolution reaction.

During anodic (positive voltages) conditions, three stages were seen to occur in all samples in the neutral solution and GaN samples in the alkaline solution. As seen in Fig. 5.35, which shows the linear sweep

of Sample 3 in anodic conditions, on the second test the current was reduced as the morphology of the layer changed during the first test.

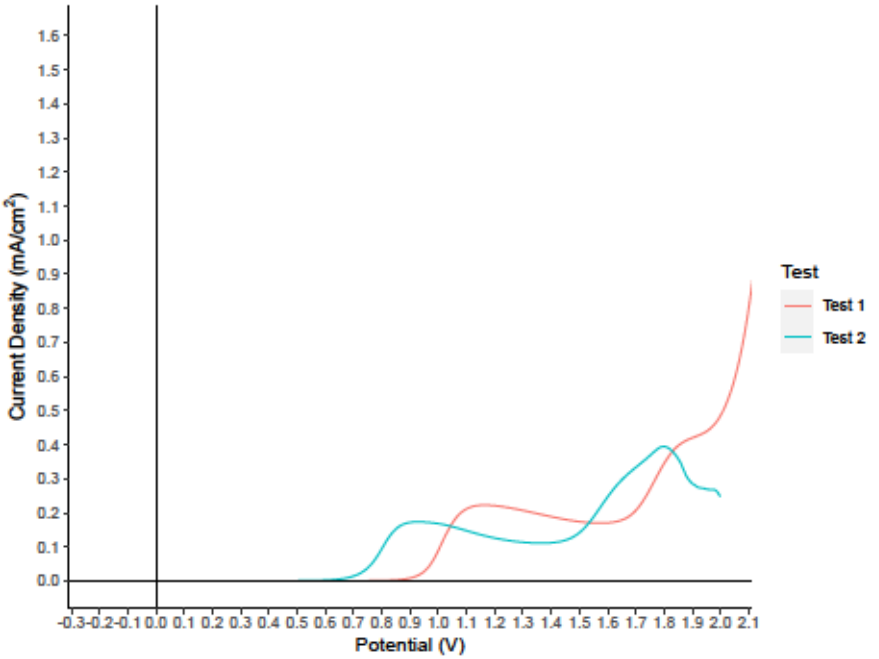

Figure 5.35: Linear sweep voltammogram of Sample 3 (InGaN) under anodic conditions.

Each of the seen stages, depicted in Fig. 5.36 corresponds to a different phenomenon.

1. Electrochemical: High anodic polarization induces additional oxidation of the nitride layer, which affects the dependence with increasing current density at potentials around 0.8 V.

2. Chemical: The negative ions in solution during anodic conditions while the layer is positively charged causes oxygen inclusion into the surface (passivation) causing a depletion of electroactive ions from the surface of the layer resulting in difficulty generating electrons and the current decreases.

3. Electrochemical: $2H_2O + 4e^- \rightarrow O_2 + 4H^+$ After the layer change and the voltage gets high enough to penetrate through the passivated layer the reaction continues.

Alternatively, for stage two, the layer is being dissolved into solution causing a current decrease. In this case stage 3 would not be present. The onset for stage two begins at the point where the current stabilizes and begins to drop as the passivated layer blocks current flow into the layer.

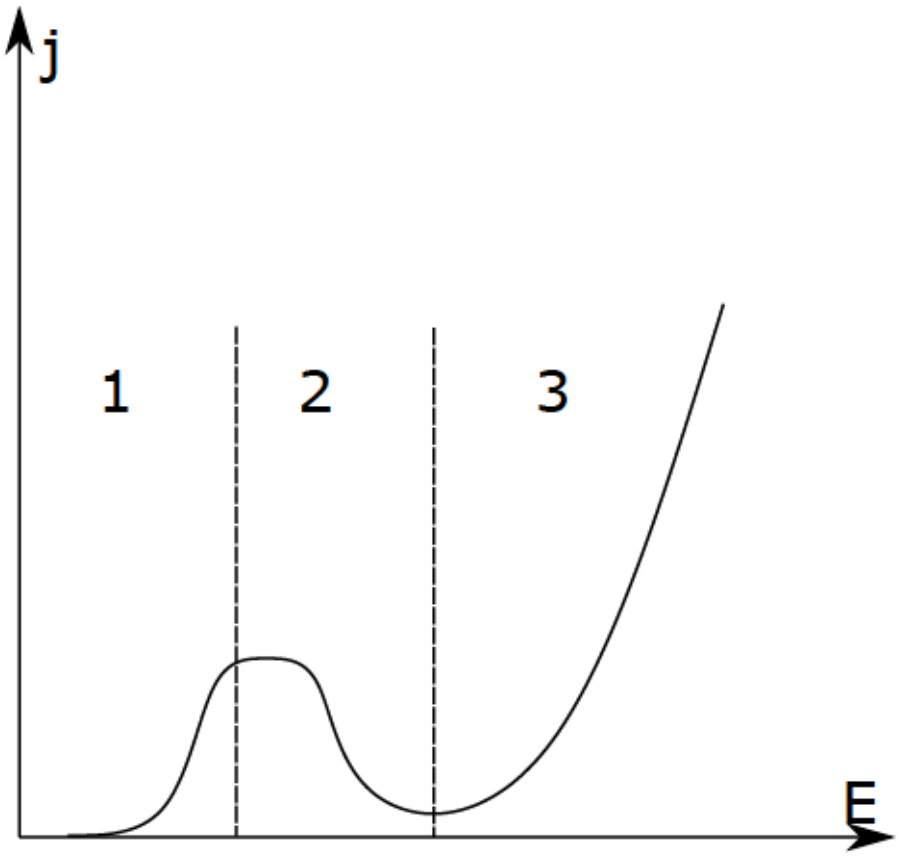

Figure 5.36: A typical curve seen in anodic conditions with the three regions being identified.

The samples were also compared by pH to verify if the InGaN samples provided the best response (lowest HER and OER). The only dateset that provided useful data was the acidic comparison, as contamination within the solution for the neutral and alkaline test provided no consistent results. Fig. 5.37 shows the voltammogram acidic test for each sample. Sample 3 (InGaN) proved to be the best sample for both HER and OER, followed by samples 4 (InN), 6 (InN), and 8 (InGaN) all having a similar HER.

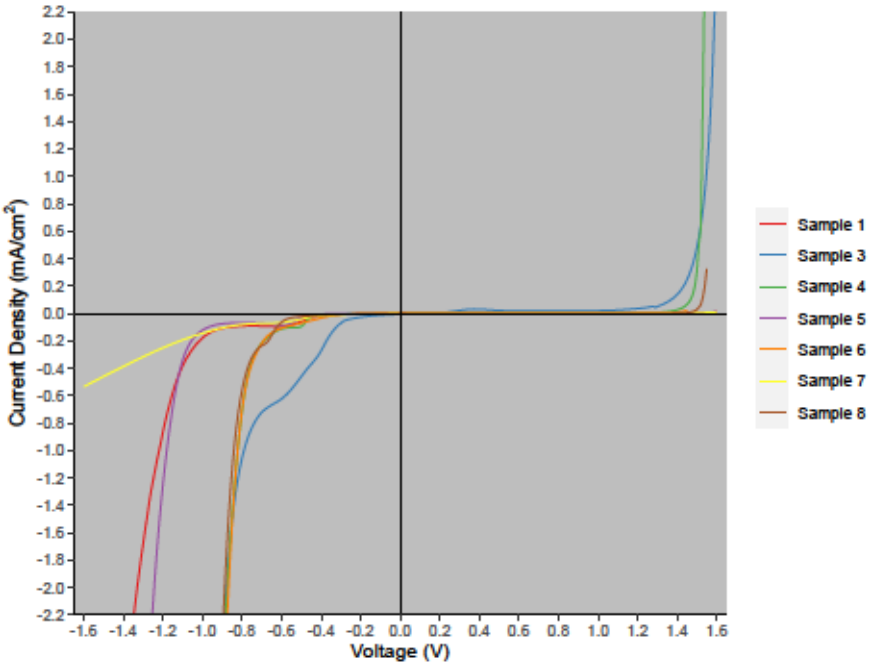

Figure 5.37: Comparison between each sample in an acidic solution.

5.2.3 *Photoresponse*

Two tests were used to determine a photoresponse. Both tests used the 500 W light source. The first, was the same as the previous tests, the linear sweep voltammogram. This was used to determine if any of the samples would change with illumination. Fig. 5.38 shows the linear sweep for Sample 2 (InN). For the anodic side there is no difference with illumination while with the cathodic side the onset of the HER occurs at a much higher voltage.

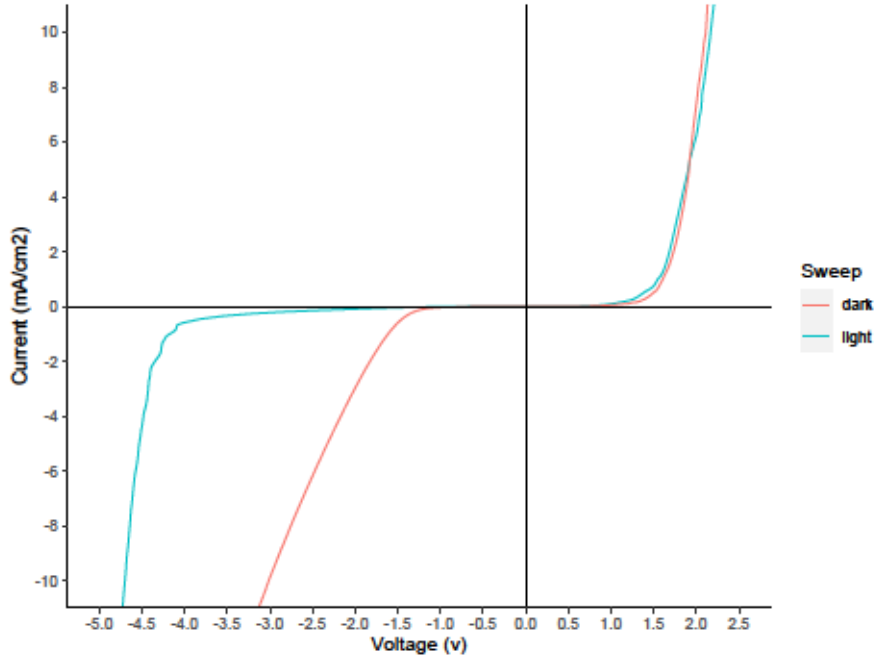

Figure 5.38: Linear sweep voltammogram for Sample 2 (InN) with both the dark scan and the illuminated scan.

For anodic conditions, a similar trend is seen in Sample 3 (InGaN Fig. 5.39). There seems to be no effect with illumination for the production of oxygen.For cathodic conditions, with illumination, the onset of hydrogen production occurs earlier. The cathodic peak seen at around 0 V is the result of impurities in the solution that are not part of the experiment.

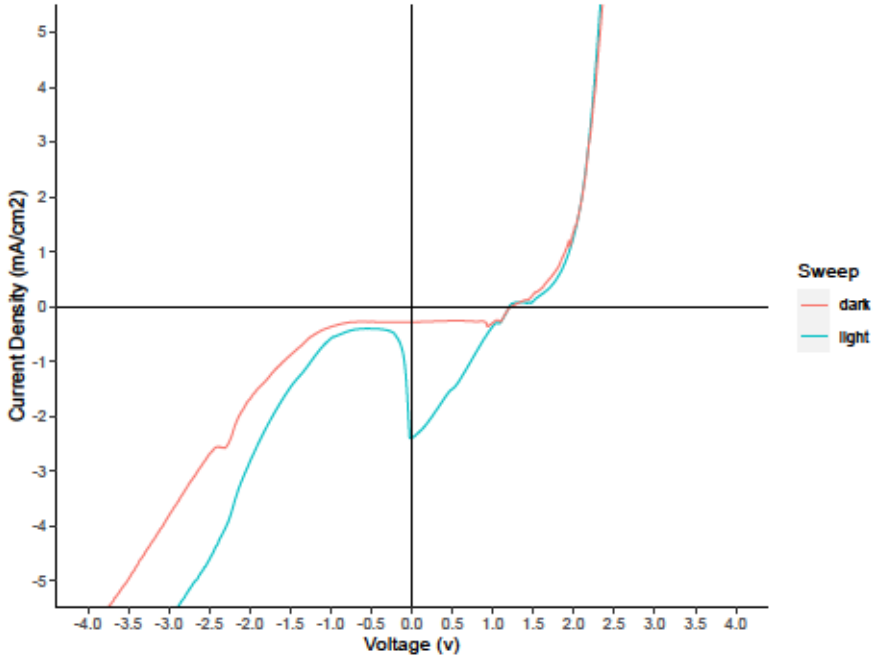

Figure 5.39: Linear sweep voltammogram for Sample 3 (InGaN) with both the dark scan and the illuminated scan.

The second test was a chopped open circuit test. 0 V was applied and the current was measured while the light source was pulsed every 5 s. Only Samples 2, 5, and 7 showed any photoresponse, while Sample 8 started out with a photoresponse, but after a certain number of cycles the signal became noisy. Fig. 5.40 shows the chopped photoresponse for Sample 2.

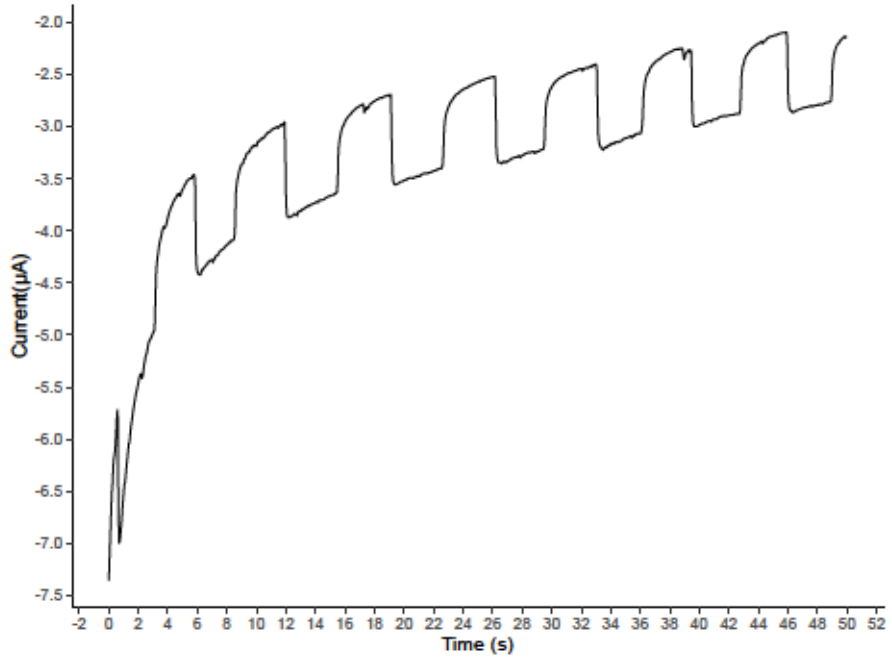

Figure 5.40: Chopped photoresponse for Sample 2 (InN).

From the chopped photoresponse it is possible to estimate the amount of hydrogen released using illumination using Faraday's law of electrolysis (Eq. (5.1)).

$$\text{Mole of } H_2 = \frac{1}{2}\frac{(\int_0^t I d\tau)}{F} \tag{5.1}$$

Where F is the Faraday constant (the quantity of charge in coulombs carried by one mole of electrons). By calculating the area under the curve from the chopped photoresponse, $\int_0^t I d\tau$ can be found. For Sample 2:

$$\text{Mole of } H_2 = \frac{1}{2}\frac{(\int_0^t I d\tau)}{F} \tag{5.2}$$

$$= 7.93 \times 10^{-11}\,\text{mol} \times 22.4\,\text{L mol}^{-1} \tag{5.3}$$

$$= 2.0166 \times 10^{-2}\,\frac{\mu\text{L}}{\text{min cm}^2} \tag{5.4}$$

5.2.4 *Sample Degradation*

After the voltammograms the surfaces of the samples went though a morphological change caused by either the electrochemical process or though a photoelectrochemical process. The samples were scanned with the AFM before and after testing to determine the amount of degradation experienced. In addition samples scanned repeatably achieved a lower current density for each subsequent scan. Fig. 5.41 shows the AFM scan for sample 4. For completeness the other samples will be included in Appendix B. Table 5.3 shows the RMS roughness before and after PEC testing.

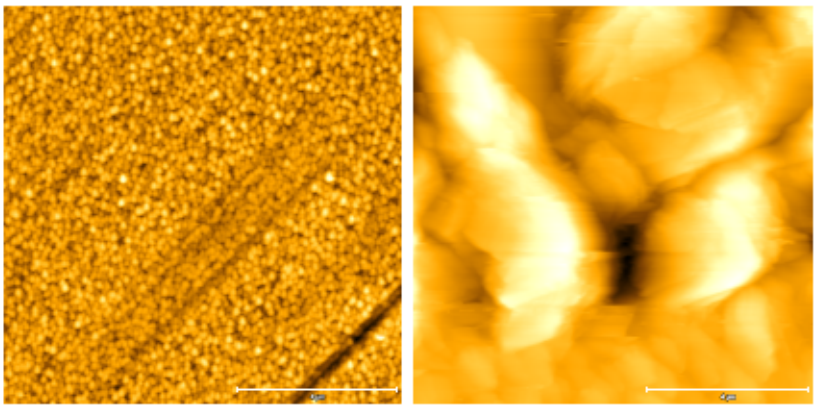

(a) (b)

Figure 5.41: (a) AFM scan before testing. (b) AFM scan after testing.

Table 5.3: RMS roughness before and after PEC testing.

Sample	Make-up	Initial R_q(nm)	Final R_q(nm)
1	GaN	3.507	12.80
2	InN on Commercial GaN	9.912	58.95
3	InGaN	21.95	44.58
4	InN on GaN	13.02	152.4
5	GaN	1.234	2.773
6	InN on GaN	27.96	59.70
7	InGaN on AlGaN	19.94	155.7
8	InGaN	2.196	35.50
9	ZnO	3.056	7.888

All samples saw an increase in surface roughness caused by one of two cases: anodic conversion of the layer or mechanical destruction caused by the release of the gasses. From the above results it would seem that GaN and ZnO are the most stable as photoelectrodes. However both GaN and ZnO only absorb in the UV range of light. Further experiments would be required to increase the stability of InGaN as a layer for photoelectrodes as InGaN can be band engineered to absorb in the visible spectrum of light.

6

CONCLUSIONS

Investigations into the band gap of InN was performed. The XRD results show that the InN layers are polycrystalline Wurtzite-type.The measured band gap was found to be 1.80 ± 0.25 eV using XAS and XES and confirmed with XEOL. Chemical analysis from the O K-edge XAS spectra showed the presence on oxygen impurities in the InN layers with the oxygen being more on the surface than in the bulk. This is also confirmed though XPS measurements with the $O1s$ scan showing an $In-O$ bond along with adsorbed oxygen, with the adsorbed oxygen having a higher peak than the $In-O$ bond. Additionally the XEOL measurements also confirm oxygen impurities in the samples.

Layers grown at the Lakehead Semiconductor Research Lab prototype reactor have been used to demonstrate photoelectrodes for use in PEC cells. The layers experienced degeneration due to mechanical destruction though the evolution of gases or though anodic changes to the layers. A possible solution to this would be to passivate the layers with a metal oxide to act as nucleation sites for gas evolution and to operate strictly in the cathodic region.

Samples under illumination showed no difference in anodic conditions to the samples tested with no illuminations. In cathodic conditions, the HER occurred at higher (more negative) voltages under illuminations for GaN, while for InGaN under illumination, HER occurred lower voltages as opposed to the dark sweep.

It was also found that GaN operates best in alkaline solutions, whereas indium containing layers operated best within acidic conditions, when comparing the onset of HER and OER.

Work is still needed to increase the stability of the layers for use as photoelectrodes. P-type doping the III-V Nitrides could provide an avenue for photoanodes, as current n-type and unintentionally doped layers can only act as photocathodes. As well with p-type doping, the sample surface exhibits electron accumulation under illumination, so a p-type semiconductor material as a working electrode offers self-protection against photocorrosion caused by semiconductor oxidization. Testing should also be done to determine photoresponse at the HER for photocathodes in order to determine gas evolution. Two-electrode measurements will also need to be performed for final stability testing and for measuring STH conversion rates.

Finally, investigations into alternate substrates for III-V nitrides should be completed. The tunability of InGaN should allow for lattice matching to a variety of substrates. This tunability could be used to grow InGaN on silicon based photo-voltaics to provide the backing power needed to drive the PEC device.

Part I

APPENDIX

A

APPENDIX A

A.1 LINEAR SWEEP VOLTAMMETRY

Below is the code for the liner sweep voltammetry:

```
#Import the required packages and modules from pymeasure
import logging
import sys
from time import sleep
import numpy as np

from pymeasure.instruments.keithley import Keithley2400
from pymeasure.display.Qt import QtGui
from pymeasure.display.windows import ManagedWindow
from pymeasure.experiment import (
    Procedure, FloatParameter, unique_filename, Results,
    Parameter
)
#Start the logger
log = logging.getLogger('')
log.addHandler(logging.NullHandler())

#The sweep procedure
class VIProcedure(Procedure):

    #Declare all the required input parameters:max
    voltage, min voltage, voltage step, delay between
    each step
```

```
#maximum current range, and the sample name for
saving the file
max_voltage = FloatParameter('Maximum Voltage',
units='V', default=5)
min_voltage = FloatParameter('Minimum Voltage',
units='V', default=-5)
voltage_step = FloatParameter('Voltage Step', units=
'V', default=0.01)
delay = FloatParameter('Delay Time', units='ms',
default=20)
current_range = FloatParameter('Current Range',
units='A', default=1)
sample = Parameter('Sample Name', default='Sample')
DATA_COLUMNS = ['Voltage (V)', 'Current (A)']

def startup(self):
    log.info("Setting up instruments")

   #Inital set-up for the 2400, with the RS232
connection and what mode to be used
    self.source = Keithley2400("ASRL4", timeout
=1200, baud_rate=57600)
    self.source.apply_voltage()
    self.source.measure_current()
    self.source.wires=4
    self.source.source_voltage_range = self.
min_voltage
    self.source.compliance_current = self.
current_range
    self.source.enable_source()
    sleep(2)
#To sweep though the voltage an array is used to
tell the 2400 which voltage to be set at for both
sweeping from
```

```
        #min to max and from max to min and then making a
        master array for the program to use.
        def execute(self):
            voltage_up = np.arange(self.min_voltage, self.
        max_voltage, self.voltage_step)
            voltage_down = np.arange(self.max_voltage, self.
        min_voltage, -self.voltage_step)
            voltages = np.concatenate((voltage_up,
        voltage_down))  # Include the reverse

            steps = len(voltages)
            #sweep the voltage and measure the current
            log.info("Starting to sweep through voltage")
            for i, voltage in enumerate(voltages):
                log.debug("Measuring voltage: %g V" %
        voltage)

                self.source.source_voltage = voltage
                # Or use self.source.ramp_to_current(current
        , delay=0.1)
                sleep(self.delay * 1e-3)

                current = self.source.current



                data = {
                    'Current (A)': current,
                    'Voltage (V)': voltage,
                }
                self.emit('results', data)
                self.emit('progress', 100. * i / steps)
                if self.should_stop():
                    log.warning("Catch stop command in
        procedure")
```

```
                break

    def shutdown(self):
        self.source.shutdown()
        log.info("Finished")

#The GUI procedure, creates a windowed box with
    changeable inputs for the variables listed in the
    sweep procedure
#and graphs the output
class MainWindow(ManagedWindow):

    def __init__(self):
        super().__init__(
            procedure_class=VIProcedure,
            inputs=[
                'max_voltage', 'min_voltage', '
    voltage_step',
                'delay', 'current_range', 'sample'
            ],
            displays=[
                'max_voltage', 'min_voltage', '
    voltage_step',
                'delay', 'current_range','sample'
            ],
            x_axis='Voltage (V)',
            y_axis='Current (A)',

        )
        self.setWindowTitle('IV Measurement')

    def queue(self):
        directory = "./"  # Change this to the desired
    directory
```

```
        procedure = self.make_procedure()
        filename = unique_filename(directory, prefix='
    Sweep '+procedure.sample + '_')
        results = Results(procedure, filename)
        experiment = self.new_experiment(results)

        self.manager.queue(experiment)

#the main program, which calls the above procedure and
    creates the GUI though pymeasure
if __name__ == "__main__":
    app = QtGui.QApplication(sys.argv)
    window = MainWindow()
    window.show()
    sys.exit(app.exec_())
```

A.2 CHOPPED PHOTORESPONSE

Below is the code for the chopped photoresponse:

```
#Import the required packages and modules from pymeasure
import logging
import sys
from time import sleep
import numpy as np
from pymeasure.instruments.keithley import Keithley2400
from pymeasure.display.Qt import QtGui
from pymeasure.display.windows import ManagedWindow
from pymeasure.experiment import (
    Procedure, FloatParameter, unique_filename, Results,
    IntegerParameter, Parameter
)
```

```
log = logging.getLogger('')
log.addHandler(logging.NullHandler())

class Voltage_hold(Procedure):
    # Set the input parameters
    data_points = IntegerParameter('Data Points',
    default=1000)
    voltage = FloatParameter('Voltage', units='V',
    default=0)
    sample_rate = FloatParameter('Sample Rate', units= '
    ms', default=20)
    sample = Parameter('Sample Name', default='Sample')

    DATA_COLUMNS = ['Time (s)', 'Current (A)']



    def startup(self):
        log.info("Setting up instruments")

        #Inital set-up for the 2400, with the RS232
    connection and what mode to be used
        self.source = Keithley2400("ASRL4", timeout
    =1200, baud_rate=57600)
        self.source.apply_voltage()
        self.source.measure_current()
        self.source.wires=2
        self.source.source_voltage=self.voltage
        self.source.enable_source()
        self.source.compliance_current=0.5
        sleep(2) # wait here to give the instrument time
     to react
```

```
    def execute(self):
        time = np.zeros(self.data_points)
        rate=self.sample_rate

        voltage=self.voltage
        steps=len(time)

        #Holding the voltage at the specified value for
    the specified time
        log.info("Starting the voltage hold")
        for i, x in enumerate(time):


            self.source.source_voltage=voltage

            sleep(self.sample_rate*1e-3)

            t=i/(rate) #convert sample rate to time for
    the graph: samples/(sample rate * 1000)

            current = self.source.current



            data = {
                'Time (s)': t,
                'Current (A)': current,
            }
            self.emit('results', data)
            self.emit('progress', 100. * i / steps)
            if self.should_stop():
                log.warning("Catch stop command in
    procedure")
```

```
                break

    def shutdown(self):
        self.source.shutdown()
        log.info("Finished")


#The GUI procedure, creates a windowed box with
    changeable inputs for the variables listed in the
    sweep procedure
#and graphs the output
class MainWindow(ManagedWindow):

    def __init__(self):
        super().__init__(
            procedure_class=Voltage_hold,
            inputs=[
                'voltage', 'data_points', 'sample_rate',
    'sample'
            ],
            displays=[
                'voltage', 'data_points', 'sample_rate',
    'sample'

            ],
            x_axis='Time (s)',
            y_axis='Current (A)',

        )
        self.setWindowTitle('Voltage Hold')

    def queue(self):
        directory = "./"  # Change this to the desired
    directory
```

```
        procedure = self.make_procedure()

        filename = unique_filename(directory, prefix='
    Hold ' + procedure.sample + ' ')

        results = Results(procedure, filename)
        experiment = self.new_experiment(results)

        self.manager.queue(experiment)

#the main program, which calls the above procedure and
    creates the GUI though pymeasure
if __name__ == "__main__":
    app = QtGui.QApplication(sys.argv)
    window = MainWindow()
    window.show()
    sys.exit(app.exec_())
```

B

APPENDIX B

Below are the remaining AFM scans from Section 5.2.4 for completeness.

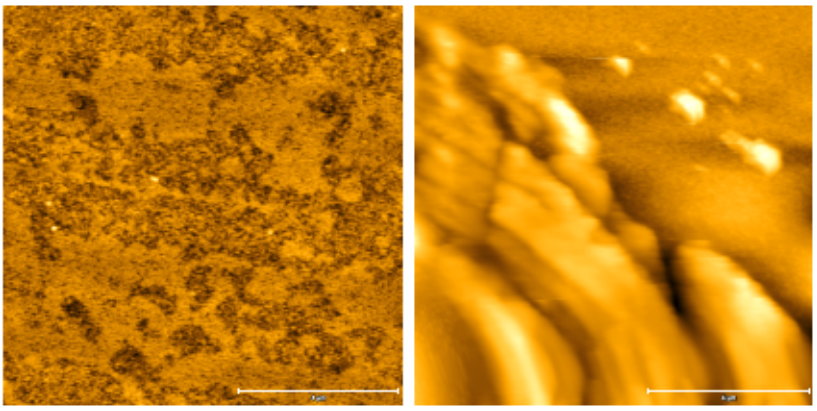

(a) (b)

Figure B.1: Sample 1 (a)Before (b)After.

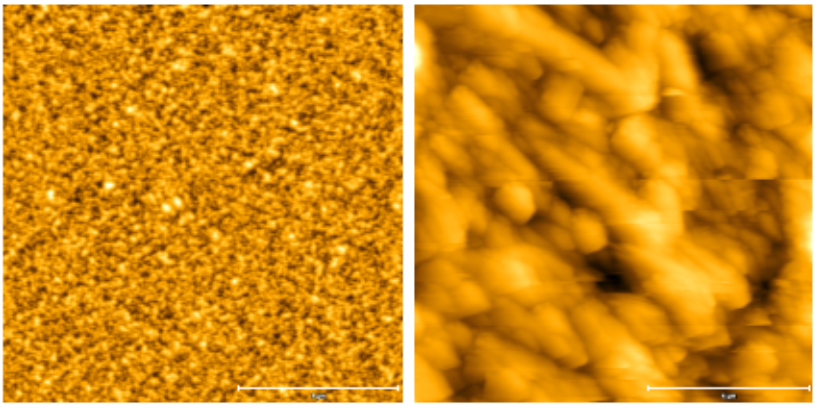

(a) (b)

Figure B.2: Sample 2 (a)Before (b)After.

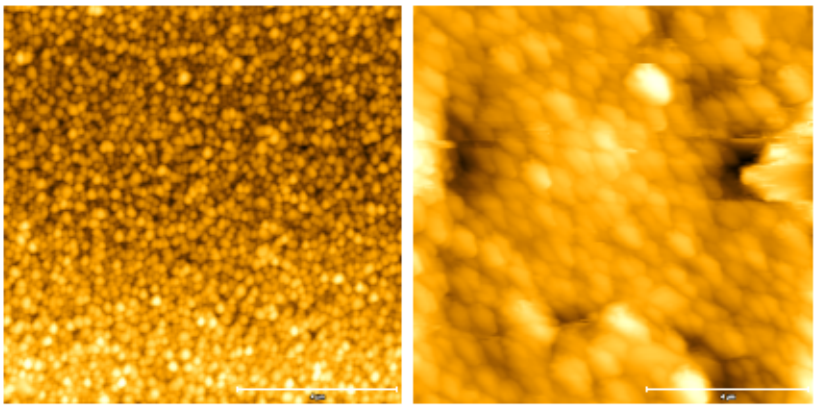

(a) (b)

Figure B.3: Sample 3 (a)Before (b)After.

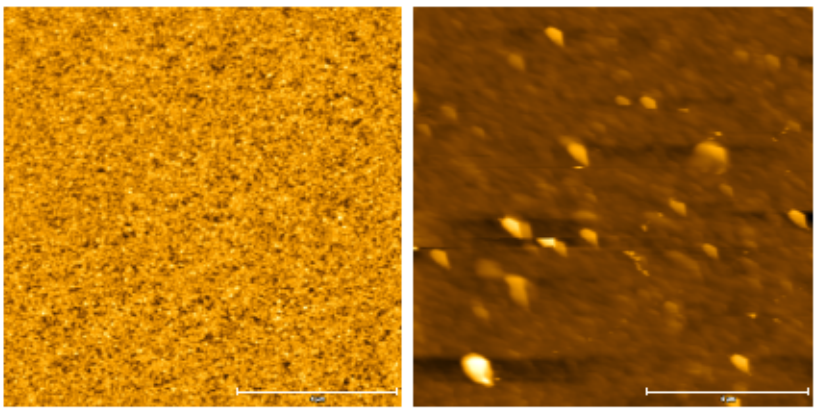

(a) (b)

Figure B.4: Sample 5 (a)Before (b)After.

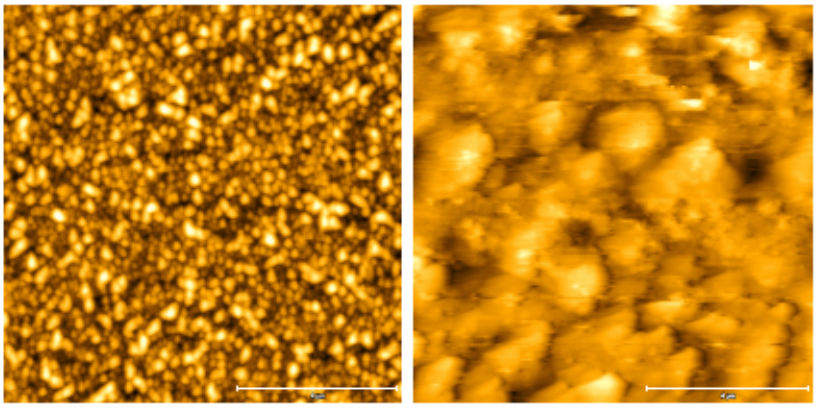

(a) (b)

Figure B.5: Sample 6 (a)Before (b)After.

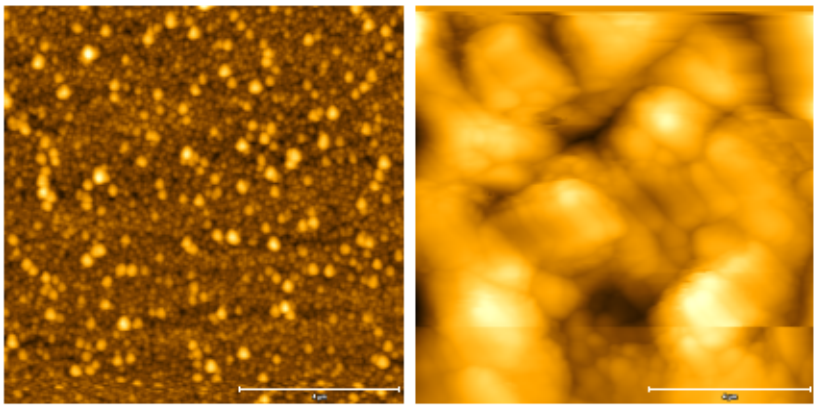

(a) (b)

Figure B.6: Sample 7 (a)Before (b)After.

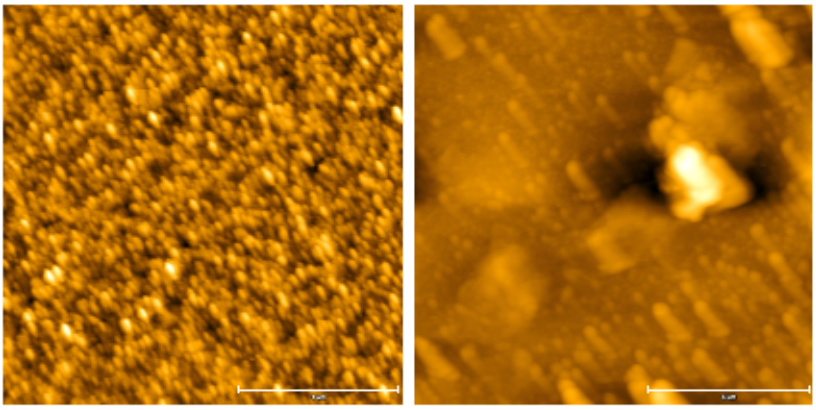

(a) (b)

Figure B.7: Sample 8 (a)Before (b)After.

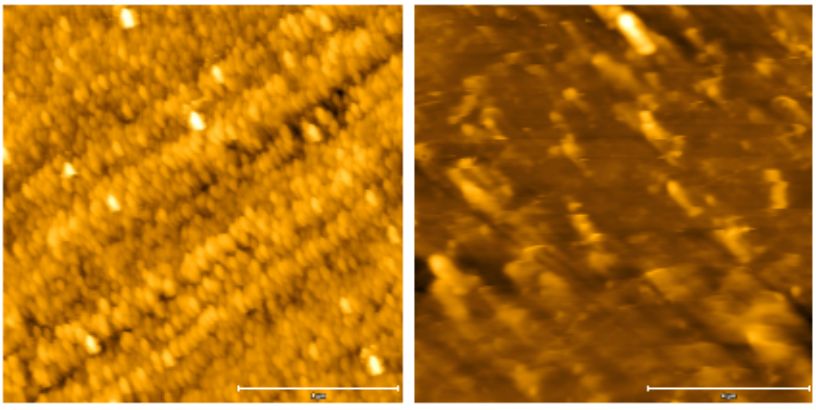

(a) (b)

Figure B.8: Sample 9 (a)Before (b)After.

BIBLIOGRAPHY

[1] H. Ritchie, M. Roser, and P. Rosado, "Energy," *Our World in Data*, Nov. 28, 2020. [Online]. Available: https://ourworldindata.org/fossil-fuels (visited on 05/17/2022).

[2] "Statistical Review of World Energy | Energy economics | Home," bp global. (2021), [Online]. Available: https://www.bp.com/en/global/corporate/energy-economics/statistical-review-of-world-energy.html.

[3] R. Leroy, "Industrial water electrolysis: Present and future," *International Journal of Hydrogen Energy*, vol. 8, no. 6, pp. 401–417, 1983, ISSN: 03603199. DOI: 10.1016/0360-3199(83)90162-3.

[4] R. Moradi and K. M. Groth, "Hydrogen storage and delivery: Review of the state of the art technologies and risk and reliability analysis," *International Journal of Hydrogen Energy*, vol. 44, no. 23, pp. 12 254–12 269, May 2019, ISSN: 03603199. DOI: 10.1016/j.ijhydene.2019.03.041.

[5] M. Levinshtein, S. Rumyantsev, and M. Shur, *Handbook Series on Semiconductor Parameters: Volume 1: Si, Ge, C (Diamond), GaAs, GaP, GaSb, InAs, InP, InSb*. WORLD SCIENTIFIC, Nov. 1996, vol. 1, ISBN: 978-981-02-2934-4. DOI: 10.1142/2046-vol1. [Online]. Available: https://www.worldscientific.com/worldscibooks/10.1142/2046-vol1 (visited on 11/23/2020).

[6] H. Morkoç, *Handbook of Nitride Semiconductors and Devices*. Weinheim: Wiley-VCH, 2008, 1 p., ISBN: 978-3-527-40797-2.

[7] P. Siddiqua, W. A. Hadi, M. S. Shur, and S. K. O'Leary, "A 2015 perspective on the nature of the steady-state and transient electron transport within the wurtzite phases of gallium nitride, aluminum nitride, indium nitride, and zinc oxide: A critical and retrospective review," *Journal of Materials Science: Materials in Electronics*, vol. 26, no. 7, pp. 4475–4512, Jul. 2015, ISSN: 1573-482X. DOI: 10.1007/s10854-015-3055-7.

[8] X. H. Wu, D. Kapolnek, E. J. Tarsa, B. Heying, S. Keller, B. P. Keller, U. K. Mishra, S. P. DenBaars, and J. S. Speck, "Nucleation Layer Evolution in Metal-organic Chemical Vapor Deposition Grown GaN," *Applied Physics Letters*, vol. 68, no. 10, pp. 1371–1373, Mar. 1996, ISSN: 0003-6951. DOI: 10.1063/1.116083.

[9] K. Hiramatsu, "Epitaxial lateral overgrowth techniques used in group III nitride epitaxy," *Journal of Physics: Condensed Matter*, vol. 13, no. 32, p. 6961, 2001, ISSN: 0953-8984. DOI: 10.1088/0953-8984/13/32/306. [Online]. Available: http://stacks.iop.org/0953-8984/13/i=32/a=306 (visited on 06/26/2018).

[10] H. Amano, N. Sawaki, I. Akasaki, and Y. Toyoda, "Metalorganic vapor phase epitaxial growth of a high quality GaN film using an AlN buffer layer," *Applied Physics Letters*, vol. 48, no. 5, pp. 353–355, Feb. 3, 1986, ISSN: 1077-3118. DOI: 10.1063/1.96549.

[11] T. Mukai, K. Takekawa, and S. Nakamura, "InGaN-Based Blue Light-Emitting Diodes Grown on Epitaxially Laterally Overgrown GaN Substrates," *Japanese Journal of Applied Physics*, vol. 37, pp. L839–L841, Part 2, No. 7B Jul. 15, 1998, ISSN: 00214922. DOI: 10.1143/JJAP.37.L839. [Online]. Available: https://iopscience.iop.org/article/10.1143/JJAP.37.L839 (visited on 11/24/2020).

[12] T. Sasaki and T. Matsuoka, "Analysis of two-step-growth conditions for GaN on an AlN buffer layer," *Journal of Applied Physics*, vol. 77, no. 1, pp. 192–200, Jan. 1995, ISSN: 1089-7550. DOI: 10.1063/1.359368.

[13] J. S. Yuan, G. H. Yu, C. M. Yang, and M. Y. Wang, "Deposition and Characterization of GaN Films on ITO Glass Substrates by PECVD," *Materials Science Forum*, vol. 610, pp. 446–449, 2009, ISSN: 1662-9752. DOI: 10.4028/www.scientific.net/MSF.610-613.446. [Online]. Available: http://www.scientific.net/MSF.610-613.446 (visited on 06/02/2015).

[14] A. G. Bhuiyan, K. Sugita, A. Hashimoto, and A. Yamamoto, "InGaN Solar Cells: Present State of the Art and Important Challenges," *IEEE Journal of Photovoltaics*, vol. 2, no. 3, pp. 276–293, Jul. 2012, ISSN: 2156-3381. DOI: 10.1109/JPHOTOV.2012.2193384.

[15] J. K. Sheu, P. H. Liao, T. C. Huang, K. J. Chiang, W. C. Lai, and M. L. Lee, "InGaN-based epitaxial films as photoelectrodes for hydrogen generation through water photoelectrolysis and CO2 reduction to formic acid," *Solar Energy Materials and Solar Cells*, vol. 166, pp. 86–90, Jul. 1, 2017, ISSN: 0927-0248. DOI: 10.1016/j.solmat.2017.03.014. [Online]. Available: https://www.sciencedirect.com/science/article/pii/S0927024817301290 (visited on 01/28/2022).

[16] T. Yao and S.-K. Hong, Eds., *Oxide and Nitride Semiconductors: Processing, Properties, and Applications* (Advances in Materials Research). Berlin Heidelberg: Springer-Verlag, 2009, ISBN: 978-3-540-88846-8. DOI: 10.1007/978-3-540-88847-5.

[17] I. Vurgaftman and J. R. Meyer, "Band parameters for nitrogen-containing semiconductors," *Journal of Applied Physics*, vol. 94, no. 6, pp. 3675–3696, Aug. 29, 2003, ISSN: 0021-8979. DOI: 10.1063/1.1600519. [Online]. Available: https://aip.scitation.org/doi/10.1063/1.1600519 (visited on 06/26/2018).

[18] F. Bernardini, V. Fiorentini, and D. Vanderbilt, "Spontaneous polarization and piezoelectric constants of III-V nitrides," *Physical Review B*, vol. 56, no. 16, R10024–R10027, Oct. 15, 1997. DOI: 10.1103/PhysRevB.56.R10024. [Online]. Available: http://link.aps.org/doi/10.1103/PhysRevB.56.R10024 (visited on 04/27/2015).

[19] V. Y. Davydov, A. A. Klochikhin, R. P. Seisyan, *et al.*, "Absorption and Emission of Hexagonal InN. Evidence of Narrow Fundamental Band Gap," *physica status solidi (b)*, vol. 229, no. 3, r1–r3, 2001, ISSN: 1521-3951. DOI: 10.1002/1521-3951(200202)229:3<R1::AID-PSSB99991>3.0.CO;2-0.

[20] T. Araki, Y. Saito, T. Yamaguchi, M. Kurouchi, Y. Nanishi, and H. Naoi, "Radio Frequency-Molecular Beam Epitaxial Growth of InN Epitaxial Films on (0001) Sapphire and Their Properties," *Journal of Vacuum Science & Technology B: Microelectronics and Nanometer Structures Processing, Measurement, and Phenomena*, vol. 22, no. 4, pp. 2139–2143, Jul. 2004, ISSN: 1071-1023. DOI: 10.1116/1.1771682.

[21] T. V. Shubina, S. V. Ivanov, V. N. Jmerik, *et al.*, "Mie resonances, infrared emission, and the band gap of InN," *Physical Review Letters*, vol. 92, no. 11, p. 117 407, Mar. 19, 2004, ISSN: 0031-9007. DOI: 10.1103/PhysRevLett.92.117407. pmid: 15089170.

[22] R. Dubreuil, M. R. Amin, J. Tot, M. Nagorski, B. Kadikoff, A. Moewes, and D. Alexandrov, "Structure and bandgap determination of InN grown by RP-MOCVD," *Journal of Materials Science: Materials in Electronics*, vol. 33, no. 22, pp. 17 668–17 677, Aug. 2022, ISSN: 1573-482X. DOI: 10.1007/s10854-022-08630-x.

[23] M. X. Tan, P. E. Laibinis, S. T. Nguyen, J. M. Kesselman, C. E. Stanton, and N. S. Lewis, "Principles and Applications of Semiconductor Photoelectrochemistry," in *Progress in Inorganic Chemistry*, K. D. Karlin, Ed., Hoboken, NJ, USA: John Wiley & Sons, Inc., Mar. 9, 2007, pp. 21–144, ISBN: 978-0-470-16642-0. DOI: 10.1002/9780470166420.ch2. [Online]. Available: https://onlinelibrary.wiley.com/doi/10.1002/9780470166420.ch2 (visited on 08/16/2022).

[24] D. M. Chapin, C. S. Fuller, and G. L. Pearson, "A New Silicon p-n Junction Photocell for Converting Solar Radiation into Electrical Power," *Journal of Applied Physics*, vol. 25, no. 5, pp. 676–677, May 1954, ISSN: 0021-8979. DOI: 10.1063/1.1721711.

[25] J. F. Geisz, R. M. France, K. L. Schulte, M. A. Steiner, A. G. Norman, H. L. Guthrey, M. R. Young, T. Song, and T. Moriarty, "Six-junction III–V solar cells with 47.1% conversion efficiency under 143 Suns concentration," *Nature Energy*, vol. 5, no. 4, pp. 326–335, Apr. 2020, ISSN: 2058-7546. DOI: 10.1038/s41560-020-0598-5. [Online]. Available: http://www.nature.com/articles/s41560-020-0598-5 (visited on 08/17/2022).

[26] "Best Research-Cell Efficiency Chart." (2022), [Online]. Available: https://www.nrel.gov/pv/cell-efficiency.html (visited on 08/17/2022).

[27] S. Giménez and J. Bisquert, Eds., *Photoelectrochemical Solar Fuel Production*. Cham: Springer International Publishing, 2016, ISBN: 978-3-319-29639-5. DOI: 10.1007/978-3-319-29641-8.

[28] Z. Chen, H. N. Dinh, and E. Miller, *Photoelectrochemical Water Splitting* (SpringerBriefs in Energy). New York, NY: Springer New York, 2013, ISBN: 978-1-4614-8297-0. DOI: 10.1007/978-1-4614-8298-7.

[29] X. Yang, A. Wolcott, G. Wang, A. Sobo, R. C. Fitzmorris, F. Qian, J. Z. Zhang, and Y. Li, "Nitrogen-Doped ZnO Nanowire Arrays for Photoelectrochemical Water Splitting," *Nano Letters*, vol. 9, no. 6, pp. 2331–2336, Jun. 10, 2009, ISSN: 1530-6984. DOI: 10.1021/nl900772q. [Online]. Available: https://doi.org/10.1021/nl900772q (visited on 12/14/2022).

[30] K. Sayama, A. Nomura, Z. Zou, R. Abe, Y. Abe, and H. Arakawa, "Photoelectrochemical decomposition of water on nanocrystalline BiVO4 film electrodes under visible light," *Chemical Communications*, no. 23, p. 2908, 2003, ISSN: 1359-7345, 1364-548X. DOI: 10.1039/b310428a. [Online]. Available: http://xlink.rsc.org/?DOI=b310428a (visited on 12/14/2022).

[31] I. S. Cho, Z. Chen, A. J. Forman, D. R. Kim, P. M. Rao, T. F. Jaramillo, and X. Zheng, "Branched TiO2 Nanorods for Photoelectrochemical Hydrogen Production," *Nano Letters*, vol. 11, no. 11, pp. 4978–4984, Nov. 9, 2011, ISSN: 1530-6984. DOI: 10.1021/nl2029392. [Online]. Available: https://doi.org/10.1021/nl2029392 (visited on 12/14/2022).

[32] H. Kim, M. Seol, J. Lee, and K. Yong, "Highly Efficient Photoelectrochemical Hydrogen Generation Using Hierarchical ZnO/WOx Nanowires Cosensitized with CdSe/CdS," *The Journal of Physical Chemistry C*, vol. 115, no. 51, pp. 25 429–25 436, Dec. 29, 2011, ISSN: 1932-7447. DOI: 10.1021/jp2093115. [Online]. Available: https://doi.org/10.1021/jp2093115 (visited on 12/14/2022).

[33] O. Khaselev and J. A. Turner, "Electrochemical Stability of p-GaInP2 in Aqueous Electrolytes Toward Photoelectrochemical Water Splitting," *Journal of The Electrochemical Society*, vol. 145, no. 10, p. 3335, Oct. 1, 1998, ISSN: 1945-7111. DOI: 10.1149/1.1838808. [Online]. Available: https://iopscience.iop.org/article/10.1149/1.1838808/meta (visited on 12/14/2022).

[34] J. Gu, Y. Yan, J. L. Young, K. X. Steirer, N. R. Neale, and J. A. Turner, "Water reduction by a p-GaInP2 photoelectrode stabilized by an amorphous TiO2 coating and a molecular cobalt catalyst," *Nature Materials*, vol. 15, no. 4, pp. 456–460, Apr. 2016, ISSN: 1476-1122, 1476-4660. DOI: 10.1038/nmat4511. [Online].

Available: https://www.nature.com/articles/nmat4511 (visited on 12/14/2022).

[35] J. Wu, "When group-III nitrides go infrared: New properties and perspectives," *Journal of Applied Physics*, vol. 106, no. 1, p. 011 101, Jul. 1, 2009, ISSN: 0021-8979, 1089-7550. DOI: 10.1063/1.3155798. [Online]. Available: http://scitation.aip.org/content/aip/journal/jap/106/1/10.1063/1.3155798 (visited on 01/12/2016).

[36] Y. Wang, S. Vanka, J. Gim, Y. Wu, R. Fan, Y. Zhang, J. Shi, M. Shen, R. Hovden, and Z. Mi, "An In0.42Ga0.58N tunnel junction nanowire photocathode monolithically integrated on a non-planar Si wafer," *Nano Energy*, vol. 57, pp. 405–413, Mar. 1, 2019, ISSN: 2211-2855. DOI: 10.1016/j.nanoen.2018.12.067. [Online]. Available: https://www.sciencedirect.com/science/article/pii/S2211285518309807 (visited on 11/22/2022).

[37] S. Fan, B. AlOtaibi, S. Y. Woo, Y. Wang, G. A. Botton, and Z. Mi, "High Efficiency Solar-to-Hydrogen Conversion on a Monolithically Integrated InGaN/GaN/Si Adaptive Tunnel Junction Photocathode," *Nano Letters*, vol. 15, no. 4, pp. 2721–2726, Apr. 8, 2015, ISSN: 1530-6984. DOI: 10.1021/acs.nanolett.5b00535. [Online]. Available: https://doi.org/10.1021/acs.nanolett.5b00535 (visited on 11/22/2022).

[38] V. Parameshwaran, C. Gallinat, R. W. Enck, A. V. Sampath, P. H. Shen, T. Kuykendall, S. Aloni, M. Wraback, and B. M. Clemens, "III-V nitride semiconductors for solar hydrogen production," in *Energy Harvesting and Storage: Materials, Devices, and Applications III*, vol. 8377, SPIE, May 24, 2012, pp. 70–76. DOI: 10.1117/12.925200. [Online]. Available: https://www.spiedigitallibrary.org/conference-proceedings-of-spie/8377/83770B/III-V-nitride-semiconductors-for-solar-hydrogen-production/10.1117/12.925200.full (visited on 11/22/2022).

[39] K. Fujii and K. Ohkawa, "Photoelectrochemical Properties of p-Type GaN in Comparison with n-Type GaN," *Japanese Journal of Applied Physics*, vol. 44, p. L909, 7L Jul. 1, 2005, ISSN: 1347-4065. DOI: 10.1143/JJAP.44.L909. [Online]. Available: https://iopscience.iop.org/article/10.1143/JJAP.44.L909/meta (visited on 11/22/2022).

[40] M. Gopalakrishnan, S. Gopalakrishnan, G. M. Bhalerao, and K. Jeganathan, "Multiband InGaN nanowires with enhanced visible photon absorption for efficient photoelectrochemical water splitting," *Journal of Power Sources*, vol. 337, pp. 130–136, Jan. 1, 2017, ISSN: 0378-7753. DOI: 10.1016/j.jpowsour.2016.10.099. [Online]. Available: https://www.sciencedirect.com/science/article/pii/S0378775316315087 (visited on 12/14/2022).

[41] P. G. Moses and C. G. Van de Walle, "Band bowing and band alignment in InGaN alloys," *Applied Physics Letters*, vol. 96, no. 2, p. 021 908, Jan. 11, 2010, ISSN: 0003-6951. DOI: 10.1063/1.3291055. [Online]. Available: https://aip.scitation.org/doi/10.1063/1.3291055 (visited on 11/22/2022).

[42] B. AlOtaibi, H. P. T. Nguyen, S. Zhao, M. G. Kibria, S. Fan, and Z. Mi, "Highly Stable Photoelectrochemical Water Splitting and Hydrogen Generation Using a Double-Band InGaN/GaN Core/Shell Nanowire Photoanode," *Nano Letters*, vol. 13, no. 9, pp. 4356–4361, Sep. 11, 2013, ISSN: 1530-6984. DOI: 10.1021/nl402156e. [Online]. Available: https://doi.org/10.1021/nl402156e (visited on 12/14/2022).

[43] I. M. Huygens, K. Strubbe, and W. P. Gomes, "Electrochemistry and Photoetching of n-GaN," *Journal of The Electrochemical Society*, vol. 147, no. 5, p. 1797, May 1, 2000, ISSN: 1945-7111. DOI: 10.1149/1.1393436. [Online]. Available: https://iopscience.iop.org/article/10.1149/1.1393436/meta (visited on 12/14/2022).

[44] L.-H. Peng, C.-W. Chuang, J.-K. Ho, C.-N. Huang, and C.-Y. Chen, "Deep ultraviolet enhanced wet chemical etching of gallium nitride," *Applied Physics Letters*, vol. 72, no. 8, pp. 939–941, Feb. 23, 1998, ISSN: 0003-6951. DOI: 10.1063/1.120879. [Online]. Available: https://aip.scitation.org/doi/abs/10.1063/1.120879 (visited on 12/14/2022).

[45] C. H. Ko, Y. K. Su, S. J. Chang, W. H. Lan, J. Webb, M. C. Tu, and Y. T. Cherng, "Photo-enhanced chemical wet etching of GaN," *Materials Science and Engineering: B*, vol. 96, no. 1, pp. 43–47, Oct. 1, 2002, ISSN: 0921-5107. DOI: 10.1016/S0921-5107(02)00323-9. [Online]. Available: https://www.sciencedirect.com/science/article/pii/S0921510702003239 (visited on 12/14/2022).

[46] R. van de Krol and M. Grätzel, Eds., *Photoelectrochemical Hydrogen Production* (Electronic Materials: Science & Technology). Boston, MA: Springer US, 2012, vol. 102, ISBN: 978-1-4614-1379-0. DOI: 10.1007/978-1-4614-1380-6. [Online]. Available: http://link.springer.com/10.1007/978-1-4614-1380-6 (visited on 08/18/2022).

[47] S. M. Sze and K. K. Ng, *Physics of Semiconductor Devices*, 3rd ed. Hoboken, N.J: Wiley-Interscience, 2007, ISBN: 978-0-471-14323-9.

[48] R. F. Pierret, *Semiconductor Device Fundamentals*. Reading, Mass. Bonn: Addison-Wesley, 1996, 792 pp., ISBN: 978-0-201-54393-3.

[49] L. J. Minggu, W. R. Wan Daud, and M. B. Kassim, "An overview of photocells and photoreactors for photoelectrochemical water splitting," *International Journal of Hydrogen Energy*, 3rd Argentinean and 2nd Latin American Congress inHydrogen and

Sustainable Energy Sources, vol. 35, no. 11, pp. 5233–5244, Jun. 1, 2010, ISSN: 0360-3199. DOI: 10.1016/j.ijhydene.2010.02.133. [Online]. Available: https://www.sciencedirect.com/science/article/pii/S0360319910004374 (visited on 09/01/2022).

[50] A. Currao, V. R. Reddy, M. K. van Veen, R. E. I. Schropp, and G. Calzaferri, "Water splitting with silver chloride photoanodes and amorphous silicon solar cells," *Photochemical & Photobiological Sciences*, vol. 3, no. 11-12, pp. 1017–1025, Nov. 29, 2004, ISSN: 1474-9092. DOI: 10.1039/B411882K. [Online]. Available: https://pubs.rsc.org/en/content/articlelanding/2004/pp/b411882k (visited on 09/02/2022).

[51] E. Selli, G. L. Chiarello, E. Quartarone, P. Mustarelli, I. Rossetti, and L. Forni, "A photocatalytic water splitting device for separate hydrogen and oxygen evolution," *Chemical Communications*, no. 47, pp. 5022–5024, Nov. 29, 2007, ISSN: 1364-548X. DOI: 10.1039/B711747G. [Online]. Available: https://pubs.rsc.org/en/content/articlelanding/2007/cc/b711747g (visited on 09/02/2022).

[52] T. Bak, J. Nowotny, M. Rekas, and C. C. Sorrell, "Photo-electrochemical properties of the TiO2-Pt system in aqueous solutions," *International Journal of Hydrogen Energy*, vol. 27, no. 1, pp. 19–26, Jan. 1, 2002, ISSN: 0360-3199. DOI: 10.1016/S0360-3199(01)00090-8. [Online]. Available: https://www.sciencedirect.com/science/article/pii/S0360319901000908 (visited on 09/02/2022).

[53] N. K. Allam, K. Shankar, and C. A. Grimes, "Photoelectrochemical and water photoelectrolysis properties of ordered TiO2 nanotubes fabricated by Ti anodization in fluoride-free HCl electrolytes," *Journal of Materials Chemistry*, vol. 18, no. 20, pp. 2341–2348, May 7, 2008, ISSN: 1364-5501. DOI: 10.1039/B718580D. [Online]. Available: https://pubs.rsc.org/en/content/articlelanding/2008/jm/b718580d (visited on 09/02/2022).

[54] C. A. Grimes, O. K. Varghese, and S. Ranjan, Eds., *Light, Water, Hydrogen*. Boston, MA: Springer US, 2008, ISBN: 978-0-387-33198-0. DOI: 10.1007/978-0-387-68238-9. [Online]. Available: http://link.springer.com/10.1007/978-0-387-68238-9 (visited on 09/02/2022).

[55] S. Bae, J. Kang, E. Shim, J. Yoon, and H. Joo, "Correlation of electrical and physical properties of photoanode with hydrogen evolution in enzymatic photo-electrochemical cell," *Journal of Power Sources*, vol. 179, no. 2, pp. 863–869, May 1, 2008, ISSN: 0378-7753. DOI: 10.1016/j.jpowsour.2007.12.117. [Online]. Available: https://www.sciencedirect.com/science/article/pii/S0378775308000773 (visited on 09/02/2022).

[56] R. M. Eastment and C. H. B. Mee, "Work function measurements on (100), (110) and (111) surfaces of aluminium," *Journal of Physics F: Metal Physics*, vol. 3, no. 9, pp. 1738–1745, Sep. 1973, ISSN: 0305-4608. DOI: 10.1088/0305-4608/3/9/016. [Online]. Available: https://iopscience.iop.org/article/10.1088/0305-4608/3/9/016 (visited on 09/06/2022).

[57] Y. Park, V. Choong, Y. Gao, B. R. Hsieh, and C. W. Tang, "Work function of indium tin oxide transparent conductor measured by photoelectron spectroscopy," *Applied Physics Letters*, vol. 68, no. 19, pp. 2699–2701, May 6, 1996, ISSN: 0003-6951. DOI: 10.1063/1.116313. [Online]. Available: https://aip.scitation.org/doi/10.1063/1.116313 (visited on 09/06/2022).

[58] W. M. H. Sachtler, G. J. H. Dorgelo, and A. A. Holscher, "The work function of gold," *Surface Science*, vol. 5, no. 2, pp. 221–229, Oct. 1, 1966, ISSN: 0039-6028. DOI: 10.1016/0039-6028(66)90083-5. [Online]. Available: https://www.sciencedirect.com/science/article/pii/0039602866900835 (visited on 09/06/2022).

[59] J. Meng and Y. Jaluria, "Numerical Simulation of GaN Growth in a Metalorganic Chemical Vapor Deposition Process," *Journal of Manufacturing Science and Engineering*, vol. 135, no. 061013, Nov. 18, 2013, ISSN: 1087-1357. DOI: 10.1115/1.4025781. [Online]. Available: https://doi.org/10.1115/1.4025781 (visited on 01/08/2021).

[60] D. J. G. Speight, *Lange's Handbook of Chemistry, Seventeenth Edition*. McGraw-Hill Education, 2017, ISBN: 978-1-259-58609-5. [Online]. Available: https://www.accessengineeringlibrary.com/content/book/9781259586095 (visited on 11/30/2020).

[61] K. Rönnby, S. C. Buttera, P. Rouf, S. T. Barry, L. Ojamäe, and H. Pedersen, "Methylamines as Nitrogen Precursors in Chemical Vapor Deposition of Gallium Nitride," *The Journal of Physical Chemistry C*, vol. 123, no. 11, pp. 6701–6710, Mar. 21, 2019, ISSN: 1932-7447. DOI: 10.1021/acs.jpcc.9b00482. [Online]. Available: https://doi.org/10.1021/acs.jpcc.9b00482 (visited on 12/18/2020).

[62] J.-H. Boo, S.-B. Lee, Y.-S. Kim, J. T. Park, K.-S. Yu, and Y. Kim, "Growth of AlN and GaN Thin Films on Si(100) Using New Single Molecular Precursors by MOCVD Method," *physica status solidi (a)*, vol. 176, no. 1, pp. 711–717, 1999, ISSN: 1521-396X. DOI: 10.1002/(SICI)1521-396X(199911)176:1<711::AID-PSSA711>3.0.CO;2-Y. [Online]. Available: https://onlinelibrary.wiley.com/doi/abs/10.1002/%28SICI%291521-396X%28199911%29176%3A1%3C711%3A%3AAID-PSSA711%3E3.0.CO%3B2-Y (visited on 12/18/2020).

[63] D. K. Gaskill, N. Bottka, and M. C. Lin, "Growth of GaN films using trimethylgallium and hydrazine," *Applied Physics Letters*, vol. 48, no. 21, pp. 1449–1451, May 26, 1986, ISSN: 0003-6951. DOI: 10.1063/1.96886. [Online]. Available: https://aip.scitation.org/doi/10.1063/1.96886 (visited on 12/18/2020).

[64] D. Kum and D. Byun, "The effect of substrate surface roughness on GaN growth using MOCVD process," *Journal of Electronic Materials*, vol. 26, no. 10, pp. 1098–1102, Oct. 1, 1997, ISSN: 1543-186X. DOI: 10.1007/s11664-997-0001-3. [Online]. Available: https://doi.org/10.1007/s11664-997-0001-3 (visited on 12/09/2020).

[65] G. Namkoong, W. A. Doolittle, A. S. Brown, M. Losurdo, P. Capezzuto, and G. Bruno, "Role of sapphire nitridation temperature on GaN growth by plasma assisted molecular beam epitaxy: Part I. Impact of the nitridation chemistry on material characteristics," *Journal of Applied Physics*, vol. 91, no. 4, pp. 2499–2507, Jan. 29, 2002, ISSN: 0021-8979. DOI: 10.1063/1.1435834. [Online]. Available: https://aip.scitation.org/doi/abs/10.1063/1.1435834 (visited on 12/09/2020).

[66] A. Wierzbicka, Z. R. Zytkiewicz, S. Kret, *et al.*, "Influence of substrate nitridation temperature on epitaxial alignment of GaN nanowires to Si(111) substrate," *Nanotechnology*, vol. 24, no. 3, p. 035703, Dec. 2012, ISSN: 0957-4484. DOI: 10.1088/0957-4484/24/3/035703. [Online]. Available: https://doi.org/10.1088%2F0957-4484%2F24%2F3%2F035703 (visited on 12/09/2020).

[67] T. Ito, M. Sumiya, Y. Takano, K. Ohtsuka, and S. Fuke, "Influence of Thermal Annealing on GaN Buffer Layers and the Property of Subsequent GaN Layers Grown by Metalorganic Chemical Vapor Deposition," *Japanese Journal of Applied Physics*, vol. 38, p. 649, 2R Feb. 1, 1999, ISSN: 1347-4065. DOI: 10.1143/JJAP.38.649. [Online]. Available: https://iopscience.iop.org/article/10.1143/JJAP.38.649/meta (visited on 03/15/2021).

[68] C. Pelosi, G. Attolini, C. Bocchi, P. Franzosi, C. Frigeri, M. Berti, A. V. Drigo, and F. Romanato, "The role of the V/III ratio in the growth and structural properties of metalorganic vapor phase epitaxy GaAs/Ge heterostructures," *Journal of Electronic Materials*, vol. 24, no. 11, pp. 1723–1730, Nov. 1, 1995, ISSN: 1543-186X. DOI: 10.1007/BF02676841. [Online]. Available: https://doi.org/10.1007/BF02676841 (visited on 01/08/2021).

[69] M. Mesrine, N. Grandjean, and J. Massies, "Efficiency of NH3 as nitrogen source for GaN molecular beam epitaxy," *Applied Physics Letters*, vol. 72, no. 3, pp. 350–352, Jan. 19, 1998, ISSN: 0003-6951, 1077-3118. DOI: 10.1063/1.120733. [Online]. Available: http://aip.scitation.org/doi/10.1063/1.120733 (visited on 01/25/2018).

[70] C. Sone, M. Hong Kim, H. Jin Kim, and E. Yoon, "Effects of hydrogen on carbon incorporation in GaN grown by remote plasma-enhanced metal-organic chemical vapor deposition," *Journal of Crystal Growth*, vol. 189–190, pp. 321–324, Jun. 15, 1998, ISSN: 0022-0248. DOI: 10.1016/S0022-0248(98)00278-4. [Online]. Available: http://www.sciencedirect.com/science/article/pii/S0022024898002784 (visited on 01/08/2021).

[71] Y. Horikoshi, "Flow Rate Modulated Vapor Epitaxy," in *Reference Module in Materials Science and Materials Engineering*, Elsevier, Jan. 1, 2016, ISBN: 978-0-12-803581-8. DOI: 10.1016/B978-0-12-803581-8.03667-5. [Online]. Available: http://www.sciencedirect.com/science/article/pii/B9780128035818036675 (visited on 01/09/2021).

[72] R. S. Q. Fareed, R. Jain, R. Gaska, M. S. Shur, J. Wu, W. Walukiewicz, and M. A. Khan, "High quality InN/GaN heterostructures grown by migration enhanced metalorganic chemical vapor deposition," *Applied Physics Letters*, vol. 84, no. 11, pp. 1892–1894, Mar. 15, 2004, ISSN: 0003-6951, 1077-3118. DOI: 10.1063/1.1686889. [Online]. Available: http://scitation.aip.org/content/aip/journal/apl/84/11/10.1063/1.1686889 (visited on 09/29/2015).

[73] Q. Fareed, R. Gaska, and M. S. Shur, "Migration Enhanced Metal Organic Chemical Vapor Deposition of AlN/GaN/InN-Based Heterostructures," in *International Semiconductor Device Research Symposium, 2003*, Dec. 2003, pp. 402–403. DOI: 10.1109/ISDRS.2003.1272154.

[74] H. Lu, W. J. Schaff, J. Hwang, H. Wu, W. Yeo, A. Pharkya, and L. F. Eastman, "Improvement on epitaxial grown of InN by migration enhanced epitaxy," *Applied Physics Letters*, vol. 77, no. 16, pp. 2548–2550, Oct. 16, 2000, ISSN: 0003-6951, 1077-3118. DOI: 10.1063/1.1318235. [Online]. Available: http://scitation.aip.org/content/aip/journal/apl/77/16/10.1063/1.1318235 (visited on 06/15/2016).

[75] K. Kusakabe, K. Kishino, A. Kikuchi, T. Yamada, D. Sugihara, and S. Nakamura, "Reduction of threading dislocations in migration enhanced epitaxy grown GaN with N-polarity by use of AlN multiple interlayer," *Journal of Crystal Growth*, Proceedings of the Fourth European Workshop on Gallium Nitride, vol. 230, no. 3–4, pp. 387–391, Sep. 2001, ISSN: 0022-0248. DOI: 10.1016/S0022-0248(01)01248-9. [Online]. Available: http://www.sciencedirect.com/science/article/pii/S0022024801012489 (visited on 09/29/2015).

[76] C. Adelmann, J. Brault, J.-L. Rouvière, H. Mariette, G. Mula, and B. Daudin, "Atomic-layer epitaxy of GaN quantum wells and quantum dots on (0001) AlN," *Journal of Applied Physics*, vol. 91, no. 8, pp. 5498–5500, Mar. 29, 2002, ISSN: 0021-8979. DOI: 10.1063/1.1458049. [Online]. Available: https://aip.

scitation.org/doi/abs/10.1063/1.1458049 (visited on 03/15/2021).

[77] X. Liu, S. Ramanathan, A. Longdergan, A. Srivastava, E. Lee, T. E. Seidel, J. T. Barton, D. Pang, and R. G. Gordon, "ALD of Hafnium Oxide Thin Films from Tetrakis(ethylmethylamino)hafnium and Ozone," *Journal of The Electrochemical Society*, vol. 152, no. 3, G213, Jan. 31, 2005, ISSN: 1945-7111. DOI: 10.1149/1.1859631. [Online]. Available: https://iopscience.iop.org/article/10.1149/1.1859631/meta (visited on 03/15/2021).

[78] C. Ozgit, I. Donmez, M. Alevli, and N. Biyikli, "Atomic layer deposition of GaN at low temperatures," *Journal of Vacuum Science & Technology A*, vol. 30, no. 1, 01A124, Jan. 1, 2012, ISSN: 0734-2101, 1520-8559. DOI: 10.1116/1.3664102. [Online]. Available: http://scitation.aip.org/content/avs/journal/jvsta/30/1/10.1116/1.3664102 (visited on 03/01/2016).

[79] H. Eichhorn, K. H. Schoenbach, and T. Tessnow, "Paschen's law for a hollow cathode discharge," *Applied Physics Letters*, vol. 63, no. 18, pp. 2481–2483, Nov. 1, 1993, ISSN: 0003-6951. DOI: 10.1063/1.110455. [Online]. Available: https://aip.scitation.org/doi/10.1063/1.110455 (visited on 03/15/2021).

[80] K. S. A. Butcher, D. Alexandrov, P. Terziyska, V. Georgiev, and D. Georgieva, "Initial experiments in the migration enhanced afterglow growth of gallium and indium nitride," *physica status solidi (c)*, vol. 9, no. 3-4, pp. 1070–1073, Mar. 2012, ISSN: 18626351. DOI: 10.1002/pssc.201100209. [Online]. Available: http://doi.wiley.com/10.1002/pssc.201100209 (visited on 05/02/2017).

[81] *Nitrogen Data Sheet*. [Online]. Available: https://www.lindeus.com/-/media/corporate/praxairus/documents/specification-sheets-and-brochures/gases/nitrogen/nitrogen-n2-spec-sheet-ss-p4631.pdf?la=en.

[82] *Bragg's law*, in *Wikipedia*, Aug. 16, 2022. [Online]. Available: https://en.wikipedia.org/w/index.php?title=Bragg%27s_law&oldid=1104663695 (visited on 09/16/2022).

[83] M. A. Moram and M. E. Vickers, "X-ray diffraction of III-Nitrides," *Reports on Progress in Physics*, vol. 72, no. 3, p. 036 502, 2009, ISSN: 0034-4885. DOI: 10.1088/0034-4885/72/3/036502.

[84] P. Worsfold, "SPECTROPHOTOMETRY | Overview," in *Encyclopedia of Analytical Science*, Elsevier, 2005, pp. 318–321, ISBN: 978-0-12-369397-6. DOI: 10.1016/B0-12-369397-7/00714-7. [Online]. Available: https://linkinghub.elsevier.com/retrieve/pii/B0123693977007147 (visited on 09/16/2022).

[85] J. Tauc, R. Grigorovici, and A. Vancu, "Optical Properties and Electronic Structure of Amorphous Germanium," *physica status solidi (b)*, vol. 15, no. 2, pp. 627–637, 1966, ISSN: 1521-3951. DOI: 10.1002/pssb.19660150224. [Online]. Available:

https://onlinelibrary.wiley.com/doi/abs/10.1002/pssb.19660150224 (visited on 03/01/2019).

[86] E. A. Davis and N. F. Mott, "Conduction in non-crystalline systems V. Conductivity, optical absorption and photoconductivity in amorphous semiconductors," *Philosophical Magazine*, vol. 22, no. 179, pp. 0903–0922, Nov. 1970, ISSN: 0031-8086. DOI: 10.1080/14786437008221061. [Online]. Available: http://www.tandfonline.com/doi/abs/10.1080/14786437008221061 (visited on 09/20/2022).

[87] J. Orloff, Ed., *Handbook of Charged Particle Optics*, 2. ed. Boca Raton: CRC Press, 2009, 665 pp., ISBN: 978-1-4200-4554-3.

[88] S. O. Kasap, *Principles of Electronic Materials and Devices*, Fourth edition. New York, NY: McGraw-Hill, a business unit of The McGraw-Hill Companies, Inc, 2018, ISBN: 978-0-07-802818-2.

[89] L. J. van der PAUW, "A Method of Measuring Specific Resistivity and Hall Effect of Discs of Arbitrary Shape," in *Semiconductor Devices: Pioneering Papers*. WORLD SCIENTIFIC, Mar. 1991, pp. 174–182, ISBN: 978-981-02-0209-5. DOI: 10.1142/9789814503464_0017. [Online]. Available: http://www.worldscientific.com/doi/abs/10.1142/9789814503464_0017 (visited on 09/23/2022).

[90] B. Voigtländer, *Scanning Probe Microscopy: Atomic Force Microscopy and Scanning Tunneling Microscopy* (NanoScience and Technology). Berlin, Heidelberg: Springer Berlin Heidelberg, 2015, ISBN: 978-3-662-45239-4. DOI: 10.1007/978-3-662-45240-0. [Online]. Available: http://link.springer.com/10.1007/978-3-662-45240-0 (visited on 09/22/2022).

[91] S. Wang, H. Liu, Q. Chen, and H. Zhang, "An analytical model of low field and high field electron mobility in wurtzite indium nitride," *Journal of Materials Science: Materials in Electronics*, vol. 27, no. 11, pp. 11353–11357, Nov. 1, 2016, ISSN: 1573-482X. DOI: 10.1007/s10854-016-5259-x. [Online]. Available: https://doi.org/10.1007/s10854-016-5259-x (visited on 11/06/2019).

[92] S. K. O'Leary, B. E. Foutz, M. S. Shur, and L. F. Eastman, "Potential performance of indium-nitride-based devices," *Applied Physics Letters*, vol. 88, no. 15, p. 152113, Apr. 10, 2006, ISSN: 0003-6951. DOI: 10.1063/1.2193469. [Online]. Available: https://aip.scitation.org/doi/full/10.1063/1.2193469 (visited on 11/06/2019).

[93] V. M. Polyakov and F. Schwierz, "Low-field electron mobility in wurtzite InN," *Applied Physics Letters*, vol. 88, no. 3, p. 032101, Jan. 16, 2006, ISSN: 0003-6951, 1077-3118. DOI: 10.1063/1.2166195. [Online]. Available: http://scitation.aip.org.ezproxy.lakeheadu.ca/content/aip/journal/apl/88/3/10.1063/1.2166195 (visited on 03/27/2016).

[94] I. Mahboob, T. D. Veal, L. F. J. Piper, C. F. McConville, H. Lu, W. J. Schaff, J. Furthmüller, and F. Bechstedt, "Origin of electron accumulation at wurtzite InN surfaces," *Physical Review B*, vol. 69, no. 20, p. 201 307, May 20, 2004. DOI: 10.1103/PhysRevB.69.201307. [Online]. Available: http://link.aps.org/doi/10.1103/PhysRevB.69.201307 (visited on 12/09/2015).

[95] K.-W. Kao, M.-C. Hsu, Y.-H. Chang, S. Gwo, and J. A. Yeh, "A Sub-ppm Acetone Gas Sensor for Diabetes Detection Using 10 nm Thick Ultrathin InN FETs," *Sensors (Basel, Switzerland)*, vol. 12, no. 6, pp. 7157–7168, May 29, 2012, ISSN: 1424-8220. DOI: 10.3390/s120607157. pmid: 22969342. [Online]. Available: https://www.ncbi.nlm.nih.gov/pmc/articles/PMC3435971/ (visited on 06/26/2018).

[96] Y.-S. Lu, J.-L. Ho, J. Yeh, and S. Gwo, "InN-based anion selective sensing devices," in *2009 Sixth International Conference on Networked Sensing Systems (INSS)*, Jun. 2009, pp. 1–4. DOI: 10.1109/INSS.2009.5409932.

[97] K. P. Biju and M. K. Jain, "The effect of rf power on the growth of InN films by modified activated reactive evaporation," *Applied Surface Science*, vol. 254, no. 22, pp. 7259–7265, Sep. 2008, ISSN: 01694332. DOI: 10.1016/j.apsusc.2008.05.297. [Online]. Available: https://linkinghub.elsevier.com/retrieve/pii/S0169433208012956 (visited on 02/01/2022).

[98] X.-M. Cai, F. Ye, Y.-Q. Hao, D.-P. Zhang, Z.-H. Zhang, and P. Fan, "The properties of direct current sputtering deposited InN thin films under different gas flow rates," *Journal of Alloys and Compounds*, vol. 484, no. 1-2, pp. 677–681, Sep. 2009, ISSN: 09258388. DOI: 10.1016/j.jallcom.2009.05.021. [Online]. Available: https://linkinghub.elsevier.com/retrieve/pii/S0925838809009323 (visited on 02/01/2022).

[99] I. Bello, W. M. Lau, R. P. W. Lawson, and K. K. Foo, "Deposition of indium nitride by low energy modulated indium and nitrogen ion beams," *Journal of Vacuum Science & Technology A: Vacuum, Surfaces, and Films*, vol. 10, no. 4, pp. 1642–1646, Jul. 1992, ISSN: 0734-2101, 1520-8559. DOI: 10.1116/1.577763. [Online]. Available: http://avs.scitation.org/doi/10.1116/1.577763 (visited on 06/14/2022).

[100] V. Lebedev, V. Cimalla, J. Pezoldt, M. Himmerlich, S. Krischok, J. A. Schaefer, O. Ambacher, F. M. Morales, J. G. Lozano, and D. González, "Effect of dislocations on electrical and electron transport properties of InN thin films. I. Strain relief and formation of a dislocation network," *Journal of Applied Physics*, vol. 100, no. 9, p. 094 902, Nov. 2006, ISSN: 0021-8979, 1089-7550. DOI: 10.1063/1.2363233. [Online]. Available: http://aip.scitation.org/doi/10.1063/1.2363233 (visited on 10/30/2019).

[101] G. Beamson and D. Briggs, "High resolution XPS of organic polymers: The Scienta ESCA 300 database.," *Surface and Interface Analysis*, vol. 20, no. 3, pp. 267–267, Mar. 1993, ISSN: 01422421. DOI: 10.1002/sia.740200310. [Online]. Available: https://onlinelibrary.wiley.com/doi/10.1002/sia.740200310 (visited on 09/28/2021).

[102] Z. Wang, C. Li, L. Liu, and T.-K. Sham, "Probing defect emissions in bulk, micro- and nano-sized α-Al $_2$ O $_3$ via X-ray excited optical luminescence," *The Journal of Chemical Physics*, vol. 138, no. 8, p. 084706, Feb. 28, 2013, ISSN: 0021-9606, 1089-7690. DOI: 10.1063/1.4793473. [Online]. Available: http://aip.scitation.org/doi/10.1063/1.4793473 (visited on 02/01/2022).

[103] D. Wang, J. Yang, X. Li, J. Wang, R. Li, M. Cai, T. K. Sham, and X. Sun, "Observation of Surface/Defect States of SnO2 Nanowires on Different Substrates from X-ray Excited Optical Luminescence," *Crystal Growth & Design*, vol. 12, no. 1, pp. 397–402, Jan. 4, 2012, ISSN: 1528-7483. DOI: 10.1021/cg2011919. [Online]. Available: https://doi.org/10.1021/cg2011919 (visited on 02/01/2022).

[104] D. Alexandrov, K. S. A. Butcher, and M. Wintrebert-Fouquet, "Absorption and photoluminescence features caused by defects in InN," *Journal of Crystal Growth*, Proceedings of the First ONR International Indium Nitride Workshop, vol. 269, no. 1, pp. 77–86, Aug. 15, 2004, ISSN: 0022-0248. DOI: 10.1016/j.jcrysgro.2004.05.036. [Online]. Available: http://www.sciencedirect.com/science/article/pii/S0022024804005998 (visited on 06/26/2018).

[105] M. Amirhoseiny, Z. Hassan, and S. Ng, "Photoluminescence spectra of nitrogen-rich InN thin films grown on Si(110) and photoelectrochemical etched Si(110)," *Vacuum*, vol. 101, pp. 217–220, Mar. 2014, ISSN: 0042207X. DOI: 10.1016/j.vacuum.2013.08.017. [Online]. Available: https://linkinghub.elsevier.com/retrieve/pii/S0042207X13003102 (visited on 02/01/2022).

[106] Q. X. Guo, T. Tanaka, M. Nishio, H. Ogawa, X. D. Pu, and W. Z. Shen, "Observation of visible luminescence from indium nitride at room temperature," *Applied Physics Letters*, vol. 86, no. 23, p. 231913, Jun. 6, 2005, ISSN: 0003-6951, 1077-3118. DOI: 10.1063/1.1947914. [Online]. Available: http://aip.scitation.org/doi/10.1063/1.1947914 (visited on 02/01/2022).

[107] K. Schwarz, P. Blaha, and G. Madsen, "Electronic structure calculations of solids using the WIEN2k package for material sciences," *Computer Physics Communications*, vol. 147, no. 1-2, pp. 71–76, Aug. 2002, ISSN: 00104655. DOI: 10.1016/S0010-4655(02)00206-0. [Online]. Available: https://linkinghub.elsevier.com/retrieve/pii/S0010465502002060 (visited on 02/01/2022).

[108] M. R. Amin, T. de Boer, P. Becker, J. Hertrampf, R. Niewa, and A. Moewes, "Bandgap and Electronic Structure Determination of Oxygen-Containing Ammonothermal InN: Experiment and Theory," *The Journal of Physical Chemistry C*, vol. 123, no. 14, pp. 8943–8950, Apr. 11, 2019, ISSN: 1932-7447. DOI: 10.1021/acs.jpcc.8b12369. [Online]. Available: https://doi.org/10.1021/acs.jpcc.8b12369 (visited on 10/25/2019).